Infrared Spectroscopy of Small Molecules and Hydrogen-Bonded Dimers in Helium Nanodroplets

by

Christy J. Knapp

A thesis submitted in partial fulfillment of the requirements for the degree of

Doctor of Philosophy

Department of Chemistry

University of Alberta

Abstract

As a spectroscopic matrix, helium nanodroplets exhibit many advantages over frozen rare gas matrices or other seeded clusters. Helium nanodroplets are superfluid, and interact only very weakly with embedded dopants, meaning high-resolution spectra are possible. Further, dopants are rapidly cooled to the droplet temperature of ~0.4 K, such that only the ground vibrational state is populated. Finally, helium nanodroplets are transparent to all wavelengths above ~60 nm. In this thesis, the infrared laser spectra of hydrogen peroxide, singly deuterated hydrogen peroxide, and hydrogen bonded dimers embedded in superfluid helium nanodroplets are presented.

The infrared spectrum of hydrogen peroxide reveals much about the interaction between the helium bath and the dopant. First, the *B* rotational constant is reduced by ~42% of the gas phase value, while the *A* constant is largely unaffected due to fast rotation about the *a*-inertial axis. The extent of renormalization was found to be the same for singly deuterated hydrogen peroxide. The *trans*-tunneling splitting is reduced by only 6% of the gas phase value. Rovibrational linewidths vary based on the density of phonon states available in the droplet at

various rotational energies. Linewidths are narrower for lines with rotational energies falling within the "phonon gap." Finally, dynamic coupling between the H_2O_2 rotor and the surrounding helium density resulted in asymmetrically skewed lines.

Infrared spectra of two hydrogen bonded dimers in helium droplets are reported. The hydrogen peroxide dimer exhibits two OH vibrational modes corresponding to the bound and free OH asymmetric stretch. The bound OH stretch is significantly redshifted compared to the free OH stretch, in good agreement with previously reported spectra in a solid argon matrix. Both lines were broadened to an extent that rotationally resolved lines were not observed, and the precise configuration of the dimer could not be determined beyond having a cyclic shape. For the formic acid dimer, rotational analysis was possible, and the structure was found to be consistent with a non-polar, cyclic structure.

Preface

Some of the work in this thesis was part of a collaborative effort between myself and other researchers. I have detailed the contributions of others to this work below.

Chapter 4 of this thesis has been published as "Rotovibrational spectrocopy of hydrogen peroxide embedded in superfluid helium nanodroplets" by P.L. Raston, C.J. Knapp, and W. Jäger [*Phys. Chem. Chem. Phys.* **2011**, *13,* 18789-18798]. The collection of data, analysis, and preparation of the manuscript was done cooperatively between myself and P.L. Raston. As the supervisory author, W. Jäger was involved with concept formation and manuscript preparation.

Chapter 7 of this thesis is currently in preparation for publication as "Helium nanodroplet isolation and ro-vibrational spectroscopy of the cyclic formic acid dimer" by P. Das, C.J. Knapp, and W. Jäger. The experimental design as it pertains to laser spectroscopy was done by myself, and the collection of data and analyses were done cooperatively by P. Das and myself. Manuscript preparation was done by P. Das, myself and W. Jäger. W. Jäger was also involved in concept formation.

Chapters 6 and 7 are my original work. I collected the data and performed the analyses. This work has not been published elsewhere. W. Jäger was involved in concept formation.

For Nolan and Clara

Acknowledgements

First, I would like to acknowledge my excellent supervisor, Prof. Wolfgang Jäger. I am thankful for his guidance, patience, and unfailing support during my time as a PhD student. Each conversation we had was invaluable, whether it related to my research, parenting, or politics. I am also grateful for the opportunity to present my work at many conferences, and for being involved in many fascinating projects.

I would like to thank Prof. Yunjie Xu for many interesting conversations about spectroscopy, and for always giving honest advice. Dr. Paul Raston deserves many thanks for his excellent teaching skills, and for preparing me for the countless hours of problem solving and equipment repair in the helium droplet lab. For their excellent technical skills, I'd also like to thank department staff members: Allan, Kim, Jason, Dirk, Dieter, Vincent and Paul.

For their support, I thank my supervisory committee: Prof. Roderick Wasylishen, and Prof. Frederick West. I am also thankful to Prof. Gabriel Hanna for being on my exam committee, and to Prof. Takamasa Momose for agreeing to be my external examiner.

I thank past and present members of both the Xu and Jäger groups. Christian, Elijah, Fumie, Javix, Jiao, Joseph, Prasanta, Reza, Shawn, Steve, Supriya, Zahra and any others whom I may have missed.

I am grateful for the funding I received from the Natural Sciences and Engineering Research Council, Alberta Innovates, and the University of Alberta.

I thank Gary Douberly and his group members from the University of Georgia for help with laser automation, and for providing a macro for collecting optically selected mass spectra.

Finally, I thank family and friends for their immeasurable support. To Jason, I will be forever grateful for every single 5:00 am cup of coffee he brewed for me. For their love and support I thank John and Karen Knapp. For occasionally allowing me some sleep, and for just generally being wonderful, I thank Nolan and Clara.

Table of Contents

List of Tables

List of Figures

List of Symbols

T_λ	Lambda-temperature for superfluid helium
ρ	Density
ρ_n	Normal fluid density
ρ_s	Superfluid density
P_0	Helium backing pressure
T_0	Nozzle temperature
$\langle N \rangle$	Mean number of helium atoms per droplet
P_n	Probability of picking up n molecules as defined by Poisson statistics
σ	Cross sectional area of a droplet
L	Length of the doping call
n	Number of molecules picked up by a droplet
A, B, C	Rotational constants
λ	Wavelength
$\boldsymbol{P}$	Polarizability

$\boldsymbol{E}$	Electric field
χ	Electric susceptibility
ω	Frequency
J	Rotational angular momentum quantum number
K	Symmetric top quantum number
v_n	Vibrational mode
τ	Torsional state
κ	Asymmetry parameter
$\overline{D}_J, D'_{JK}$	Centrifugal distortion constants

List of Abbreviations

HENDI	Helium nanodroplet isolation
LDM	Liquid drop model
QMS	Quadrupole mass spectrometer
OPO	Optical parametric oscillator
PPNL	Periodically-poled lithium niobate
YAG	Yttrium Aluminum Garnet
ICE	Intracavity etalon
VI	Virtual instrument
cw	Continuous wave
IR	Infrared
OSMS	Optically selected mass spectrum
UHP	Urea hydrogen peroxide
UU, UD	Up-Up and Up-Down conformers of the hydrogen peroxide dimer

Chapter 1: Introduction

1.0 Introduction

Cryogenic matrix isolation techniques have long been employed for studying molecules and molecular clusters. Of particular significance is the use of matrix isolation to study transient species. Such species can be trapped in frozen rare-gas matrices and probed spectroscopically, revealing desirable information about conformation, molecular interactions, and low-temperature reactions. However, the solid nature of most rare-gas matrices results in many spectroscopic drawbacks, such as symmetry changes, large vibrational perturbations with respect to the gas phase, and low resolution spectra due to the inhibition of rotational motion of the trapped molecules.[1] Solid rare-gas matrices can therefore result in the loss of much-needed information about the species being probed.

In the early 1990's, a new cryogenic matrix isolation technique arose in answer to the many drawbacks of frozen rare-gas matrices. This technique uses liquid helium as the matrix, and is often referred to as Helium Nanodroplet Isolation (HENDI) Spectroscopy.[2] Since their inception, helium nanodroples have been referred to as an "ideal" matrix, and even the

"*ultimate*" matrix, due to the unique nature of liquid helium.[1] The nanoscale droplets of helium used in HENDI spectroscopy are cold (~0.37 K), superfluid, and interact only very weakly with molecules or other dopants. Each of these unique properties reduces the effect of the matrix on the species of interest, resulting in spectra that more closely resemble those recorded in the gas-phase.

1.1 Superfluid Helium

The increasing popularity of helium nanodroplet spectroscopy is a direct result of the fundamental properties of helium-4 atoms. Interactions between helium atoms are very weak, and its low mass results in large zero-point oscillations. As a result, helium will theoretically remain a liquid down to absolute zero. Helium condenses to form a classical liquid at 4.2 K, referred to as He I, at standard atmospheric pressure. When cooled below 2.2 K (the so-called lambda-temperature, or T_λ), liquid helium undergoes a phase transition to a quantum fluid phase, He II. The He II phase is referred to as superfluid helium, and exhibits many fascinating properties, including zero viscosity flow, and unusually high heat conductance.[1]

Superfluid helium is described by the two-fluid model,[3,4] wherein the quantum fluid is defined as being composed of two types of fluids: a superfluid, and a normal fluid. The total fluid density below T_λ, ρ, is described as a sum of the normal fluid density (ρ_n) and the superfluid density (ρ_s) as shown in equation (1):

$$\rho = \rho_n + \rho_s \tag{1}$$

At temperatures higher than the lambda-point, the fluid density consists of only normal fluid, while below the lambda-temperature, the superfluid density increases as the temperature decreases until absolute zero, where liquid helium theoretically consists of only superfluid. The

fundamental difference between the normal fluid component and the superfluid component is that the latter exists as a bose-condensate, meaning the helium atoms are all in the same quantum state and can therefore be described by a single wavefunction. As a result, the helium atoms that are part of the condensate are indistinguishable, and represent a bulk manifestation of quantum mechanics.

Experimental evidence for the two-fluid model was provided by the famous Andronikashvili experiment in 1946.[5] A rotating pendulum with closely spaced discs was placed in a helium-4 bath. Below the lambda-temperature, it was shown that the period of the rotating discs was temperature dependent. As the temperature decreased, there was less drag on the pendulum, and therefore less damping of the oscillatory period. The decreased damping of the pendulum rotations represents an increasing trend towards frictionless flow, and therefore an increase in the superfluid density below 2.2 K.

1.3 Helium Nanodroplets

Droplets of liquid helium were first observed in a fog following rapid cooling of helium gas in 1908,[6] many years prior to the discovery of superfluidity in bulk helium in the 1930's.[7] The discovery of, and subsequent interest in, superfluidity resulted in a breadth of theoretical research, including much interest in nanoscale droplets of helium, which represent finite quantum systems.[8] In 1961, nanoscale helium droplets were observed in a free-jet expansion.[9] Early work on understanding the properties of helium droplets was achieved in the early 1990's, when nanoscale droplets were doped with SF_6, and its rovibrational spectrum was measured.[10] The presence of rotationally resolved lines was the first indication that the helium droplet matrix was unique compared to other seeded rare gas clusters or frozen matrices, and suggested the

droplets were superfluid. Indeed, the majority of our present understanding of the properties of helium nanodroplets comes from measuring the spectra of dopants inside the droplets.[11] Because helium droplets are transparent to light with wavelengths larger than ~60 nm, direct experimentation on the droplets themselves is experimentally challenging. Not only is experimentation with such short wavelengths challenging, the diffuse droplet beam also makes the measurement of absorption difficult. The transparency to wavelengths greater than ~60 nm, however, means that helium droplets are valuable as a spectroscopic matrix.[1]

In 1998, Grebenev *et al*.[12] provided the first solid evidence of superfluidity in nanoscale droplets of helium, in what was called the "Microscopic Andronikashvili Experiment." In the experiment, the rovibrational spectrum of OCS embedded in both normal fluid helium nanodroplets comprised of helium-3, and droplets containing helium-4. In the pure helium-3 droplets, the infrared spectrum of OCS shows no rotational resolution due to the large drag on the rotational motion of the OCS molecule by the normal-fluid helium. In droplets where the OCS molecule was solvated by at least 60 helium atoms, sharp rotational lines were observed, indicating that the helium-4 was superfluid and allowed for nearly-free rotation of the OCS molecule, much like the rotation of the pendulum in helium-4 below the lambda-temperature in Andronikashvili's experiment.[5] Since then, microwave experiments have shown that it takes as little as 7 helium atoms for the onset of superfluidity in small OCS-He_N clusters.[13] Helium-4 nanodroplets evaporatively cool to 0.37 K, well below the lambda-point, meaning they have a high superfluid density.[14] This is in contrast to helium-3 droplets, which cool to 0.15 K, which is above the lambda temperature for the helium-3 isotope.[1]

Superfluidity in helium nanodroplets is now well established, and is responsible for the spectroscopic advantage of using helium nanodroplets over other rare-gas matrices. Many

questions about the nature of superfluidity in nanoscale droplets remain, however, making the droplets themselves a continued subject of intense experimental interest. An area of special importance to spectroscopy is the nature of interactions between the helium bath and the dopant species. As it stands, the field of helium nanodroplet spectroscopy has matured to the point of having wide-ranging applications that include the study of low-temperature reactions,[15] surface deposition experiments,[16] and a matrix in which to study large biomolecular ions.[17] In this thesis, I build upon studies examining the interplay between the superfluid matrix and transiently chiral hydrogen peroxide, and also make use of the droplets as a matrix in which to examine small hydrogen bonded dimers, including the hydrogen peroxide dimer and the formic acid dimer.

1.4 Thesis Organization

In the chapters that follow, I present my studies on small molecules and dimers embedded in superfluid helium nanodroplets. Chapter 2 outlines the experimental techniques used throughout my investigations, as well as pertinent background information about helium nanodroplet spectroscopy. Details of the infrared laser system and the automation of its tuning are presented in Chapter 3. In Chapter 4, the rotovibrational spectrum of hydrogen peroxide in helium nanodroplets is discussed. Insights from this work include an examination of the effects of the superfluid helium matrix on the spectrum, including line-broadening and the observed tunneling splitting. The following chapter presents a similar spectral analysis of the singly deuterated species, HOOD. The spectrum of the hydrogen peroxide dimer is discussed in Chapter 6. The identification and analysis of the cyclic formic acid dimer is provided in Chapter 7. Finally, the thesis is concluded in Chapter 8.

References

[1] J. P. Toennies, A. F. Vilesov, *Angew. Chem. - Int. Ed.* **2004**, *43*, 2622–2648.

[2] M. Y. Choi, G. E. Douberly, T. M. Falconer, W. K. Lewis, C. M. Lindsay, J. M. Merritt, P. L. Stiles, R. E. Miller, *Int. Rev. Phys. Chem.* **2006**, *25*, 15–75.

[3] L. TISZA, *Nature* **1938**, *141*, 913.

[4] L. Landau, *Phys. Rev.* **1941**, *60*, 356–358.

[5] E. L. Andronikashvili, *J Phys USSR* **1946**, *10*.

[6] O. H. Kamerlingh, *Commun Phys Lab Univ Leiden* **1908**, *105*, 3.

[7] P. Kapitza, *Nature* **1938**, *141*, 74.

[8] P. Sindzingre, M. L. Klein, D. M. Ceperley, *Phys. Rev. Lett.* **1989**, *63*, 1601–1604.

[9] E. W. Becker, *Z. Für Phys. At. Mol. Clust.* **1986**, *3*, 101–107.

[10] S. Goyal, D. L. Schutt, G. Scoles, *Phys. Rev. Lett.* **1992**, *69*, 933–936.

[11] F. Stienkemeier, K. K. Lehmann, *J. Phys. B At. Mol. Opt. Phys.* **2006**, *39*, R127–R166.

[12] S. Grebenev, J. P. Toennies, A. F. Vilesov, *Science* **1998**, *279*, 2083–2086.

[13] J. Tang, J. Xu, A. R. W. McKellar, W. Jäger, *Science* **2002**, *297*, 2030–2033.

[14] M. Hartmann, R. E. Miller, J. P. Toennies, A. Vilesov, *Phys. Rev. Lett.* **1995**, *75*, 1566–1569.

[15] S. A. Krasnokutski, M. Kuhn, M. Renzler, C. Jäger, T. Henning, P. Scheier, *Astrophys. J. Lett.* **2016**, *818*, L31.

[16] A. Volk, P. Thaler, D. Knez, A. W. Hauser, J. Steurer, W. Grogger, F. Hofer, W. E. Ernst, *Phys. Chem. Chem. Phys.* **2016**, *18*, 1451–1459.

[17] F. Bierau, P. Kupser, G. Meijer, G. von Helden, *Phys Rev Lett* **2010**, *105*, 133402.

Chapter 2: Experimental Design and Fundamental Concepts

2.0 Introduction

The low temperature of helium nanodroplets provides a useful environment for the investigation of chemical systems. Simplified spectra arising from fewer populated states, the narrowing of spectral lines, trapping of reaction intermediates or metastable species, and low-temperature chemical reaction studies are just some of the many advantages provided by the low temperature of helium nanodroplets.[1] Unlike frozen rare-gas matrices, helium nanodroplets also allow for the measurement of spectra with rotational resolution, which provides a degree of structural information not available in any other matrix. High-resolution, low-temperature spectra can also be obtained from seeded supersonic jets, but unlike helium nanodroplets, all degrees of freedom for the species of interest are not in thermal equilibrium with the translational temperature of the molecular beam, which is typically on the order of 1 K. Helium nanodroplets, on the other hand, can achieve cooling of translational, rotational and vibrational levels to less

than 1 K, while also providing a matrix in which high-resolution spectra can be measured. Thus, helium nanodroplet spectroscopy represents a coupling of matrix isolation and molecular beam techniques.

Infrared laser spectroscopy has proven to be especially well suited for the investigation of chemical systems embedded in helium nanodroplets, such as molecules, clusters, or radicals. For many such systems, a rovibrational spectrum can be recorded and analyzed, providing useful details such as structural information, or the effect of the quantum solvent on the behavior of the system.[1–3] Beyond an examination of the quantum solvent, however, one may ask why it is necessary to record infrared spectra of dopants in helium nanodroplets rather than simply in gas phase. Unlike the gas phase spectra, helium nanodroplets provide superior cooling, reaching a lower temperature than is typically achieved using standard gas phase techniques. Further, it is well established that the helium droplet matrix can be used to trap high energy, metastable structures that cannot be easily produced in the gas phase. In fact, all advantages of frozen rare-gas matrices are present in helium droplet spectroscopy, but the spectra recorded in helium droplets experience less matrix effects.

Helium nanodroplets are produced, doped, probed with infrared radiation, and detected using a helium nanodroplet spectrometer (Figure 2.1). A schematic of this instrument is provided in Figure 2.2, which contains the three chambers relevant to the work contained in this thesis. The basic design of the instrument is based on a molecular beam apparatus, where droplets are produced in a free-jet expansion in the source chamber. The helium droplets are skimmed to form a beam which travels the length of the instrument. After production in the source chamber, the droplets are doped with the species of interest in a pick-up cell, followed by

irradiation with an infrared laser aligned coaxially with the droplet beam. The beam travels then through the ionization region of a quadrupole mass spectrometer, which acts as a detector.

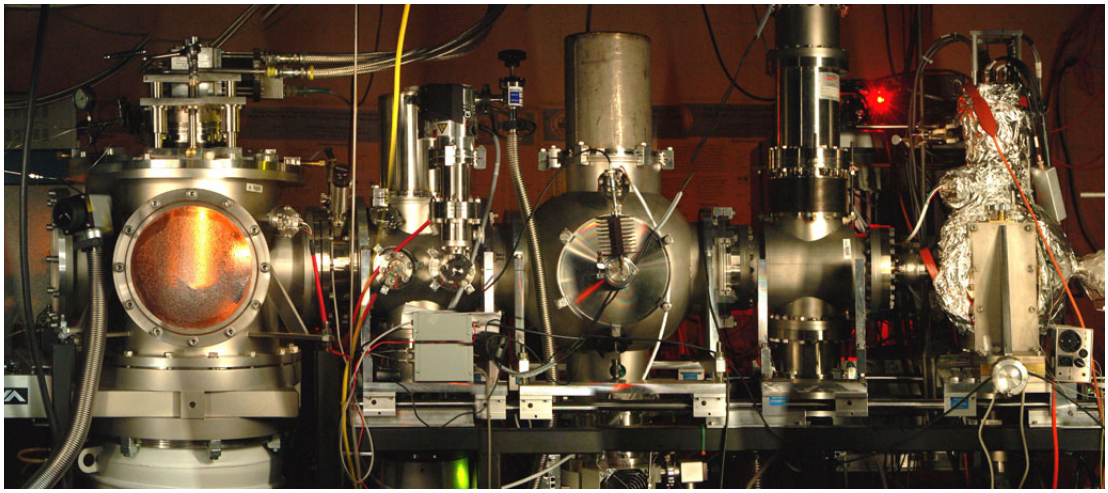

Figure 2.1. The Jäger group helium nanodroplet spectrometer. The source chamber is the leftmost chamber in the picture, followed by the doping chamber, the microwave and bolometer chambers (not described in this thesis), and the mass spectrometry chamber. Photo credit: Wolfgang Jäger.

In this chapter, I provide a detailed account of the experimental design and theoretical background necessary for helium nanodroplet spectroscopy. The chapter is organized to follow the experimental set-up provided in Figures 2.1 and 2.2. I begin with a description of helium nanodroplet production in the source chamber, followed by an examination of the properties of helium nanodroplets. Next I discuss the doping of the droplets, followed by mass spectrometry and laser depletion spectroscopy. A discussion of rovibrational spectroscopy in helium nanodroplets follows.

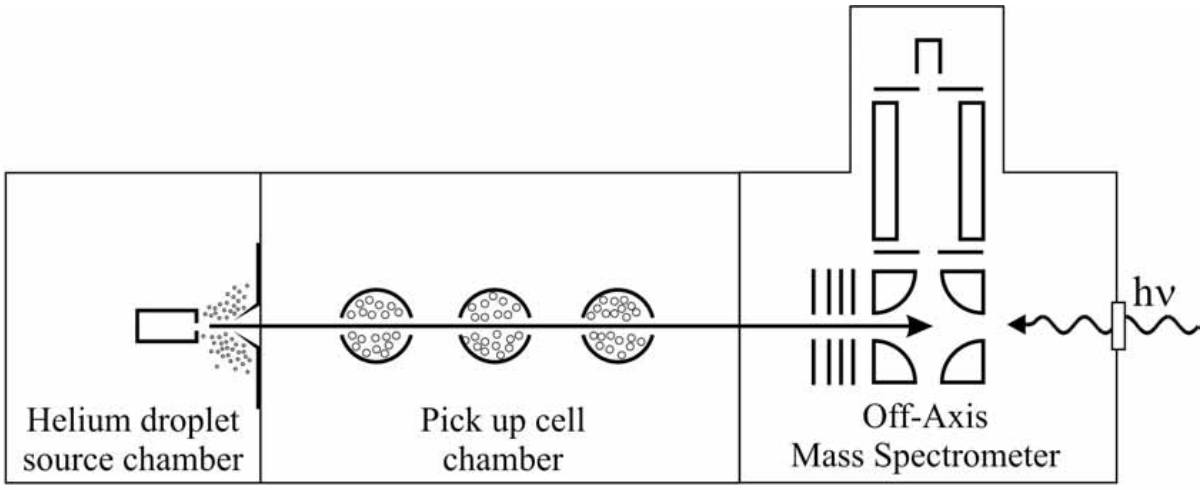

Figure 2.2. A simplified schematic of a helium nanodroplet spectrometer, showing the three chambers relevant to this thesis: the source chamber, the pick-up chamber, and the mass spectrometer chamber. Figure used with permission from ref. 2.

2.1 Droplet Production

Helium nanodroplets are produced in a continuous free-jet expansion by passing a sample of pre-cooled ultra-high purity helium (99.9990%) through a 5μm pinhole nozzle into a low-pressure chamber, referred to as the source chamber. The source chamber pressure is held around 2 x 10^{-5} Torr with the use of a high capacity diffusion pump. The helium used for droplet production is held at a pressure of between 20 and 80 bar (P_0), and is precooled to 10-30 K (T_0) with the cold head of a closed-cycle helium refrigerator, which is attached to the copper nozzle head. In the expansion, helium atoms cluster together in the high-pressure area immediately following the pinhole nozzle. Here, the pressure is high enough that the helium condenses into liquid droplets. Further from the nozzle, the helium pressure drops below the equilibrium vapour pressure, and the droplets undergo a period of evaporation. The temperature of the helium

droplets decreases as a result of evaporative cooling until they reach a temperature of about 0.37K, at which point the rate of evaporation becomes negligible.[4]

Droplet size, which is generally expressed in terms of the mean number of helium atoms per droplet, $\langle N \rangle$, is controlled by varying the nozzle temperature and stagnating pressure, T_0 and P_0. At a constant pressure, decreasing the temperature increases the average number of helium atoms per droplet. Conversely, at a constant temperature, increasing the pressure results in an increase in the average number of helium atoms per droplet. Thus, lower temperatures and higher pressures lead to larger droplet sizes.[5–7]

The number of helium atoms per droplet, and therefore the size, is given as a mean value because for each temperature and pressure, the droplets produced represent a log-normal distribution of sizes. The evidence for the droplet size distribution comes mainly from deflection in scattering experiments.[5–7] Although it is well understood that a broad distribution of droplet sizes is present in the helium droplet beam, control of the mean droplet size, by varying the nozzle temperature and stagnation temperature, is critical. For example, choosing conditions that favor the formation of droplet sizes below ~1500 He atoms/droplet results in significant inhomogeneous broadening of spectral lines of embedded dopants,[8] whereas having droplet sizes well above 5000 atoms per droplet can reduce spectroscopic sensitivity when using depletion spectroscopy (see section 2.5 of this chapter for a description of depletion spectroscopy). It has been shown via fluorescence spectroscopy that spectroscopic signal intensity drops off significantly below a nozzle temperature of about 15 K, where droplet sizes become too large to be effective for spectroscopy.[9]

It should be noted that there are three droplet production regimes for helium droplet sources. I have thus far described only the subcritical expansion regime, where the precooled

helium expands as a gas into the nozzle chamber, and then condenses into droplets through collisions in the high-pressure expansion zone, followed by evaporative cooling. Subcritical expansions are necessary for depletion spectroscopy since droplet sizes formed are typically below $\langle N \rangle < 30{,}000$. Lowering the nozzle temperature below the subcritical expansion conditions results in a supercritical expansion, which is the dispersion of liquid helium from the nozzle, and favors large droplets with $\langle N \rangle > 30{,}000$.[10] If the nozzle is cooled below 4 K with a stagnation pressure of 50 bar, the droplet production comes as a result of break-up of the liquid helium flow, resulting in very large droplets outside of the nanoscale size regime, $\langle N \rangle \approx 10^{10}$.[11]

All experiments reported in this thesis were done in the subcritical expansion regime, for the purposes of performing spectroscopic studies. Under average droplet production conditions used (T_0 = 20 K, P_0 = 40 bar), the droplet velocity is ~400 m/s,[5,12] corresponding to a time of flight to the quadrupole mass spectrometer of ~4 ms. With an initial cooling rate of ~10^{10} Ks^{-1}, droplets reach an equilibrium temperature of ~0.37 K prior to reaching the doping chamber.[4] Further, any dopants embedded in the droplets are cooled to the equilibrium temperature of the droplets, at least translationally, within ~100 ps.[3] Thus, the initial cooling rates of both the droplets and embedded impurities typically do not interfere with spectroscopic experiments.

2.2 Properties of Helium Droplets

As was mention in Chapter 1 of this thesis, when helium-4 is cooled below the lambda point, it becomes superfluid. Under the two-fluid model for bulk helium proposed by Landau[13] and Tisza,[14] the density of the superfluid increases as the temperature of helium is decreased

below the lambda point. Because helium nanodroplets equilibrate to about 0.37 K, the superfluid density is expected to be quite high.

Under the two-fluid model, the normal fluid fraction is considered to be excitations of the superfluid. An explanation of the quantum mechanical behavior of helium droplets is described using the liquid drop model (LDM), where helium droplets are treated as spheres with an assumed density equal to that of bulk helium.[4] For the spherical droplets, elementary excitations can be classified into surface modes and compressional modes. The surface modes, referred to as ripplons, result in a change in shape of the outer surface of the droplet. Ripplons can be described as capillary waves on the droplet surface, and affect the thermodynamics, such as evaporation, of the droplets at the experimental temperatures.

The compressional modes of the droplets, referred to as phonons, result in density changes inside the droplet. While even the lowest energy phonon modes remain unpopulated at the droplet temperatures, they do play a role in the cooling of dopants following excitation with resonant radiation. The density of states of rotons, which are phonons that sit within the minimum of the phonon excitation curve, have been shown to be involved in the rotational cooling of dopants.[15,16] If the rotational energy of the dopant matches with a high density of rotons in the phonon energy curve, relaxation is rapid and results in broadened rovibrational lines. The low density of roton states available for small rotors in the droplets is advantageous, as it results in longer excited state lifetimes and therefore narrow spectral lines.[2] Observed rovibrational lines in helium nanodroplets are typically homogeneously broadened as a result of rotational relaxation.

Other quantum excitations within the droplet are also possible including quantized vortices, and excitations based on the translational motion of the dopant.[3] In most cases, the

translational motion of the dopant does not result in the splitting of observed spectral lines as would be expected, given that the translational splitting is smaller than rovibrational linewidths within the droplet. Translational modes do, however, result in an energy well at the centre of the droplets, and thus closed shell dopants spend more time in the centre of the droplet than they do near the surface.[3] This phenomenon is analogous to a particle in a box, but extended to a 3-dimensional sphere.

Evidence of the presence of vortices in helium nanodroplets, which represent defects with a quantum of helium circulating about them, is given by Gomez *et al*.[17] In their experiment, xenon atoms were introduced to the droplets and become trapped in vortex cores. They are then imaged by femtosecond x-ray diffraction to reveal the structure of the vortex lattices inside the droplets. It is unclear how the quantized vortices may affect the spectroscopy of dopants inside the droplets.

2.3 Doping

Impurities are embedded in helium through collisional pick-up in the doping chamber of the helium nanodroplet apparatus.[18] The dopants are initially at room temperature, but cool rapidly to the equilibrium temperature of the droplet. The rapid cooling is a result of the high density of states in the helium droplet that are available to dopants at higher energies. When the dopant is captured, momentary heating results in the evaporation of helium atoms from the surface of the droplet until the equilibrium temperature is again reached. This rapid cooling of all degrees of freedom of the dopants is one of the many reasons why helium nanodroplets are a desirable spectroscopic matrix.[1]

Within the doping cells, pressures of dopant particles is generally on the order of $10^{-7} - 10^{-5}$ Torr. Under the low-pressure conditions in the doping cells, the pick-up of dopants by the droplets is sequential – that is, dopant particles are picked up one at a time.[19,20] This has important implications on the study of clusters in helium droplets. Because dopants inside helium nanodroplets are drawn together by long-range attractive forces, they often form high-energy, or metastable conformers.[20,21] The low energy available in the helium bath means that rearrangement to lower energy structures is typically not possible. It has even been shown that simply varying the pick-up order of dopants can result in different cluster structures being favored.[22,23] It should be noted, however, that precise control of cluster conformers is typically not possible, since many different conformers can form, and the percentage of each is a result of how they come together in the droplet.

The number of dopant particles present in each droplet can be described by Poisson statistics.[19] The relationship between the number of dopants, n, and the number density of dopants in the pick-up cell, ρ, is given by equation 1:

$$P_n = \frac{(\alpha L)^n}{n!} \exp(-\alpha L) \quad (1)$$

Where L is the length of the doping cell and $\alpha = \rho\sigma$, with σ representing the cross-sectional area of the droplet. The proportion of droplets containing clusters with higher numbers of monomers, n, therefore increases as the doping pressure increases.

2.4 Mass Spectrometry

The droplet beam passes through the doping chamber, then through subsequent chambers and finally terminates in the mass spectrometer chamber. Once the helium droplets enter the

mass spectrometer chamber, they pass through a coiled circular filament used for electron impact ionization, which occurs for helium droplets at electron impact energies > 70 eV (110 eV was typically used for the experiments reported in this thesis).[12,24] Much like the pick-up cross section of the droplet, the ionization cross section is roughly equal to the geometrical cross section of the droplet. Upon electron impact of the droplet, a helium atom is ionized to He^+, followed by rapid charge hopping. The charge hopping is terminated either through the formation of a He^+_n cluster, or when the charge migrates to the dopant. The localization of the charge results in a large release of energy and destruction of the droplet.[25] A mass spectrum of a helium nanodroplet beam shows peaks every 4 m/z resulting from the different ionized clusters of helium, but the peak at m/z = 8, representing He^+_2 is typically the largest. The different helium ion cluster sizes diminish in intensity with increasing m/z. Some differences in the relative intensity of different m/z values are related to the size of the droplets, although this effect is more pronounced for large helium droplets.[26] Following ionization, the ion fragments are guided towards the quadrupole mass filter to the multiplier which amplifies the signal and transmits it as a voltage.

I used a Quadrupole Mass Spectrometer (QMS) for many purposes while conducting my experimental work. First, the mass spectrum of undoped droplets provides an indication of the level of background impurities picked up by the droplets. Second, the overall signal strength at m/z = 8 is used to assess the quality of the alignment of the nozzle with the mass spectrometer. The nozzle is mounted onto a translation stage, and its position can be changed to improve alignment. Moving the nozzle while observing changes in the ion counts at m/z = 8 is a fast way to fine tune the overall nozzle alignment. Additionally, the mass spectrum is used in the initial stages of experiments with new dopants to assess doping efficiency.

2.5 Infrared Laser Depletion Spectroscopy

The QMS is also used as a detector for infrared laser spectroscopy. This is achieved by modulating an infrared laser beam which is aligned coaxially with the droplet beam, and detecting the total ion signal at different laser frequencies using lock in detection of the QMS signal at the laser modulation frequency (typically around 50 – 100 Hz). When the dopant absorbs an infrared photon, energy is dissipated in the helium bath following relaxation.[8,27,28] The energy is removed from the droplet via evaporation of helium atoms from the surface of the droplet. If the binding energy of one helium atom to the droplet is ~5 cm^{-1},[19] the absorption if one 4000 cm^{-1} photon results in the evaporation of about 800 helium atoms. Because relaxation and subsequent evaporation is fast on the timescale of the experiment, several absorption and evaporation events occur during the time of flight of the doped droplet prior to ionization. Each photon absorbed results in an overall decrease in the size of the droplets as helium atoms are lost to evaporative cooling. The net effect is the reduction of the cross-sectional area of the droplet. What is observed, in the case of resonance, is an overall decrease in the signal from the mass spectrometer due to a decrease in the ionization cross-section of the droplets. This type of action spectroscopy is therefore referred to as depletion spectroscopy due to the signal depletion that occurs when photons are absorbed by the dopants.

Depletion spectroscopy is required in helium nanodroplets due to the very low density of absorbers in the helium droplet beam. The diffuse beam and statistical doping of the droplets means that direct measurement of absorption or emission of infrared radiation is not practical or even possible given instrumental limitations. The change of size of the droplets, however, is relatively easy to detect using a QMS and lock-in detection.

A schematic of the experimental set-up I used for infrared spectroscopy of doped helium nanodroplets is given in Figure 2.3. The idler beam from a continuous OPO mid-infrared laser (described in detail in Chapter 3) is passed through two calcium fluoride windows which act as beam splitters. The small percentage of reflected light is passed into both a laser wavelength meter (Bristol Instruments, Model 621) for frequency measurements of the idler beam, as well as a power meter. The idler beam is then chopped at a rate of ~70 Hz and guided to the helium nanodroplet apparatus using gold coated mirrors. A focusing lens with a 1 m focal length is used to increase the intensity of the infrared beam on the droplet beam. The idler beam passes through a calcium fluoride window at Brewster's angle to reduce reflection and into the droplet apparatus such that it overlaps with the droplet beam. The alignment of the laser with the path of the helium droplet beam is crucial for spectroscopy, and is performed by finely adjusting the position of the guiding mirrors until the beam passes through the skimmer and can be observed hitting the nozzle. While the infrared laser is of course invisible to the eye, when operating the OPO at low power (below the threshold of the internal gain medium), red laser light is transmitted and can be used for visual alignment.

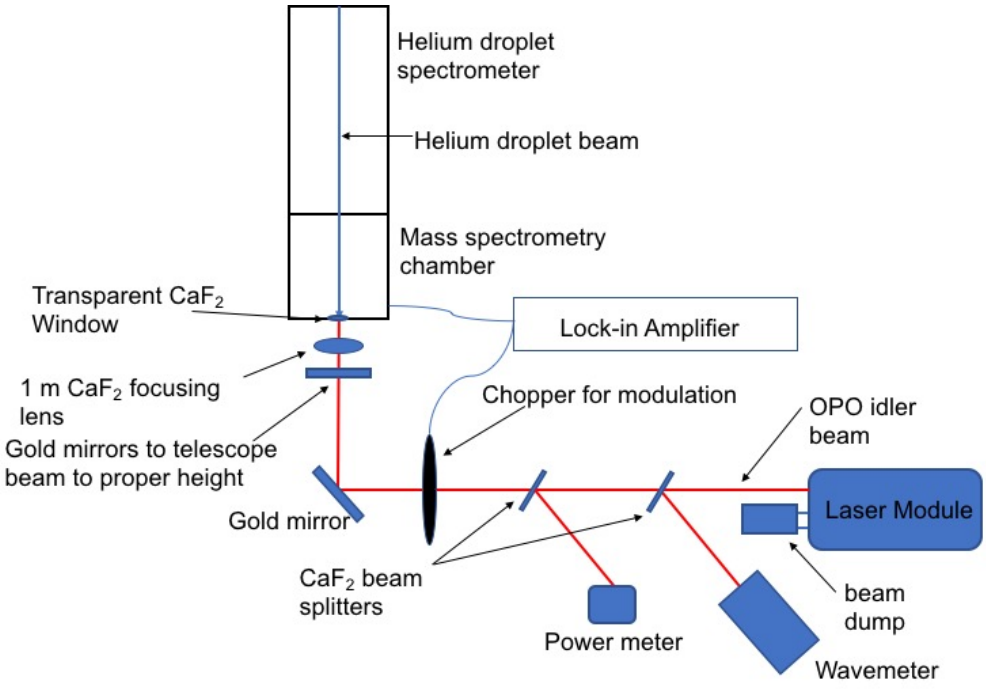

Figure 2.3. The experimental set up of the infrared laser for spectroscopy of dopants in helium nanodroplets.

2.6 Rovibrational Spectroscopy of Dopants in Helium Nanodroplets

One of the major advantages of the helium nanodoplet matrix compared to solid rare gas matrices, is that the superfluid nature of the helium allows for nearly free rotation of the embedded impurities. The helium bath interacts with the dopants only very weakly, such that the symmetry of the molecule is not affected by the matrix. Symmetry effects can cause splitting of spectral lines, as is often observed in solid rare gas matrices. Further, the nearly free rotation of species embedded in the droplets often results in rotationally resolved vibrational spectra that appear very similar to the gas phase.[28] Band origin shift of vibrational modes in helium droplets are generally < 1 cm^{-1} from the gas phase values, compared to the much larger shifts observed in solid rare gas matrices.[2]

The primary difference of rovibrational spectra of dopants in helium droplets compared to the gas phase is the spacing of the rotationally resolved lines. Adiabatic following of helium density closest to the dopant results in an increase in the moment of inertia of the rotor. Rotational constants of molecules are inversely proportional to the moment of inertia, *I*. The relationship between the moment of inertia of a linear rotor and its rotational constant, B, is given in equation 2:

$$B = \frac{\hbar}{4\pi cI} \tag{2}$$

Here, *c* is the speed of light and $\hbar$ is the reduced Planck constant. Adiabatic following of the dopant increases the moment of inertia, and decreases the rotational constant, which in turn decreases the line spacing of rotationally resolved lines.[16]

The reduction of the rotational constants in helium nanodroplets is referred to as renormalization. For most rotors, the rotational constants in helium droplets are renormalized to, on average, about 0.3 of the gas phase value.[2] For smaller rotors, or for rotations about an axis with a low moment of inertia, the rotors are thought to move too quickly for adiabatic following. This results in a much smaller renormalization of the rotational constants, which approach the gas phase values with increasing rotational energies.[2] For rotors within the adiabatic following regime, there is still much variation in the extent of renormalization of rotational constants. This is a result of the anisotropy in the dopant-helium interaction potential.[2] Larger anisotropy results in an asymmetrically distributed helium density following the rotor, and larger renormalization values.

2.7 Conclusions

I have thus far outlined the experimental considerations for infrared spectroscopy of dopants in superfluid helium nanodroplets relevant to this thesis. The highlighted experimental details include droplet production, doping and detection. I have also included discussions on the quantum mechanical nature of the superfluid helium nanodroplets, as this has important implications on the measurement of rovibrational spectra of dopant species. The experimental aspects discussed in this chapter provide details to the experimental design used in Chapters 4 to 7. More details on the laser used for infrared spectroscopy are given in Chapter 3.

References

[1] J. P. Toennies, A. F. Vilesov, *Angew. Chem. - Int. Ed.* **2004**, *43*, 2622–2648.

[2] M. Y. Choi, G. E. Douberly, T. M. Falconer, W. K. Lewis, C. M. Lindsay, J. M. Merritt, P. L. Stiles, R. E. Miller, *Int. Rev. Phys. Chem.* **2006**, *25*, 15–75.

[3] F. Stienkemeier, K. K. Lehmann, *J. Phys. B At. Mol. Opt. Phys.* **2006**, *39*, R127–R166.

[4] D. M. Brink, S. Stringari, *Z. Für Phys. At. Mol. Clust.* **1990**, *15*, 257–263.

[5] M. Lewerenz, B. Schilling, J. P. Toennies, *Chem. Phys. Lett.* **1993**, *206*, 381–387.

[6] J. Harms, J. P. Toennies, F. Dalfovo, *Phys. Rev. B* **1998**, *58*, 3341–3350.

[7] E. L. Knuth, U. Henne, *J. Chem. Phys.* **1999**, *110*, 2664–2668.

[8] S. Grebenev, M. Hartmann, M. Havenith, B. Sartakov, J. P. Toennies, A. F. Vilesov, *J. Chem. Phys.* **2000**, *112*, 4485–4495.

[9] F. Stienkemeier, O. Bünermann, R. Mayol, F. Ancilotto, M. Barranco, M. Pi, *Phys. Rev. B* **2004**, *70*, 214509.

[10] J. Harms, J. P. Toennies, E. L. Knuth, *J. Chem. Phys.* **1997**, *106*, 3348–3357.

[11] R. E. Grisenti, J. P. Toennies, *Phys. Rev. Lett.* **2003**, *90*, 234501.

[12] H. Buchenau, E. L. Knuth, J. Northby, J. P. Toennies, C. Winkler, *J. Chem. Phys.* **1990**, *92*, 6875–6889.

[13] L. Landau, *Phys. Rev.* **1941**, *60*, 356–358.

[14] L. TISZA, *Nature* **1938**, *141*, 913.

[15] M. Hartmann, F. Mielke, J. P. Toennies, A. F. Vilesov, G. Benedek, *Phys Rev Lett* **1996**, *76*, 4560–4563.

[16] K. K. Lehmann, *J. Chem. Phys.* **2001**, *114*, 4643–4648.

[17] L. F. Gomez, K. R. Ferguson, J. P. Cryan, C. Bacellar, R. M. P. Tanyag, C. Jones, S. Schorb, D. Anielski, A. Belkacem, C. Bernando, et al., *Science* **2014**, *345*, 906.

[18] A. Scheidemann, J. P. Toennies, J. A. Northby, *Phys. Rev. Lett.* **1990**, *64*, 1899–1902.

[19] M. Lewerenz, B. Schilling, J. P. Toennies, *J. Chem. Phys.* **1995**, *102*, 8191–8207.

[20] K. Nauta, R. E. Miller, *J. Chem. Phys.* **2000**, *113*, 9466–9469.

[21] K. Nauta, R. E. Miller, *Science* **1999**, *283*, 1895–1897.

[22] N. Pörtner, A. F. Vilesov, M. Havenith, *Chem. Phys. Lett.* **2001**, *343*, 281–288.

[23] M. Hartmann, A. Lindinger, J. P. Toennies, A. F. Vilesov, *Chem. Phys.* **1998**, *239*, 139–149.

[24] A. Scheidemann, B. Schilling, J. P. Toennies, *J. Phys. Chem.* **1993**, *97*, 2128–2138.

[25] B. E. Callicoatt, K. Förde, L. F. Jung, T. Ruchti, K. C. Janda, *J. Chem. Phys.* **1998**, *109*, 10195–10200.

[26] L. F. Gomez, E. Loginov, R. Sliter, A. F. Vilesov, *J. Chem. Phys.* **2011**, *135*, 154201.

[27] R. Fröchtenicht, J. P. Toennies, A. Vilesov, *Chem. Phys. Lett.* **1994**, *229*, 1–7.

[28] M. Hartmann, R. E. Miller, J. P. Toennies, A. Vilesov, *Phys. Rev. Lett.* **1995**, *75*, 1566–1569.

Chapter 3: Infrared Laser Tuning Automation

3.0 Introduction

For the Jäger group's continuous-beam helium nanodroplet machine, a continuous wave (cw), high output power, continuously tunable mid-infrared laser is required for high-resolution rovibrational spectroscopy. A cw laser maximizes the exposure of the continuous beam of helium droplets to infrared radiation; pulsed laser sources dramatically reduce the duty cycle and therefore spectroscopic sensitivity. The low optical density of absorbers in the beam also requires a high output power (~ 1-3 W) to ensure that significant absorption and therefore beam depletion occurs. Finally, for high-resolution, rotationally resolved spectra, the laser must be continuously tunable. While there are many mid-infrared lasers on the market, there are few that meet all of the above criteria. The laser used for this application in the Jäger lab, and indeed many other helium nanodroplet groups, is the Lockheed-Martin Aculight ARGOS 2400-SF-15 system.[1–3]

The Aculight Argos 2400 series laser is a cw, tunable optical parametric oscillator (OPO) mid-infrared laser. It consists of a 15 mW Yb-doped fiber seed laser (1064 nm) (Koheras), which is amplified to 15 W using a diode pumped fiber amplifier (IPG photonics), and used as the pump laser.[2] The pump laser is fed via fiber optic cable into the module cavity and passed through a periodically-poled lithium niobate (PPNL) crystal, which converts the source beam into an idler beam and a signal beam, whose relationship is given in equation (1):

$$\frac{1}{\lambda_P} = \frac{1}{\lambda_S} + \frac{1}{\lambda_I} \quad (1)$$

Where λ_P is the pump laser wavelength, λ_S is the signal beam, and $\lambda_I$represents the idler beam, which is the beam used in the experiment (Fig. 3.1).

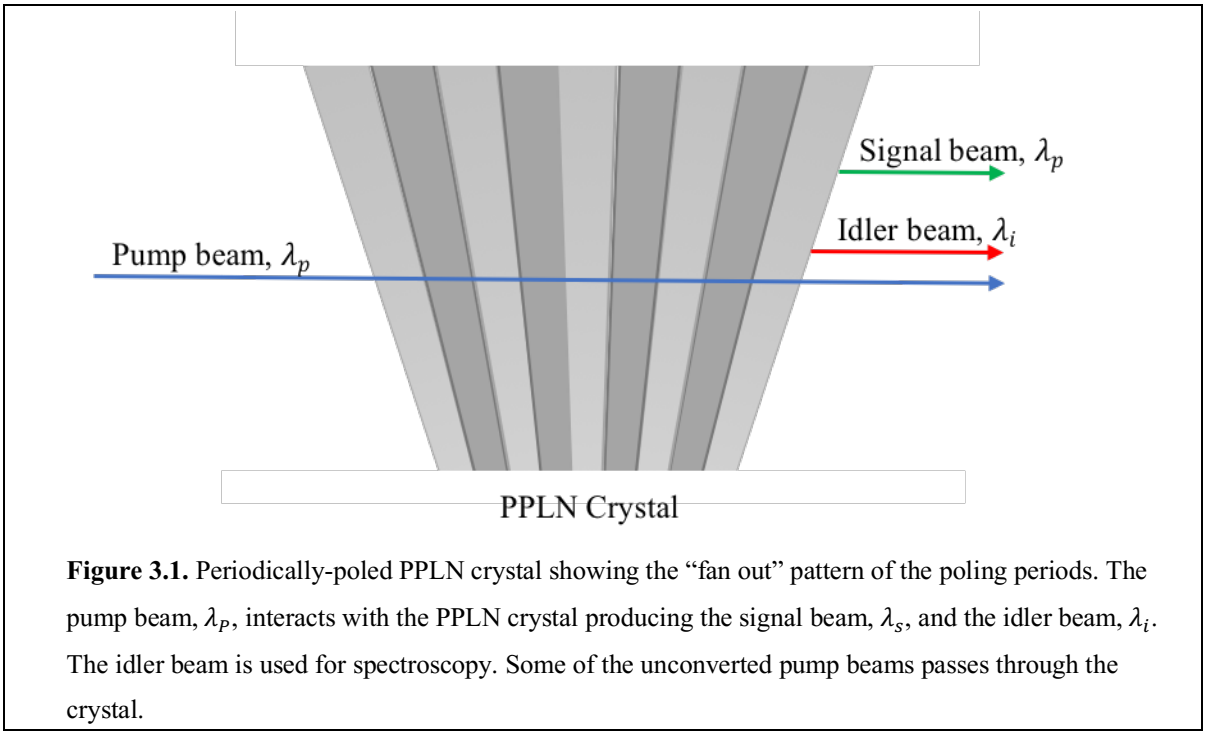

Figure 3.1. Periodically-poled PPLN crystal showing the "fan out" pattern of the poling periods. The pump beam, λ_P, interacts with the PPLN crystal producing the signal beam, λ_s, and the idler beam, λ_i. The idler beam is used for spectroscopy. Some of the unconverted pump beams passes through the crystal.

The design of the Aculight ARGOS 2400-SF-15 is such that tuning the frequency requires the coordination of three distinct processes to achieve fine (continuous), intermediate

and course tuning. Direct from the manufacturer, this laser system requires full manual tuning of each of the three elements. The laser can, however, be connected to a computer system, and two of the tuning elements can easily controlled by a basic LabVIEW virtual instrument (VI). The coarse tuning however, requires that a user physically translate an internal crystal using a hex key inserted into the laser module. Crystal translation must be frequently performed to ensure good output power, as well as to cover the necessary wavelength regions for recorded spectra. The user must therefore constantly intervene throughout the measurement of a spectrum, leading to significant time-commitments. In 2012, a method for automating the tuning of the Aculight ARGOS 2400-SF-15 was developed by Morrison *et al.* in the Douberly group, University of Georgia, resulting in a substantial reduction in the amount of user intervention required, and therefore a greatly reduced time-commitment.[4] To increase the efficiency of experiments in the Jäger nanodroplet lab, I automated the tuning of our laser system following the Douberly group's method. This chapter documents my implementation of the Douberly tuning automation method into our laser system. Prior to the practical details of automation, the necessary background details of the laser system are detailed below.

3.1 Optical Parametric Oscillation

Frequency conversion of the pump beam into the signal and idler beams in the Aculight laser is achieved with the use of a non-linear optical technique referred to as optical parametric oscillation. Non-linear optical techniques require the use of anisotropic crystalline materials in which the polarization, $\boldsymbol{P}$, responds non-linearly to an intense electric field, $\boldsymbol{E}$. The polarization resulting from an electric field can be written as follows:

$$\boldsymbol{P} = \varepsilon_0\left[\chi^{(1)}\boldsymbol{E} + \chi^{(2)}\boldsymbol{E}^2 + \chi^{(3)}\boldsymbol{E}^3 \ldots\right], \quad (2)$$

where ε_0 is the electric permittivity of free space, and $\chi^{(n)}$ represents the susceptibility of the medium – a proportionality constant which indicates the degree of polarization of the medium induced by an electric field. The first term, $\chi^{(1)}\boldsymbol{E}$ describes the linear response of polarization in the presence of an electric field, whereas $\chi^{(2)}\boldsymbol{E}^2$ describes the second order non-linear response. Thus, the polarization of a material induced by an electric field is the sum of the first order (linear) and higher order (non-linear) components. At low field strength, the linear response dominates, but at higher field strength, the non-linear effects become more important.[5]

In the presence of a strong optical wave provided by a laser at frequency ω_p (referred to as the pump) the non-linear polarization field arising from $\chi^{(2)}$ can result in the production of a wave at frequency ω_s, referred to as the signal wave. Again through the $\chi^{(2)}$ interaction, a third wave at frequency ω_i (referred to as the idler wave) is produced by the interaction of ω_p and ω_s. Both waves arise from random noise amplified by the interaction of the pump beam and the non-linear optical medium, and this amplification is referred to as parametric amplification. The precise frequencies of the idler and signal waves are dictated by the conservation of energy, where:

$$\omega_p = \omega_s + \omega_i \quad (3)$$

To enhance gain of the idler and signal waves, the non-linear crystal is placed in a cavity, resulting in the phenomenon known as optical parametric oscillation (OPO).[5] In the Aculight Argos OPO laser, the cavity is referred to as singly resonant, meaning it is resonant with only the signal beam.[6] The cavity enhances the interaction between ω_p and ω_s, thus increasing the gain of both of ω_s and ω_i. A basic singly-resonant cavity is shown in Figure 3.2. In the Aculight Argos

OPO, the idler beam is the beam traditionally used for the purpose of spectroscopy. The Aculight Argos OPO laser makes use of what is known as a bow-tie cavity (see Fig. 3.2). The purpose of

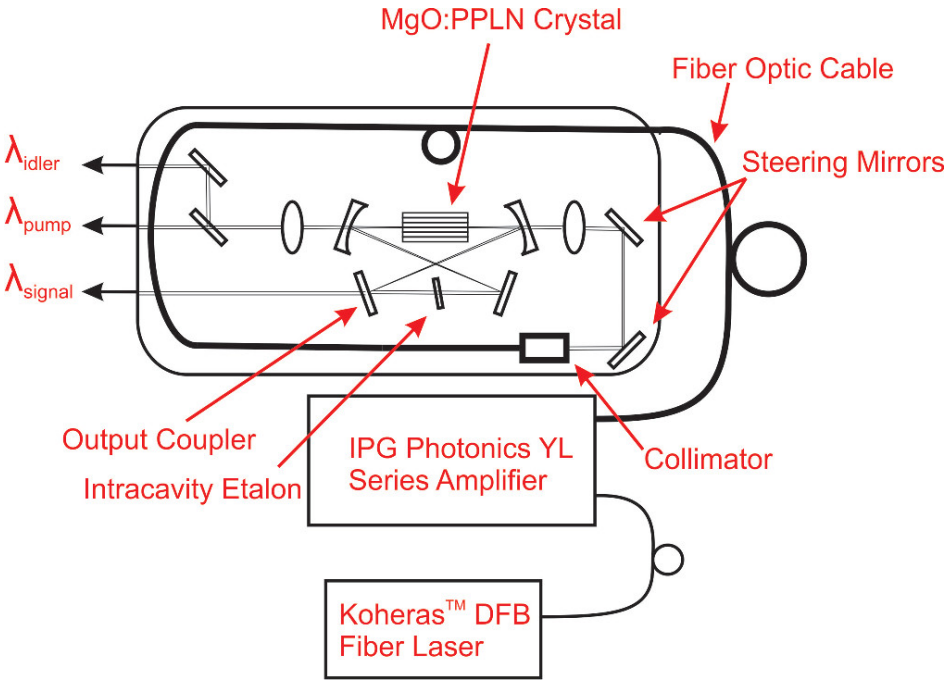

Figure 3.2. A schematic of the inside of the OPO module, including the bowtie cavity and relevant optics. Figure used with permission from ref. 4.

the bow-tie cavity is to increase gain in the PPLN crystal as well as to provide a pathway for the signal beam to pass through a YAG or fused-silica etalon, which is necessary for single mode operation.[2] The intracavity etalon is described further below, as it plays a crucial role in frequency tuning.

3.2 Tuning basics

OPO lasers are desirable for spectroscopy because the idler and signal beams can be tuned over a broad range of frequencies. For high-resolution spectroscopy, continuous tuning

over a range of frequencies is necessary. Continuous tuning of the idler beam is achieved in the Aculight Argos OPO laser by coordinating three different tuning methods. Coarse tuning results in wavelength hops of 10 – 20 nm, intermediate tuning is done in steps of ~1 nm, and fine tuning can cover a continuous range of about 2 nm, filling in the wavelength gaps left by the coarse and intermediate tuning methods.

Course tuning is achieved by translating the intracavity periodically poled lithium niobate (PPLN) crystal, which is the gain medium for the OPO. The PPLN crystal is a nonlinear material in which the poling period of the crystal is engineered to produce nonlinear frequency conversion of the pump beam. The poling period of the poled crystal varies linearly across its width, resulting in a "fan-out" appearance (Fig. 3.1). With the pump beam in a fixed position, translating the PPLN crystal up or down results in a change of the poling period, and thus a change in the wavelength of maximum gain. Physically, the crystal translation and thus rough tuning, is achieved by manually turning a translation screw on the laser module housing using a hex key.

Intermediate tuning of the OPO laser is achieved by rotating the intracavity etalon in the range of ±3.0° from its perpendicular arrangement with respect to the signal beam in the OPO cavity, depending on the module. Due to the index of refraction of the etalon, small changes in the etalon angle in the cavity result in small changes of the length of the cavity, and thus a change in the resonant signal frequency. As a result, the signal beam hops to another longitudinal cavity mode. This results in mode hops of around 1 cm^{-1} of the signal beam. The intracavity etalon is also crucial for insuring single-mode operation of the OPO laser.

Fine tuning is required to cover the range of frequencies between the mode hops that occur with tilting the intracavity etalon. The pump laser frequency can be tuned continuously over a ~100 GHz range by piezo strain of the fiber pump laser. Piezo strain is altered using an external piezo driver (Thorlabs) and varying the voltage applied from 0-90 V (B module) or 0-200 V (C module).

3.3 Automation

For continuous tuning, each of the three tuning methods (course, intermediate, and fine) must be used together. In the Jäger nanodroplet lab, I continuously tuned the laser by automating the intermediate and fine tuning methods, and manually adjusting the crystal position as needed for data collected in chapters 4 and 5. This required a great deal of user intervention, as the crystal position must be adjusted to achieve sufficient output power each time the etalon angle is changed. When the crystal position and the etalon angle are not adjusted together, a mismatch in the gain curve of the PPLN crystal and the cavity modes results in low power output of the idler wave as shown in Figure 3.3. For fully automated tuning it is not sufficient to merely control the PPLN crystal position via computer; the shift in the etalon angle and the motor must be controlled simultaneously to maintain matching of the PPLN gain curve with the intracavity etalon resonance. A method for full automation was developed by the Douberly group in 2012, and I have implemented it in order to improve the efficiency with which spectra are collected. Data in chapters 6 and 7 were collected with fully automated tuning. This section outlines the procedure and data collected during automation of the ARGOS OPO modules B and C. An example spectrum is given in the next section to highlight the success of the automation.

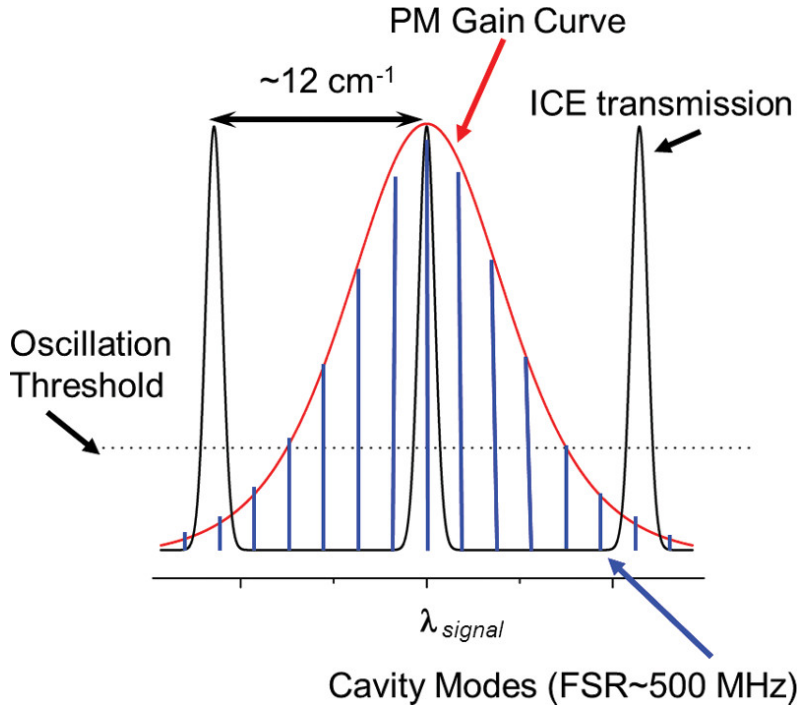

Figure 3.3 – Schematic showing the gain curve of the PPLN (red), the cavity modes (blue) and the intracavity etalon (ICE) transmission curve (black). In the above figure, the gain curve is matched appropriately with the etalon curve. Physical translation of the PPLN crystal would shift the gain curve, resulting in a mismatch between the two curves. Figure used with permission from ref. 2.

For the purpose of automation of laser tuning and recording of infrared spectra a National Instruments PCI-6221 DAQ board connected to an NI BNC-2090 rack-mounted terminal block was purchased and used for all analogue input (and output) channels required. I used lock-in detection of the signal from the mass spectrometer, and the lock-in detector signal was connected to the BNC-2090, along with a Thorlabs power meter which monitored the idler laser power, the Lakeshore temperature sensor to display nozzle temperature data, and the piezo driver (both input and output for the piezo were connected to the BNC-2090). The wavemeter and stepper

motors (see below) are connected to the computer via USB. Finally, the OPO controller is connected to the computer via an NI PCI-8430 (RS 232) interface.

3.3.1 Stepper motor configuration

Following Morrison *et al.*[4], a linear actuator (Figure 3.4) was constructed and attached externally to the laser module for translation of the crystal. The actuator consists of a stepper motor (Anaheim Automation 23MD series) that is attached to the translation screw for the PPLN crystal. The stepper motor rotates a hex key, which is attached using a flexible coupling to reduce strain on the PPLN crystal. The actual design of the actuator has been simplified from the version presented by Morrison *et al.*, in that it consists of a spring in a brass housing to

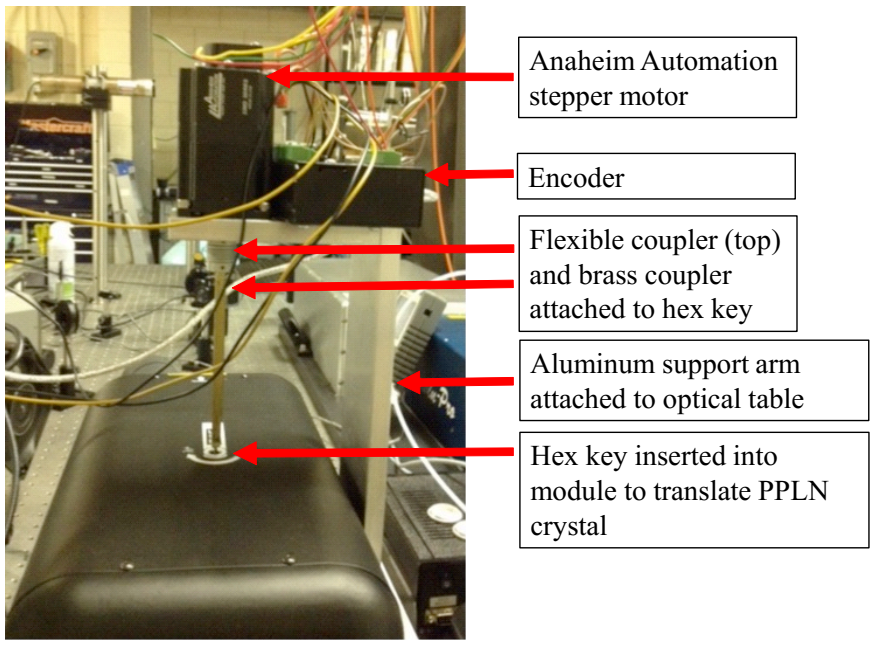

Figure 3.4. A labeled photograph of the stepper motor assembly used for automatic translation of the PPLN crystal. The stepper motor is supported by the aluminum arm, and attached to a flexible coupler followed by a brass coupler with an internal spring to allow for vertical movement of the hex key as the PPLN is translated up and down. The stepper motor is controlled via an encoder which is connected through USB to a computer.

accommodate the linear motion of the hex key, rather than a threaded screw and bushing. With this configuration, I determined that just one flexible coupler was required, further simplifying the design.

The stepper motor encoder is connected to the laboratory computer via USB, and the precise motor position can be determined. During the first phase of automation I recorded a calibration curve for each module (B and C), to determine the variation of the wavelength with motor position, using the "motoring_for_curve_make" LabVIEW VI provided by the Douberly group. The lowest laser frequency was set as the zero position of the motor, and then following Morrison *et al*., the intracavity etalon was removed in order to simplify the collection of the stepper motor calibration curve. Outliers were then removed from the raw data, resulting in the calibration curves presented in Figure 3.5. Each calibration curve was fitted using a 4^{th} order polynomial, and the constants are given in Table 3.1. The constants derived from the 4^{th} order polynomial fit are used for tuning using a LabVIEW program, detailed in section 3.3.3.

Table 3.1 – Results from the 4^{th} order polynomial fit for modules B and C. These values were put into the LabVIEW VI "ScanArgos" for proper control of the stepper motor during scanning.

Polynomial fit variables	Fitted Values	
	Module B	Module C
y-Intercept	-2.23471×10^{6}	-2.74071×10^{6}
1	1.95785×10^{3}	3.16631×10^{3}
2	-6.55390×10^{-1}	-1.44151
3	1.01463×10^{-4}	3.09313×10^{-4}
4	-6.09054×10^{-9}	-2.5829410^{-8}

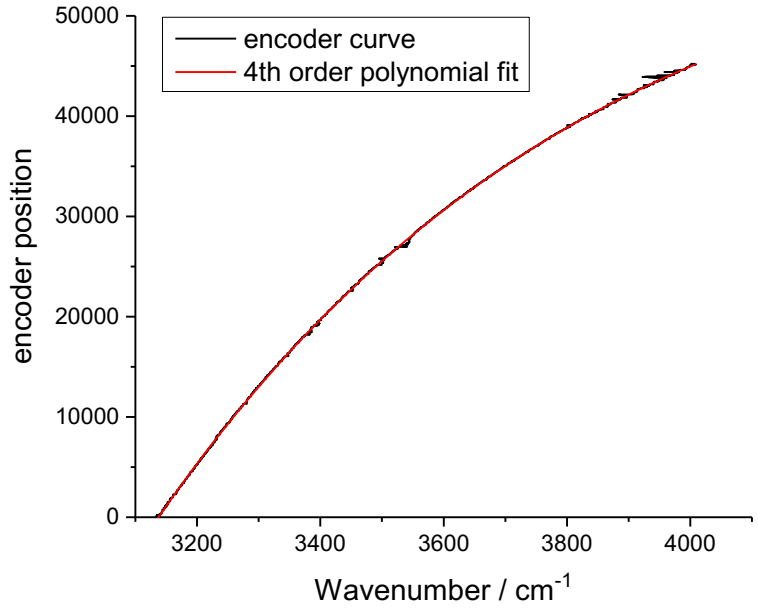

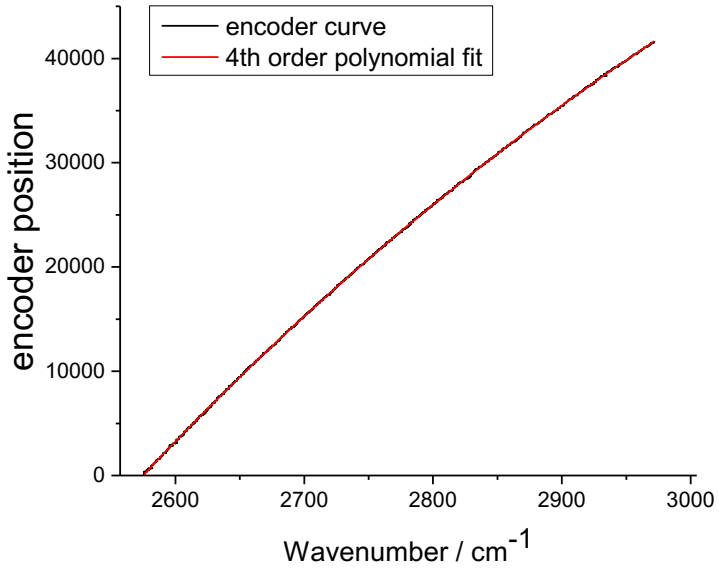

Figure 3.5. Motor encoder curves for modules B (top) and C (bottom). Both curves were recorded with the intracavity etalon removed. The adjusted R-squared for the top curve is 0.99993 and for the bottom, 0.99997. Both curves were recorded at a crystal temperature of 55°C.

3.3.2 Etalon curves

After completion of the stepper motor calibration curves, I put the intracavity etalon back into the laser cavity for both module B and C in order to generate etalon curves. To generate the etalon curves, the etalon angle was varied between ±3.0° (C module) and ±1.75º (module B) in steps of 0.01º while recording the frequency from the wavemeter. The two etalon curves are shown in Figure 3.6. The purpose of the etalon curve is to determine the range of etalon angles required to cover the desired spectral range, as well as the angle steps needed for a modehop. As seen in figure 7, a range from -1.5 to +2º was chosen for module C with steps of 0.15º, and a range of -0.6 to +0.7º with steps of 0.15º was chosen for module B. The angle step is chosen so that each change of etalon angle results in a hop of the wavelength. If the etalon angle step was too small, the wavelength would not change, and the same wavelength data would be recorded extraneously. It should be noted that the recommended etalon angle range for each module also sits about the 0º mark. When etalon angle is too far from 0º for an extended period of time, overheating of the cavity block can occur.

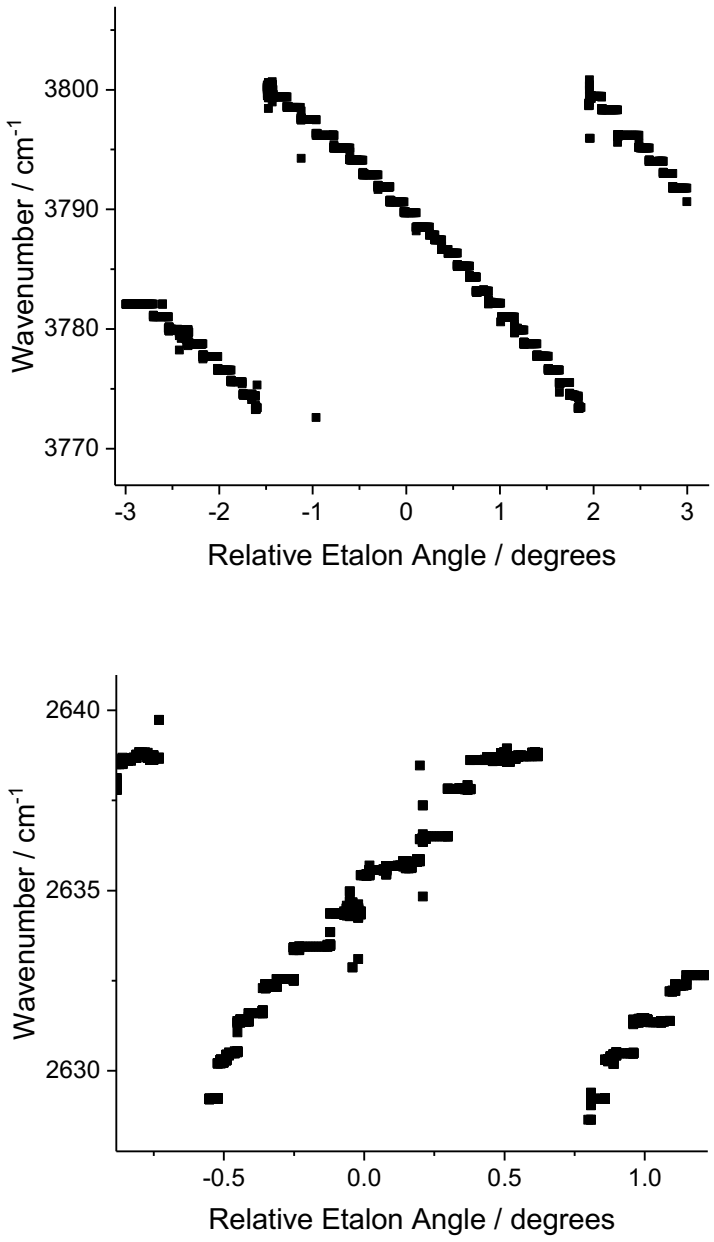

Figure 3.6. Etalon curves for module B (top) and module C (bottom). Each curve shows steps corresponding to mode hops that accompany etalon angle changes. The two curves were used to determine the etalon angle range and hop required for scanning.

3.4 Scanning

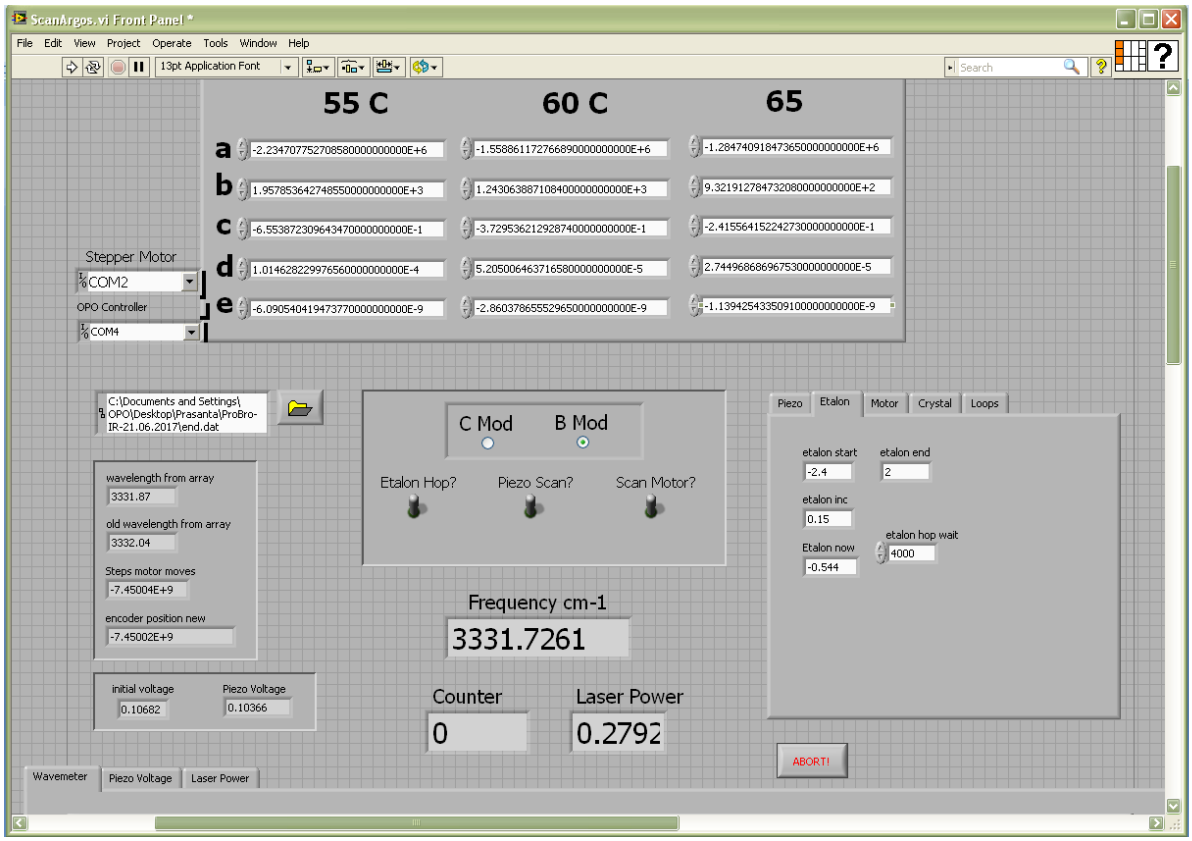

Figure 3.7. The front panel of the ScanArgos VI used for automated tuning and the recording of infrared spectra. See the text for details.

The Douberly group provided me with the ScanArgos.vi created in LabVIEW to use for automated scanning, as well as several other VIs that were used for the creation of calibration curves. None of the VIs were ready to use as provided, so I configured them to communicate with our instrumentation using National Instruments Measurement and Automation Explorer (NI MAX). The constants generated from the 4th order polynomial fit of the encoder curves that I generated were input into the ScanArgos.vi, as well as the etalon range and step for each module. An example of the ScanArgos.vi front panel is given in Figure 3.7. Below I provide a summary

of the scanning procedure and some of the relevant details of the Vis used in the process. A more general, expanded explanation of the VIs can be found in the supplemental information of ref. 4.

In the front panel shown in Figure 3.7, the 5 parameters generated from the 4^{th} order polynomial fit (see Table 3.1) are entered for module B module under the 55 C tab, which is the crystal temperature at which the encoder curve was recorded. ScanArgos.vi detects the crystal temperature and uses the parameters under the appropriate column. Note that I have not recorded the encoder curves at temperatures of 60 or 65°C, as I had some difficulty maintaining the crystal temperature at 60°C (or higher). Recording encoder curves at higher temperature is a future endeavor that will potentially require a repair to module B. Higher temperature encoder curves for module C have not yet been attempted.

Underneath the encoder curve values, Figure 3.7 shows that module B has been selected, and the three toggle switches for etalon hop, piezo scan, and motor scanning are in the on position indicating the program is set for fully automated scanning of all three tuning elements. Below the toggle switches are data readouts for the frequency in cm^{-1}, laser power (which is recorded by splitting the idler beam and using a Thorlabs power meter for measuring power), and the counter, which indicates the number of data points. Beside the toggle switches are a number of tabs, of which I will describe the two I use most frequently. First, the etalon tab contains the etalon start and stop points, increment, and the hop wait time. The wait time is shown as being set to 4000 ms, which is how long the program pauses before collecting more data after each etalon hop. This is required due to the small delay in wavelength hop after an etalon change. The Piezo tab contains information about the start and stop voltages for the piezo scanning, as well as the voltage increment, which changes the time required to scan between etalon hops. In the piezo

tab is an option to scan using either a triangle or sine waveform. I tried scanning with both waveform types and found that the sine waveform worked best for piezo tuning.

In order to being scanning and recording spectra, the “Bristol_Example” VI (provided by the Bristol Instruments with purchase of their wavemeter) must be running in the background to provide the frequency data for the ScanArgos VI. To initialize scanning, the OPO laser is turned on, and the “Bristol_Example” VI is initiated. Then another VI (also provided by the Douberly group) called “encoder_go_to_value” is used to position the motor such that the scan starting frequency is adjusted as desired, and also to help maximize the power output of the laser at the currently selected etalon angle. This essentially amounts to correctly matching the PPLN crystal and etalon gain curves in order to set the scan up to continue matching these curves each time the etalon angle is changed. The “encoder_go_to_value” VI is then stopped and closed, and the ScanArgos VI can be run to commence scanning and recording of infrared spectra.

Figure 3.8 shows the continuously displayed output during the scanning, with time as the x-axis, and frequency in cm^{-1} along the y-axis. The upper window shows the sine waveform used for piezo tuning. The voltage is first swept up, followed by an etalon hop, and then down again to ensure coverage of the frequencies between each hop. The screenshot in Figure 3.8 was taken while recording the bound OH stretching region of the hydrogen peroxide dimer, detailed in Chapter 6. The bottom panel shows the recorded data through time. The data points are automatically recorded to a file that can be opened with a data management program such as Origin or Excel. Visualizing the recorded spectrum is achieved by plotting the recorded data. The recorded data from the ScanArgos VI includes 8 columns of data. The first column is the data from the lock-in amplifier which we use to demodulate the signal from the quadrupole mass

spectrometer. Next is the laser power, the nozzle temperature, the wavemeter reading, the motor encoder position, etalon angle, piezo voltage and crystal temperature.

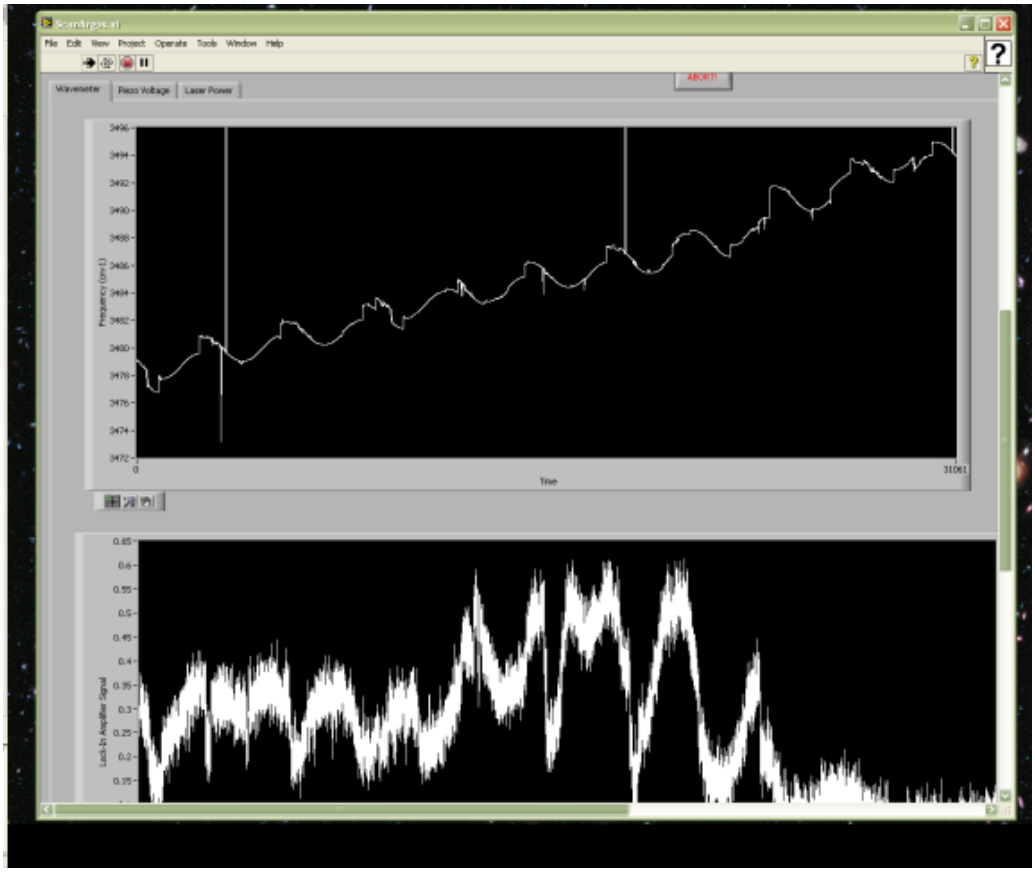

Figure 3.8. Display from ScanArgos during scanning. The upper panel shows frequency scanning with time, while the lower panel displays the data recorded from the lock-in amplifier over the same time span.

The data from scanning can either be manually worked up using a data management program (I used Origin exclusively), or the "dataworker" VI can be used. This VI can stitch together multiple data files, smooth and power correct the data. This is helpful because of the somewhat complicated structure of the data file. Data from the wavemeter is recorded at 5 Hz,

representing 5 data points per second.Each wavemeter reading is repeated 4 times, since all other analogue data is recorded at a rate of 20 Hz, resulting in a large amount of data for even a short scan.

3.5 Example spectrum

I tested the laser automation setup by recording the spectra of many different dopants embedded in helium nanodroplets to work out any bugs or other issues with my experimental set-up. Figure 3.9 shows one such example spectrum recorded over a ~15 cm range, which took about 25 minutes to record with no user intervention. For the spectrum, droplets were doped with 1.6 x 10^{-6} Torr of naphthalene, with a nozzle temperature of 19 K, and a helium backing pressure of 40 barr. The spectrum was recorded merely as a proof of concept, and I have not yet assigned all of the observed lines.

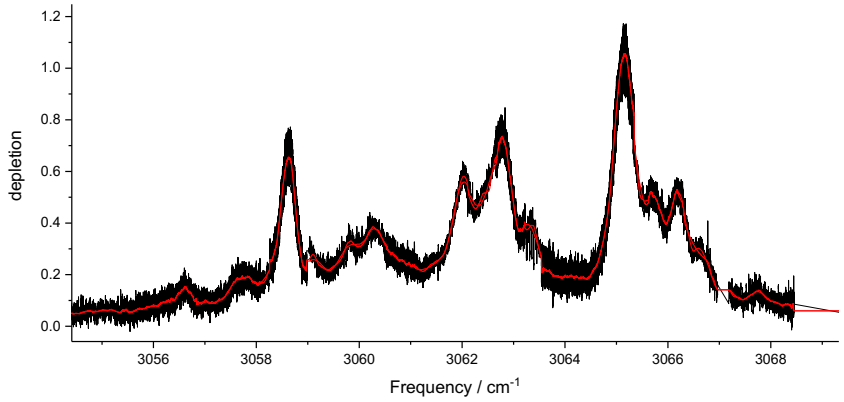

Figure 3.9. An example spectrum of naphthalene embedded in helium nanodroplets collected by the automated scanning of module C. The red line represents smoothed data that was added to guide the eye.

3.6 Conclusions

This chapter details the automation of an Aculight Argos 2400 series OPO laser I conducted in the Jäger helium nanodroplet lab as part of my PhD work. I followed the procedure set in the supplemental information of ref. 4 by Morrison *et al.*, which required an overhaul of the way scanning was conducted, and data was collected in the Jäger lab. Two OPO laser modules were used during automation: the B module and the C module, which together provide frequency coverage from 2560 – 4000 cm^{-1}. For the purpose of automation, stepper motor curves and etalon angle curves were generated, and these were used to input the required data into the ScanArgos VI provided to me by Gary Douberly. Both the VI and the hardware used were configured for use in the lab and tested by measuring the infrared spectra of species in embedded in helium nanodroplets. All spectra recorded in Chapters 6 and 7 were recorded using the automated tuning procedure outlined in this Chapter.

References

[1] A. Henderson, *Photonics Spectra* **2009**, *43*.

[2] A. Henderson, R. Stafford, *Opt. Express* **2006**, *14*, 767–772.

[3] A. Henderson, R. Stafford, J. H. Miller, *Spectrosc. St. Monica* **2005**, *20*, 12–18.

[4] A. M. Morrison, T. Liang, G. E. Douberly, *Rev. Sci. Instrum.* **2013**, *84*, 013102.

[5] S. Hooker, C. Webb, *Laser Physics*, Oxford University Press, New York, USA, **2010**.

[6] A. Henderson, R. Stafford, *Appl. Phys. B Lasers Opt.* **2006**, *85*, 181–184.

Chapter 4: Hydrogen Peroxide in Helium Nanodroplets

4.0 Introduction

Hydrogen peroxide (H_2O_2) is a naturally occurring species that is not only an important oxidant in Earth's atmosphere,[1] but also in the Martian atmosphere.[2,3] It has been used as a photolytic precursor to the formation of highly reactive atmospherically relevant species such as O–H_2O[4] and H_2O_3,[5] which were characterized by infrared (IR) spectroscopy in solid argon. Naturally, those studies were predated by the IR characterization of the H_2O_2 precursor in solid argon, which revealed that the overall rotation of the molecule was quenched, whereas the internal rotation of the two OH bars relative to each other was not.[6] While H_2O_2 has since been studied by IR spectroscopy in Kr and Xe matrices,[7] it has not yet been experimentally investigated in condensed He. Interestingly, theory predicts the axially chiral molecule (in its equilibrium geometry) to behave as a "quantum propeller" in superfluid helium (due to rotation-translation coupling), and the authors speculate that evidence for this could show up as fine structure in the rotationally resolved spectrum.[8]

Helium nanodroplets are unique in that they provide a low density superfluid medium which interacts only very weakly with impurities. They have been used to isolate a variety of otherwise difficult species, such as single protein ions,[9] high-spin alkali clusters,[10] and high energy linear molecular chains.[11] Alternatively, impurity species have been used to probe the droplet environment, which has resulted in evidence that supports particle in a spherical box states,[12] and that they are superfluid.[13] The evidence for superfluidity came from an experiment which gave insight into the density of droplet excitations as a function of energy, revealing a "phonon gap" which is characteristic of bulk superfluid helium.[13,14] This "phonon gap" coincides with the rotational energy of many molecules, allowing for long rotational coherence lifetimes (due to the near absence of droplet states available for the rotationally excited state to couple to). For example, the rotational lifetime of OCS is 30 times greater in ^{4}He droplets in ^{3}He droplets,[15] owing to the much greater density of states at rotational energies in the latter.[16]

While most light molecules such as methane rotate almost freely in superfluid helium nanodroplets,[17] as they do in many solid matrices,[18,19] heavier molecules such as OCS are only known to rotate in helium droplets (in addition to the gas phase),[15] albiet with substantially reduced rotational constants due to the coupling of non-superfluid helium density to the molecular rotation. The relative reduction of the rotational constant(s) of different molecules in going from the gas phase to helium nanodroplets varies greatly (see Fig. 12 in ref. 20),[20] from 2% for HF[21] to 83% for N_2O.[22] The degree of reduction depends mainly on the strength and anisotropy of the helium–molecule interaction potential energy surface, in addition to the rotational speed.[23] A greater interaction strength and anisotropy naturally leads to a greater reduction of the rotational constant(s). For example, while CO_2 and N_2O have similar rotational

constants in the gas phase, the deeper, more anisotropic He–N_2O interaction potential leads to a greater reduction inside of helium nanodroplets (83% for N_2O *vs.* 60% for CO_2).[22,24] If the rotational speed is too fast, however, the surrounding helium density cannot adiabatically follow the rotation of the dopant. Evidence for this comes from the rotational spectra of HCN and DCN in helium nanodroplets, which revealed that the faster rotors' *B* value is reduced by a smaller amount (17%) than that of the slower rotor (19%).[25]

The first rotationally resolved spectrum of gas phase H_2O_2 was reported in 1941, from which the *A* constant (~9 cm^{-1}) was fairly accurately determined to be an order of magnitude greater than the $B \approx C$ constant (~0.8 cm^{-1}) [26] In helium nanodroplets, the threshold for the breakdown of adiabatic following is usually taken as 1 cm^{-1},[27] which falls between the *A* and $B \approx C$ constants. I therefore expect the adiabatic approximation (which assumes adiabatic following) to be valid for rotations about the *b*- and *c*-axes, and almost completely invalid for rotations about the *a*-axis. The structure of hydrogen peroxide and the location of the rotational axes is given in figure 4.1. In the following, I describe the apparatus used to collect the IR spectra, and then analyze and discuss the spectra with reference to previous spectroscopic studies in both the gas phase and cryogenic matrices.

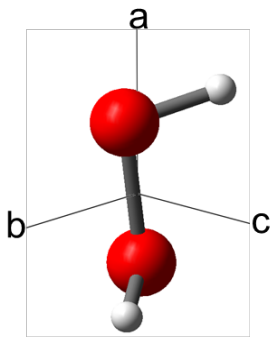

Figure 4.1. The structure of hydrogen peroxide and the-, *b*-, and *c*- rotational axes.

4.1 Experiment

The apparatus used has been described in detail in chapter 2 of this thesis, and elsewhere.[28][29] Briefly, helium nanodroplets are formed in a continuous, supersonic expansion of research grade (99.999%) helium through a pinhole (5 μm) nozzle. The backing pressure (P_{He}) was held constant at 80 bar and the temperature of the coldhead (T_N) was varied from 22 to 36 K, giving mean droplet sizes, $\bar{N}$, ranging from 3600 to 1100 atoms, respectively.[30] These $\bar{N}$ values were estimated from a combination of the experimentally determined values at P_{He}=80 bar, and T_N=16 and 24 K,[30] and the empirically derived scaling laws from ref. 31.[31] All infrared spectra were recorded with $\bar{N}$=2400, while the optically selected mass spectrum was recorded using $\bar{N}$=1700. The skimmed droplet beam crosses a diffuse beam of hydrogen peroxide and its decomposition products (see following) inside of a pick-up cell.

Following Thenard,[32] relatively pure hydrogen peroxide (with vapor pressure, $p \approx 1.61$ mmHg at 20 °C) was obtained by pumping away most of the water from an aqueous solution

(31.4% w/w; $p_{H_2O_2} \approx 0.02$ mm Hg; $p_{H_2O} \approx 12.43$ mm Hg) held in a Pyrex finger.[33,34] The Pyrex finger was coupled to a stainless steel leak valve which was kept fully open for most of the experiments. After passing through the leak valve, the dopant molecules traverse the pick-up cell and encounter a nitrogen trap which was inspired by the set-up in ref. 35.[35] Under these conditions, hydrogen peroxide significantly (>50%) decomposes to water and dioxygen en-route (see the O_2-H_2O line at 3739 cm^{-1} in fig. 1), and it is suspected that the decomposition is mainly catalyzed by the surfaces and/or impurities that are adsorbed on them.

After pick-up, the droplet beam passes through two more vacuum chambers, and is analyzed with a quadrupole mass spectrometer (QMS) in the final chamber. In this chamber, the helium is ionized, and the fragments are deflected into a quadrupole mass filter was operated in one of two modes: In the "normal" mode of operation both DC and RF fields were applied and specific masses were transmitted to the detector, and in the "RF-only" mode the DC bias was removed and masses above 6 u were transmitted.

A fiber laser pumped periodically poled lithium niobate (PPLN) optical parametric oscillator (OPO) system (Lockheed- Martin Aculight) operating in the mid-IR region was used to probe the droplet beam. The OPO beam was aligned coaxially with the droplet beam, and focused using a CaF_2 lens (focal length: 1 m) placed just prior to a BaF_2 input window which is mounted at Brewster's angle at the end of the final chamber. In order to reduce atmospheric H_2O absorptions, the optical path outside the vacuum chambers was purged with dry N_2, as was the OPO cavity. The species embedded in helium droplets that are excited by the OPO beam will mostly relax by heating up the droplet, leading to evaporation of several hundred helium atoms. The decrease in droplet size is detected with the QMS, the signal intensity from which is proportional to the

ionization cross section. The OPO beam was chopped and the signal from the QMS was processed with a lock-in amplifier. The IR power and wavelength were also recorded. Unless otherwise noted, the depletion signal has been divided by the laser power to reduce power dependent features in the spectra.

The cross-section dependent "Poisson curves" reported here were measured under slightly different pick-up conditions than most of the spectra, in that a long quartz tube was used to deliver the dopant species to the droplets. This had the effect of increasing the number of molecules intersecting the droplet beam, but did not have the desired effect of significantly decreasing the degree of decomposition of H_2O_2.

4.2 Results and discussion

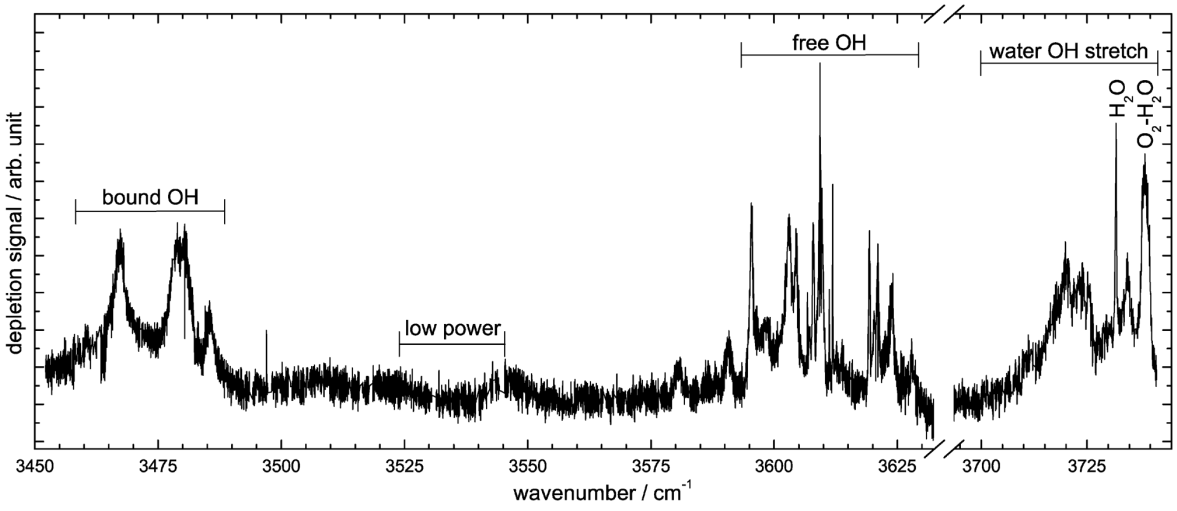

Figure 4.2. Survey spectrum of hydrogen peroxide and decomposition products embedded in superfluid helium nanodroplets. This spectrum has not been power corrected. The indicated H_2O and O_2–H_2O lines were identified from the line positions previously reported. The low power region results from OH absorptions in the PPLN crystal. "Free OH" and "bound OH" indicate regions that contain transitions corresponding to the free OH stretch and the hydrogen bonded OH stretch, respectively, of the H_2O_2 monomer and its clusters with H_2O and/or O_2.

4.2.1 Survey scan

Fig. 4.2 shows a survey spectrum collected with a high dopant flow rate and small droplets size ($\bar{N} \approx$ 2400). The high flow rate was found to be essential in reducing the relative degree of decomposition of H_2O_2 prior to pick-up, and the small droplet size was chosen to counter this high flow rate such that a reasonable number of droplets contained one dopant molecule. Four regions have been identified in Fig. 1, and shall be briefly discussed.

(1) H_2O OH stretch: This region (3700 – 3740 cm^{-1}) contains free and bound OH stretching transitions of H_2O and its dimer with O_2. The peaks in this region are useful for characterizing the impurity molecules (H_2O and O_2) picked-up by the droplets. I did not unambiguously observe the previously reported free OH stretching lines of $(H_2O)_2$ at 3729.5 and 3730.7 cm^{-1},[36] which have a combined infrared intensity that is about 4.6 times that of the O_2–H_2O line indicated in Fig. 4.2.[37] If there was as much H_2O being doped into the droplets as there is O_2, then I would expect to form twice as many O_2–H_2O dimers as $(H_2O)_2$ dimers, resulting in free OH stretching peaks of $(H_2O)_2$ that have 2.3 times the intensity of the O_2–H_2O peak. I did not observe this, however, indicating that there is much more O_2 being doped into the droplets than H_2O. This is probably related to the nitrogen trap more efficiently cryopumping H_2O over O_2. The relative amount of H_2O picked-up by the droplets from the H_2O_2 source was determined by measuring the depletion signal dependence of a known water monomer line (the $1_{01} \leftarrow 0_{00}$ line in the $\nu 3$ band) on the pressure of H_2O in a second doping cell. The signal initially increased upon addition of H_2O to give a maximum value that was ~2 times the initial value, consistent with the absence of the above mentioned $(H_2O)_2$ peaks in the survey spectrum.

(2) Free OH stretch: This region corresponds to the ‘‘non-bonded’’ OH stretch in H_2O_2 and extends from about 3590 to 3630 cm^{-1}. It is the most complicated part of the spectrum with peaks originating from many different species involving H_2O_2 and its complexes with H_2O and/or O_2. This region is the focus of this chapter.

(3) H-bound OH stretch: This region is shifted by about 140 cm^{-1} to the red of the monomer region, and contains three broad features which correspond to the hydrogen bound OH stretch in H_2O_2. Although I have not unambiguously identified the species responsible for these peaks, I suspect that H_2O–H_2O_2 and O_2–H_2O–H_2O_2 complexes are mainly responsible. Support for this is drawn from matrix isolation experiments in solid argon, where the red shift was determined to be 130-140 cm^{-1} for H_2O–H_2O_2.[38]

(4) In addition to the above mentioned regions, I suspect that the bound OH stretching transitions of O_2–H_2O_2 should occur at ~3540 cm^{-1} based on matrix isolation experiments on CO–H_2O_2 (for which the red shift should be similar),[39] and that the bound OH stretching transitions of H_2O in H_2O–H_2O_2 should fall at ~3530 cm^{-1} (once again based on matrix isolation experiments[38]). I did not detect any such peaks, probably owing to the low IR power in this region resulting from OH absorptions in the PPLN crystal. The multimer peaks described above shall not be discussed further in this chapter, since the focus is on the monomer lines. A discussion of the multimer peaks is presented in chapter 5.

4.2.2 Energy Levels and Selection Rules

As with H_2 and H_2O, H_2O_2 contains two identical protons, the spins of which can couple together in an antiparallel or parallel fashion to give *para*-H_2O_2 or *ortho*-H_2O_2, the spectrum with peaks respectively. Interconversion of the *para*- and *ortho*- species is prohibited in the absence of

a catalyst and so the two nuclear spin isomers can be considered as distinct species. Because the separation between rotational levels is much smaller than k_BT at ambient temperatures, the population ratio of the two nuclear spin isomers is primarily dictated by their spin degeneracy ratio, *i.e.* 1 : 3 for *para*-H_2O_2 : *ortho*-H_2O_2. By comparison to nuclear spin isomers of other molecules such as SF_6,[40] I expect this population ratio to be conserved in going from the gas phase (~300 K) to liquid helium nanodroplets (0.3–0.4 K), thus giving rise to intensity alternations between rotational lines in the spectrum. Here I use J_{kk} where J is the total rotational angular momentum quantum number, and K_a and K_c are labels that correlate to the symmetric top quantum number K in the limiting prolate and oblate cases, respectively.

Hydrogen peroxide is the simplest molecule that undergoes hindered internal motion, *i.e.* the torsion (oscillation) or rotation of the two OH groups with respect to each other. The potential which describes this motion has both a *trans* (387 cm^{-1}) and *cis* (2560 cm^{-1}) barrier, and two equivalent minima in-between, corresponding to a skew chain minimum energy structure with a dihedral angle of 112 °.[41] The internal-rotation energy levels are each split into four components due to tunneling through the torsional barriers. As usual, these split levels are labeled with the torsional quantum number τ, and grouped together using the principal internal-rotation quantum number n (see Fig. 4 in ref. 42).[42] Tunneling through the *trans* barrier results in a splitting of 11.437412 cm^{-1} in the ground vibrational state,[43] and 8.1769 cm^{-1} in the first excited antisymmetric stretching state,[44] while tunneling through the *cis* barrier is much weaker and gives an almost negligible splitting, the effects of which have only been observed for $n \geq 1$.[41,45]

Two fundamental OH stretching modes have been observed at high resolution in the gas phase; the antisymmetric stretching mode (ν_5) and the symmetric stretching mode (ν_1).[44,46] While the ν_5

mode has been thoroughly studied, and accurate spectroscopic constants have been determined from the line positions,[44] only tentatively determined subband origins have been reported for the ν_1 mode.[46] This is because the ν_1 mode is perturbed, it is weaker than the ν_5 mode, and several subband origins between ν_1 and ν_5 are nearly coincident, leading to bad overlapping of lines.[46] The near coincidence results from the weak vibrational coupling between the two OH groups,[47] which is much less than that for H_2O ($\nu_3 - \nu_1 = 98.92$ cm^{-1}).[48]

The selection rules for microwave and infrared transitions of H_2O_2 have been derived by Hougen using group theory,[49] and here I briefly introduce the relevant rules. In the absence of tunneling, H_2O_2 belongs to the C_2 point group, and if tunneling is fully considered, as it is here, it belongs to an extended permutation-inversion group of G_4 referred to as G_4^2.[50] Symmetry considerations give rise to the boundary condition that the symmetry species must be a single valued representation of G_4^2,[49] and since H_2O_2 contains two identical protons, the product of the nuclear spin, rotational, torsional, vibrational, and electronic symmetries must be either B_{us} or B_{gs}. From this condition, the lowest energy *para*- and *ortho*- levels are (J, K_a, K_c, n, τ, v) = (1,0,1,0,1,0) and (0,0,0,0,1,0), respectively. Because the parity must change for an electric dipole transition to occur, the general selection rule for the overall symmetry is $B_{us} \leftrightarrow B_{gs}$. Following from this, the selection rules for rotovibrational transitions involving the OH stretch are:

ΔK_a = even; ΔK_c = odd; $\Delta\tau = 0$ (*a*-type)
ΔK_a = odd; ΔK_c = odd; $\Delta\tau = 1\leftrightarrow2, 3\leftrightarrow4$ (*b*-type) } ν_5 mode

ΔK_a = odd; ΔK_c = even; $\Delta\tau = 1\leftrightarrow3, 2\leftrightarrow4$ (*c*-type) } ν_1 mode

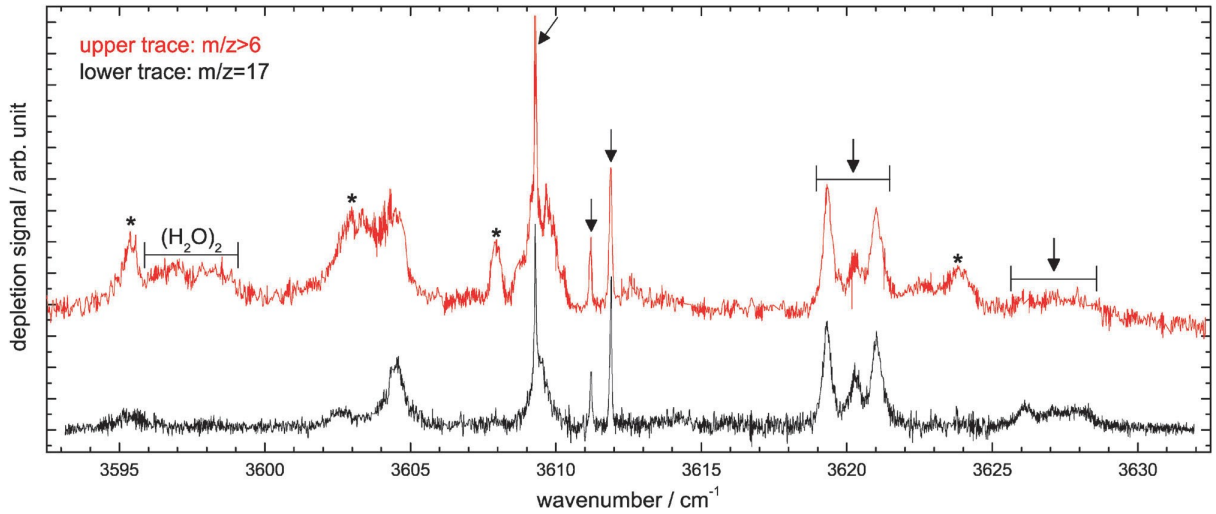

Figure 4.3. Spectra recorded with different mass channels (upper trace m/z ≥ 6; lower trace m/z =17) in the free OH stretching region of H_2O_2. The features that decrease or disappear (marked with *) in going from top to bottom are thought to be related to clusters involving at least H_2O and H_2O_2. The H_2O_2 monomer lines are indicated by arrows. The broad water dimer line at 3597.4 cm^{-1} has previously been identified.[36] The broad feature underlying the $0_{00} \leftarrow 1_{01}$ line is well approximated by a Lorentzian function with centre frequency 3609.432 cm^{-1} and width (FWHM) 0.637 cm^{-1}.

4.2.3 Monomer Spectrum and Discussion

The free OH stretching region of H_2O_2 embedded in helium nanodroplets is shown in Fig. 4.3. It reveals over a dozen peaks, about half of which are most likely due to H-bonded clusters involving H_2O_2, and O_2 and/or H_2O. The cluster peaks were easily identified by measuring the depletion signal as a function of the nozzle temperature while maintaining a constant doping flow rate and helium backing pressure. The average cluster size was determined as outlined in section II, and this was converted to a geometrical cross section and plotted against the depletion signal; Fig. 4.4 shows several representative curves for two suspected monomer peaks and two suspected

cluster peaks. As is expected (from Poissonian statistics),[51–53] the cluster peaks grow in and maximize at larger droplet cross sections relative to the monomer peaks. Following this procedure, I identified three sets of (three) monomer lines (indicated by arrows in Fig. 4.3) which maximize in intensity at smaller droplet cross sections than those for the cluster lines.

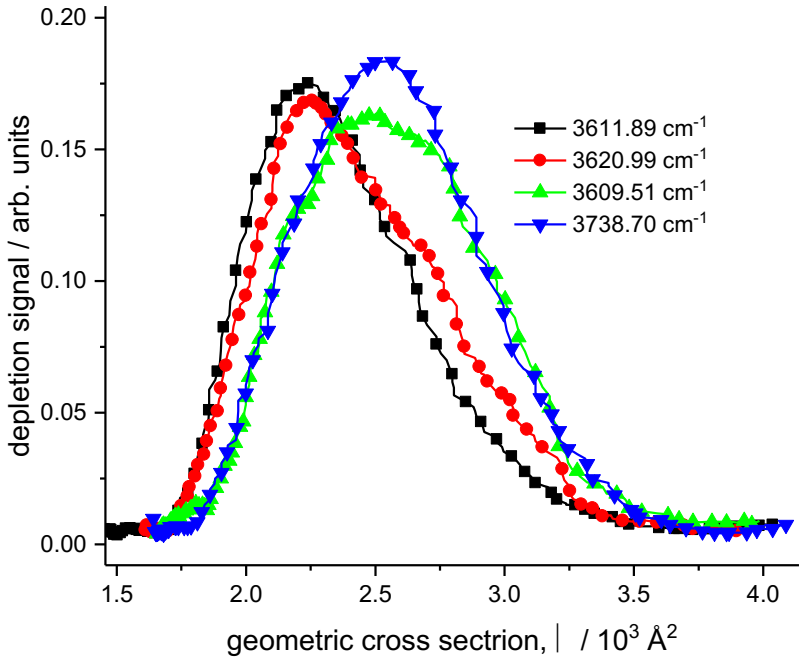

Figure 4.4. Dependence of the depletion signal on the droplet cross section at several different wavenumbers (the data have not been corrected for changes in the characteristics of the droplet beam with T_N; see text). The geometric cross section, σ, was determined from the relation $\sigma = 15.5 \times \bar{N}^{2/3}$.[82] The main curves were measured under different pick-up conditions than for the spectra (see text).

I attempted to fit Poisson curves to the data in Fig. 4.3 without success; correcting for the change in droplet flux with cluster size did not significantly help, and I note that the obtained curves should only be considered qualitative. The departure from Poissonian behavior at low

values of σ may relate to an increasing degree of deflection of the droplets (by H_2O_2, H_2O, O_2) from the beam with decreasing droplet size. The departure at high values of σ may result from an increasing attenuation of the droplet beam with increasing background levels of He gas, the levels of which increased significantly as T_N was lowered. The method of varying the cross section was chosen over varying the flow rate of dopant species, since the latter method notably affected the relative degree of decomposition of H_2O_2 prior to pick-up.

It was possible to almost completely remove some of the cluster peaks in the free OH stretching region by mass selecting *m/z* = 17 (see Fig. 4.3, bottom). A mass-to-charge ratio of 17 was chosen because very few species, except H_2O_2, significantly fragment to this mass. In helium nanodroplets, clusters containing both H_2O and H_2O_2 are not expected to ionize efficiently to *m/z* = 17 simply because H_2O has a tendency to protonate bound species. On the other hand,

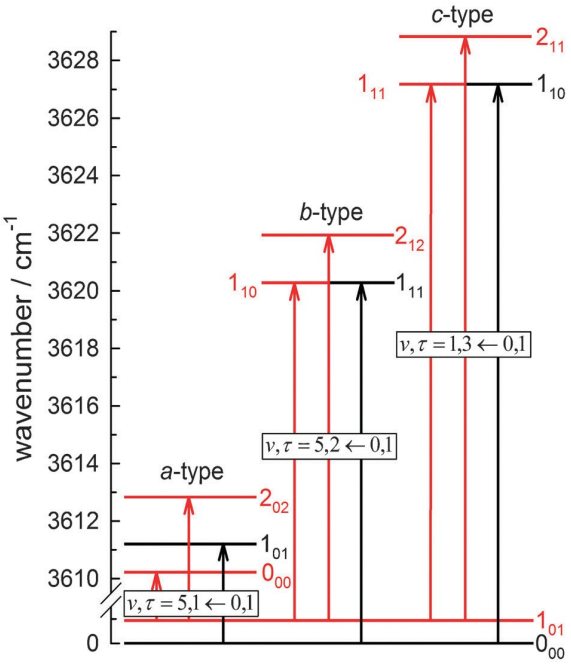

Figure 4.5. Energy level diagram of the observed transitions for H_2O_2 in helium nanodroplets; *ortho* (*para*) levels are red (black).

clusters containing both O_2 and H_2O_2 could very well ionize to OH^+ because the O–O binding energy in dioxygen is relatively large. Indeed, peaks that were suspected to be water related disappeared in the mass selected spectrum, and I expect that most of the remaining intensity in Fig. 4.3 (bottom) originates from either H_2O_2 or O_2–H_2O_2 embedded in helium nanodroplets.

I made the assignment of the monomer lines to specific transitions based on their relative intensities, in addition to their proximity to the corresponding gas phase values.[44,46] Table 4.1 lists the assignments of the measured transitions along with their linewidths and peak areas, and Fig. 4.5 shows the energy levels involved. All lines were found to be within a few wavenumbers of their respective gas phase values. The line positions listed in Table 4.1 were determined from the higher resolution spectra shown in Fig 4.6. The intensity alternations between *para*- and *ortho*-lines support the assignment, although the intensity ratio is more like 1 : 2 rather than 1 : 3. As expected, the *b*-type lines are most intense, followed by the *a*-type lines, then the *c*-type lines. I was able to check that at least the lines within the ν_1 band are not significantly power broadened. This was determined from a saturation study where a linear dependence of the depletion signal on the input power (P_{in}) was observed for P_{in} up to 1.8 W.

Table 4.1. Line characteristics and assignments in the OH stretching fundamentals of H_2O_2 embedded in superfluid helium nanodroplets.

$J'_{K_aK_c} - J''_{K_aK_c}$	Gas Phase (cm^{-1})[a]	He droplet (cm^{-1})[b]	Relative area	Γ (cm^{-1})[c]	Lifetime (ps)
ν_5 band					
$0_{00} - 1_{01}$	3608.95	3609.286(2)	0.31	0.042	>123[d]
$1_{01} - 0_{00}$	3612.37	3611.203(2)	0.16	0.058	>192[d]
$2_{02} - 1_{01}$	3614.08	3611.898(6)	0.38	0.056	>95[d]
$1_{10} - 1_{01}$	3619.69	3619.32(1)	0.88	0.28	19
$1_{11} - 0_{00}$	3621.37	3620.28(2)	0.50	0.38	14
$2_{12} - 1_{01}$	3623.05	3621.00(4)	1.0	0.40	13
ν_1 band					
$1_{11} - 1_{01}$	3626.95	3626.3(1)	0.3	0.8	7
$1_{10} - 0_{00}$	3628.70	3627.1(1)	0.2	0.7	8
$2_{11} - 1_{01}$	3530.44	3627.9(2)	0.4	0.9	6

[a] Determined from the spectroscopic constants found in ref. 44 and 46. [b] Number in parentheses indicates uncertainty in last digit and corresponds to the difference in line positions determined by-the-eye and from a Lorentzian fit. [c] Γ is the Lorentzian linewidth. [d] These values represent a lower limit to the lifetime (see the text).

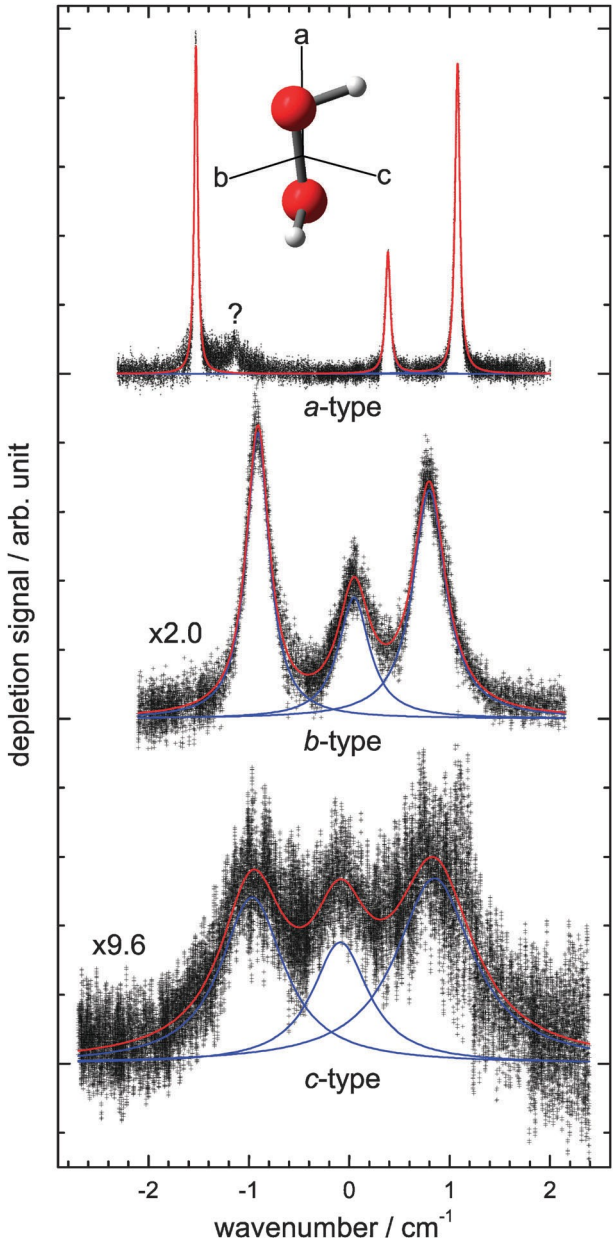

Figure 4.6. The different types of observed transitions centred to zero cm^{-1} for H_2O_2 in helium nanodroplets. The weak feature indicated with "?" remains unidentified. A broad feature underlying the from the $0_{00} \leftarrow 1_{01}$ line has been subtracted from the *a*-type spectrum (see caption of Fig. 4.3).

4.2.4 Optically Selected Mass Spectrum

Optically selected mass spectroscopy is a powerful technique in that one can optically select a mass spectrum of a particular species embedded in helium nanodroplets.[54] It is especially useful if there is a broad distribution of different species (monomers and clusters) embedded in helium nanodroplets, as is the case here. For example, it has recently been used to help assign the spectra of $(HCl)_m(H_2O)_n$ embedded in helium nanodroplets,[55] a task which has previously proven difficult.[56]

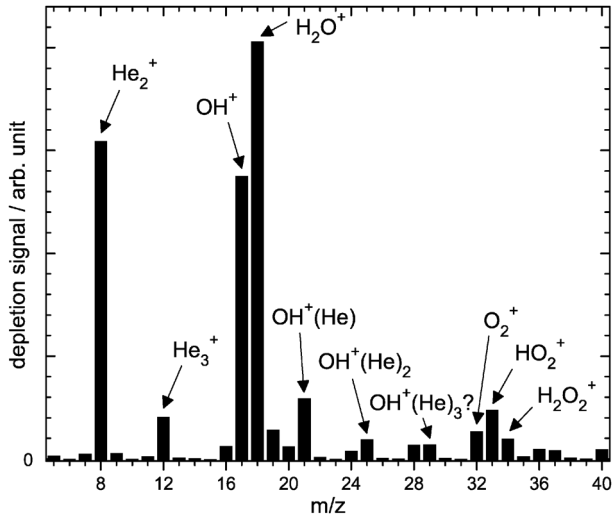

Figure 4.7. Optically selected mass spectrum of H_2O_2 in helium nanodroplets ($\bar{N} \approx 1700$); the laser was parked at 3611.89 cm^{-1} for the duration of the scan.

Fig. 4.7 shows an optically selected mass spectrum of H_2O_2 embedded in helium nanodroplets. The modulated IR beam was parked in the sharp monomer line at 3611.89 cm^{-1}, and the demodulated depletion signal for different ion channels was recorded. The resulting mass spectrum reveals the major fragmentation pathways of the probed species in helium droplets. This spectrum contains all of the fragmentation products that were observed from the gas phase

electron ionization of H_2O_2,[57] supporting in part the above assignment. Interestingly, while the parent ion is the most intense peak in the gas phase,[57] in helium droplets, it is the OH^+ and H_2O^+ peaks that are the most intense. This implies hard over soft ionization of H_2O_2 in relatively small helium nanodroplets ($\bar{N}$ = 1700 He atoms). Small droplets were used to help minimize the probability of impurity pick-up following rotovibrational excitation. Indeed, with larger droplets, the H_2O and O_2 peaks are markedly more intense, and it is clear that some of the signal at 18 and 32 u is due to the subsequent pick-up of these species following excitation. The mass spectrum is similar, regardless of what H_2O_2 momomer line I tuned to, and from control experiments on HDO_2, what ionizing electron voltage was used.

An interesting feature of the optically selected mass spectrum relates to the peaks at 21, 25 and 29 u, which correspond to $OH^+(He)$, $OH^+(He)_2$, and possibly $OH^+(He)_3$. This system has been studied theoretically, where it was predicted that the first few atoms form a solid-like cup at the H end of OH^+.[58] No "magic" cluster sizes are predicted from the variation in the binding energies with cluster size, and so abnormally intense $OH^+(He)_N$ peaks are not expected in the mass spectrum. The incremental binding energy remains fairly constant up to N = 12, then it decreases and once again remains constant out to at least N = 33.[58] The expected deviation in going from N = 12 to 13 relates to the beginning of the filling of the second solvation shell, and should be evident in the mass spectrum if large enough clusters can be unambiguously observed. Unfortunately I was unable to deconvolute larger $OH^+(He)_N$ cluster peaks in the mass spectrum from larger mass fragments (O_2H^+ and $O_2H^+(He)_N$). It should be interesting to examine the optically selected mass spectrum of OH embedded in helium nanodroplets to see if larger snowballs such as $OH^+(He)_{12}$ can be identified.

4.2.5 Rotovibrational Analysis

ν_5 band

H_2O_2 is a near prolate top with a very low degree of asymmetry [asymmetry parameter $\kappa = 0.9922$; $\kappa = (2B - A - C)/(A - C)$],[59] and here I treat it approximately as a (non-rigid) symmetric top ($B = C$, $K = Ka$), and use the following expression for the transition energies (which I note is only valid for $K'' = 0$ and $K' = 0,1$):

$$\Delta E = \nu_5 + B'J'(J'+1) - B''J''(J''+1) - \bar{D}_J\left[\left(J'(J'+1)\right)^2 - \left(J''(J''+1)\right)^2\right]$$

$$+K'\left[A' - B' - D'_{JK} - D'_{JK}\left(J'(J'+1)\right)\right]$$

Here, the "double prime" and "single prime" indicate the vibrational ground and excited state constants, respectively; ν_5 refers to the antisymmetric stretching torsional subband origin with $(n,\tau) = (0,1)\leftarrow(0,1)$, which is assumed to be degenerate with $(n,\tau) = (0,2)\leftarrow(0,1)$. The derived constants are reported in Table 4.2, where they are compared to the gasphase values.

Table 4.2. Fitted constants of H_2O_2 in superfluid helium nanodroplets (in cm^{-1}). The rotational constants were determined from a fit of the ν_5 line positions to expression (1).

Constant	Gas Phase[a]	He Droplet
ν_5[b]	3610.6588	3610.221
B''	0.855775	0.495
$B' - B''$	-3.4 x 10^{-4}	0.023
$\bar{D}_J$	3.0 x 10^{-6}	0.014
$A' - \bar{D}_J$	9.8762	9.583
D'_{JK}	5.7 x 10^{-5}	-0.006
ν_1[b]	3617.95	3617.1[c]

[a] Ground and excited vibrational state rotational constants from ref. 59 and 44, respectively; ν_5 and tentative ν_1 constants from ref. 44 and 46, respectively; B values used correspond to $(B + C)/2$. [b] Subband origins; see the text for details. [c] Determined under the assumption that the ν_5 and ν_1 rotational constants are equal.

The ν_5 subband origin is shifted to the red by 0.438 cm^{-1}, which is fairly typical considering that most band origins are shifted to the red by less than 1 cm^{-1} in going from the gas

phase to helium nanodroplets.[27] Other molecules investigated in the OH stretching region include water[60,61] and formic acid,[62] and for those species the shifts were also less than a wavenumber. The vibrational shift is typically much larger in rare gas (Rg) solids, for which there is often a linear correlation between the shift and the polarizability of the rare gas matrix. Such a correlation is revealed in Fig. 4.8 for H_2O_2, and is similar to that reported for H_2O in different rare gas hosts (see ref. 60 and references therein).[60] The linear dependence of the vibrational shift on the polarizability is usually taken as evidence that dispersion and/or dipole-induced-dipole type interactions dominate the shift.[63] I cannot, however, rule out that repulsive rare gas–H_2O_2 interactions contribute largely to the spread, as was determined to be the case for HCl and CO in different rare gas matrices.[64]

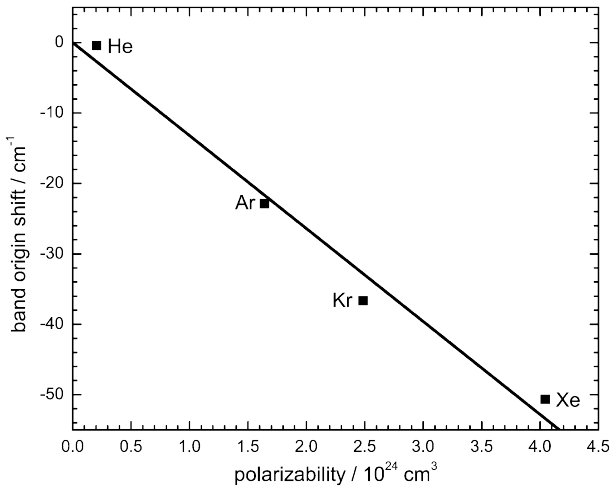

Figure 4.8. The shift of the ν_5 (sub)band origin for H_2O_2 as a function of the polarizability of the rare gas atom[83] which constitutes the matrix. The values for solid argon, krypton and xenon are taken from ref. 7.

The effective $B''(=C'')$ constant is reduced by 42% from its gas phase value, which is very similar to the reduction found for the *C* constant of ethylene (35%).[65] This is not unexpected

considering that the rotational constants are similar in the gas phase (0.83 cm^{-1} for C_2H_4 *vs.* 0.86 cm^{-1} for H_2O_2), and that their interactions with helium are not expected to be drastically different (I reason this based on the Ar–H_2O_2 and Ar–C_2H_4 potentials which are similar).[66,67] This is in stark contrast to (*ortho*-H_2)–HF, which also has a similar rotational constant in the gas phase (0.8325 cm^{-1}),[68] but is reduced by a whopping 78% in going to helium nanodroplets [69] This is most likely due to the strong anisotropy in the interaction between (*ortho*-H2)–HF and surrounding helium atoms.

The effective $\bar{D}_J$ constant is 4600 times its gas phase value, which is typical for most species studied thus far (10^3 – 10^4 times greater).[70] The relationship between *B* and *D* agrees reasonably well with the empirical expression noted in ref. 20 (see Fig. 15), suggesting that a common mechanism is responsible for the relative renormalization of these constants in going from the gas phase to superfluid helium nanodroplets. Lehmann first rationalized the large positive D_J values by considering the coupling between a ring of helium atoms and a central rotor; his "toy" model predicts that the coupling initially increases with *J*, due to an increase in the angular anisotropy in the interaction between the rotor and ring.[71]

As with D'_{JK} (for which the uncertainty is greater than the determined value), I expect D'_K to be several orders of magnitude less than A' in helium droplets. Assuming this to be the case, the A' rotational constant is reduced by only 3% of its gas phase value in liquid helium droplets. This reduction is much less than that for the B' constant, and reflects the idea that the molecule rotates too fast about the *a*-axis for helium density to adiabatically follow. Not surprisingly, this reduction is similar to that reported for NH_3 in several different rotational bands, for which the gas phase rotational constants (which range from 6 to 10 cm^{-1}) were reduced by 3 to 6% in helium,[72] in

good agreement with a later simulation.[73]

As a final point here, I searched for transitions between different values of the principal internal-rotation quantum number ($n = 1 \leftarrow 0$) in this band, but to no avail, most likely because of their low transition strengths and potentially broad linewidths.

ν_1 band

Three *c*-type rotovibrational transitions were detected with relatively low signal-to-noise ratios. I assume that the rotational constants are the same in the observed ν_1 and ν_5 torsional subbands, thus allowing for determination of the symmetric stretching torsional subband origin with $(n,t) = (0,3) \leftarrow (0,1)$ (see Table 4.2). I expect the vibrational shift of the symmetric stretch to be similar to that of the antisymmetric stretch in going from the gas phase to liquid helium. This is largely based on previous studies of H_2O[61] and NH_3 in helium nanodroplets, where the shifts between the two bands were found to be very similar. Additionally, since the splitting between the two modes is much less for H_2O_2 than H_2O[61] or NH_3,[72] the character of the two different vibrations should be similar, resulting in similar shifts. I assume they are the same and take the difference between the observed ν_1 and ν_5 subband origins in helium nanodroplets. I then remove the vibrational dependence by adding the approximate gas phase difference between the ν_1 and ν_5 vibrational frequencies. The deduced value of 7.7 cm^{-1} corresponds to the *trans* tunneling splitting in the excited OH stretching state of H_2O_2, and requires that there is no difference between the torsional frequencies in the ν_1 and ν_5 bands. According to this, the *trans* tunneling splitting is reduced by only 6% relative to the gas phase value (8.2 cm^{-1}), which is similar that determined for the inversion splitting of NH_3 (8%),[12] and less than that for $(HCl)_2$ (28%)[74] or

$(HF)_2$ (40%).[75] I note that the inferred splitting is very approximate, and simply serves to demonstrate that the *trans* tunneling splitting in helium nanodroplets is similar to that in the gas phase.

The infrared intensity of the ν_1 band has not yet been experimentally determined. While I am unable provide an absolute value from the obtained spectra, I can obtain a relative value; the sum of the peak areas in the ν_5 band divided by the sum of the peak areas in the ν_1 band amounts to 3.7 (see Table 1). This agrees well with the previously reported theoretical value of 3.9.[76] To my knowledge, this is the first experimental determination of the intensity ratio of the two OH stretching bands.

4.2.6 Line Profile Analysis

While the line profiles of H_2O_2 embedded in helium nanodroplets are well approximated by Lorentzian functions, it is not necessarily true that the corresponding linewidths are the natural linewidths; Lehmann has shown that the inhomogeneous distribution of droplet sizes may also lead to Lorentzian broadening.[77] The extent of line broadening caused by this effect ought to be similar between the different types of rotovibrational transitions. Since the widths of the *a*-type lines are roughly an order of magnitude less than that of the *b*- or *c*-type lines, I can be confident that the widths of the *a*-type lines represent an upper limit to the degree of broadening associated with the inhomogeneous distribution of droplet sizes. While the lifetimes reported in Table 1 represent lower limits, the values for the *b*- and *c*-type transitions should be closer to the actual values than for the *a*-type transitions. The increase in the linewidth with increasing transition energy is consistent with an increasing availability of helium droplet states to which the excited rotational and torsional states can couple. Indeed, there are relatively few states available below the

energy corresponding to the roton minimum in the dispersion curve of superfluid ^{4}He (~6 cm^{-1}), [14] which lies between the rotational energies of the *a*- and *b*-type lines. Unfortunately, the width of the $J_{K_aK_c} = 1_{10} \leftarrow 1_{01}$ cline is much broader (0.3 cm^{-1}) than its predicted splitting (~0.01 cm^{-1}) due to rotation-translation coupling (which should fully lift the $2J + 1$ degeneracy of the rotational levels).[8] I thus have no evidence for "quantum propeller" behavior of H_2O_2 in superfluid helium nanodroplets. The theoretical basis for the quantum propeller effect developed by Quist and Elser requires that the torsional motion about the oxygen-oxygen bond is inhibited by the helium bath. In effect, the axial chirality must be permanent, rather than transient to enable the observation of the rotation-translation coupling. The torsional motion was largely unaffected by the droplet environment, however, evidenced by the observation of the *trans*-tunneling splitting. It is unlikely that line-splitting due to the quantum propeller effect is an observable phenomenon, even with narrower linewidths.

The *a*-type transition, although relatively narrow, still have widths that are an order of magnitude greater than that observed for some other molecules studied in helium nanodroplets, such as for the $R(0)$ transition of OCS[78,79] which is thought to be largely broadened by rotation-translation coupling.[80] Although it is unclear as to the exact contribution of various processes to the widths of the *a*-type lines reported here, I can infer some details regarding the dynamical interactions from their asymmetries. Fig. 4.9 shows the $2_{02} \leftarrow 1_{01}$ line of H_2O_2, revealing that it is asymmetrically skewed to the red, which is the opposite skewness for the $0_{00} \leftarrow 1_{01}$ line. Similar asymmetries have been observed in the spectra of OCS embedded in helium droplets,[78] and a theory has recently been proposed which quantitatively accounts for the lineshapes of all the rotationally resolved *P* and *R* branch lines for that system.[81] Applying those ideas here, the

asymmetry for H_2O_2 arises from either a chirp up in rotational frequency for the $2_{02} \leftarrow 1_{01}$ (R branch) line or a chirp down for the $0_{00} \leftarrow 1_{01}$ (P branch) line, occurring on a time scale that is one to two orders of magnitude smaller than an initial rotational period.[81] Physically, the idea is that as the rotor speeds up to its terminal frequency, it sheds some helium density due to centrifugal forces (this is because the helium density is farther away from H_2O_2 and so has a higher superfluid fraction).[81]

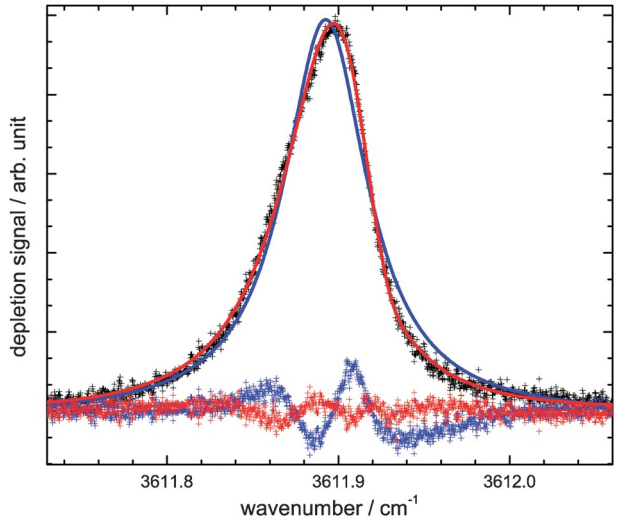

Figure 4.9. Close up of the $2_{02} \leftarrow 1_{01}$ line of H_2O_2 displayed in Fig. 4.5. The blue curve shows a Lorentzian fit to the line, and the red curve shows a skew-fit, with the residuals shown below.

4.3 Conclusions

Infrared spectra of H_2O_2 and complexes involving H_2O_2 and its decomposition products (O_2 and H_2O) have been observed in the 3450–3750 cm^{-1} region. In this chapter, I have assigned and analyzed the antisymmetric and symmetric OH stretching fundamentals of single H_2O_2 molecules in droplets consisting of ~ 2400 helium atoms. The ν_5 and ν_1 torsional subband origins are shifted

to the red by a mere 0.01% and 0.02%, respectively, from their gas phase values. The *trans* tunneling splitting does not appear to be considerably affected by the droplet environment. The infrared intensity of the ν_5 band is 3.7 times that of the ν_1 band, a value which has proven difficult to determine in the gas phase. The $B(\approx C)$ rotational constant is reduced by 42% due to the coupling of non-superfluid helium density to the molecular rotation, and is not surprisingly very similar to that previously reported for the *C* constant of ethylene embedded in helium nanodroplets.[65] The *A* constant is relatively unaffected since rotations about the *a*-axis are too fast for the helium density to adiabatically follow. The $b(\approx c)$-axis centrifugal distortion constant is 4600 times greater in helium droplets, in line with an empirical relation previously noted by Choi *et al.*[20] The *a*-type lines are an order of magnitude narrower than the *b*- or *c*-type lines, consistent with a low density of droplet states available at low rotational energies ($< 3 cm^{-1}$). Finally, the optically selected mass spectrum indicated that hard ionization is favored over soft ionization for H_2O_2 in small helium nanodroplets. Finally, the optically selected mass spectrum indicates that, as evidenced by the more intense fragment peaks over the parent ion peak, which is dominant in the gas phase.

References

[1] A. M. Thompson, *Science* **1992**, *256*, 1157.

[2] R. . Clancy, B. . Sandor, G. . Moriarty-Schieven, *Icarus* **2004**, *168*, 116–121.

[3] T. Encrenaz, B. Bézard, T. . Greathouse, M. . Richter, J. . Lacy, S. . Atreya, A. . Wong, S. Lebonnois, F. Lefèvre, F. Forget, *Icarus* **2004**, *170*, 424–429.

[4] L. Khriachtchev, M. Pettersson, S. Tuominen, M. Räsänen, *J. Chem. Phys.* **1997**, *107*, 7252–7259.

[5] A. Engdahl, B. Nelander, *Science* **2002**, *295*, 482.

[6] J. A. Lannon, F. D. Verderame, R. W. Anderson Jr., *J. Chem. Phys.* **1971**, *54*, 2212–2223.

[7] M. Pettersson, S. Tuominen, M. Räsänen, *J. Phys. Chem. A* **1997**, *101*, 1166–1171.

[8] M. J. Quist, V. Elser, *J. Chem. Phys.* **2002**, *117*, 3878–3885.

[9] F. Bierau, P. Kupser, G. Meijer, G. von Helden, *Phys Rev Lett* **2010**, *105*, 133402.

[10] C. P. Schulz, P. Claas, D. Schumacher, F. Stienkemeier, *Phys Rev Lett* **2004**, *92*, 13401.

[11] K. Nauta, R. E. Miller, *Science* **1999**, *283*, 1895–1897.

[12] R. Lehnig, N. V. Blinov, W. Jäger, *J. Chem. Phys.* **2007**, *127*, DOI http://dx.doi.org/10.1063/1.2822041.

[13] M. Hartmann, F. Mielke, J. P. Toennies, A. F. Vilesov, G. Benedek, *Phys Rev Lett* **1996**, *76*, 4560–4563.

[14] R. A. Crowley, A. D. B. Woods, *Can. J. Phys.* **1971**, *49*, 177.

[15] S. Grebenev, J. P. Toennies, A. F. Vilesov, *Science* **1998**, *279*, 2083–2086.

[16] V. S. Babichenko, Y. Kagan, *Phys Rev Lett* **1999**, *83*, 3458–3461.

[17] K. Nauta, R. . Miller, *Chem. Phys. Lett.* **2001**, *350*, 225–232.

[18] A. Cabana, G. B. Savitsky, D. F. Hornig, *J. Chem. Phys.* **1963**, *39*, 2942–2950.

[19] T. Momose, M. Miki, T. Wakabayashi, T. Shida, M.-C. Chan, S. S. Lee, T. Oka, *J. Chem. Phys.* **1997**, *107*, 7707–7716.

[20] M. Y. Choi, G. E. Douberly, T. M. Falconer, W. K. Lewis, C. M. Lindsay, J. M. Merritt, P. L. Stiles, R. E. Miller, *Int. Rev. Phys. Chem.* **2006**, *25*, 15–75.

[21] K. Nauta, R. E. Miller, *J. Chem. Phys.* **2000**, *113*, 9466–9469.

[22] K. Nauta, R. E. Miller, *J. Chem. Phys.* **2001**, *115*, 10254–10260.

[23] E. Lee, D. Farrelly, K. B. Whaley, *Phys Rev Lett* **1999**, *83*, 3812–3815.

[24] K. Szalewicz, *Int. Rev. Phys. Chem.* **2008**, *27*, 273–316.

[25] A. Conjusteau, C. Callegari, I. Reinhard, K. K. Lehmann, G. Scoles, *J. Chem. Phys.* **2000**, *113*, 4840–4843.

[26] L. R. Zumwalt, P. A. Giguère, *J. Chem. Phys.* **1941**, *9*, 458–462.

[27] C. Callegari, K. K. Lehmann, R. Schmied, G. Scoles, *J. Chem. Phys.* **2001**, *115*, 10090–10110.

[28] R. Lehnig, W. Jäger, *Chem. Phys. Lett.* **2006**, *424*, 146–150.

[29] J. P. Toennies, and A. F. Vilesov, *Annu. Rev. Phys. Chem.* **1998**, *49*, 1–41.

[30] M. Lewerenz, B. Schilling, J. P. Toennies, *Chem. Phys. Lett.* **1993**, *206*, 381–387.

[31] E. L. Knuth, B. Schilling, J. P. Toennies, *Proc. 19th Int. Symp. Rarefied Gas Dyn. Univ. Oxf. 1994* **1995**.

[32] B. Silliman, *Elem. Chem. Order Lect. Yale Coll.* **1830**.

[33] S. L. Manatt, M. R. R. Manatt, *Chem.-Eur. J.* **2004**, *10*, 6540–6557.

[34] S. L. Manatt, M. R. R. Manatt, *Chem-Eur J* **2006**, *12*, 3695.

[35] J. T. Massey, D. R. Bianco, *J. Chem. Phys.* **1954**, *22*, 442–448.

[36] K. Kuyanov-Prozument, M. Y. Choi, A. F. Vilesov, *J. Chem. Phys.* **2010**, *132*, DOI 10.1063/1.3276459.

[37] S. Kuma, M. N. Slipchenko, T. Momose, A. F. Vilesov, *J. Phys. Chem. A* **2010**, *114*, 9022–9027.

[38] A. Engdahl, B. Nelander, *Phys. Chem. Chem. Phys.* **2000**, *2*, 3967–3970.

[39] J. Lundell, S. Jolkkonen, L. Khriachtchev, M. Pettersson, M. Räsänen, *Chem. - Eur. J.* **2001**, *7*, 1670–1678.

[40] J. Harms, M. Hartmann, J. P. Toennies, A. F. Vilesov, B. Sartakov, *J. Mol. Spectrosc.* **1997**, *185*, 204–206.

[41] J.-M. Flaud, C. Camy-Peyret, J. W. C. Johns, B. Carli, *J. Chem. Phys.* **1989**, *91*, 1504–1510.

[42] R. H. Hunt, R. A. Leacock, C. Wilbur Peters, K. T. Hecht, *J. Chem. Phys.* **1965**, *42*, 1931–1946.

[43] P. Helminger, W. C. Bowman, F. C. De Lucia, *J. Mol. Spectrosc.* **1981**, *85*, 120–130.

[44] W. B. Cook, R. H. Hunt, W. N. Shelton, F. A. Flaherty, *J. Mol. Spectrosc.* **1995**, *171*, 91–112.

[45] D. T. Petkie, T. M. Goyette, J. J. Holton, F. C. Delucia, P. Helminger, *J. Mol. Spectrosc.* **1995**, *171*, 145–159.

[46] W. B. Olson, R. H. Hunt, B. W. Young, A. G. Maki, J. W. Brault, *J. Mol. Spectrosc.* **1988**, *127*, 12–34.

[47] R. L. Redington, W. B. Olson, P. C. Cross, *J. Chem. Phys.* **1962**, *36*, 1311–1326.

[48] P. E. Fraley, K. Narahari Rao, *J. Mol. Spectrosc.* **1969**, *29*, 348–364.

[49] J. T. Hougen, *Can. J. Phys.* **1984**, *62*, 1392–1402.

[50] J.-M. Flaud, A. Perrin, *Vib.-Rotational Spectrosc. Mol. Dyn. Adv. Ser. Phys. Chem.* **1997**.

[51] M. Lewerenz, B. Schilling, J. P. Toennies, *J. Chem. Phys.* **1995**, *102*, 8191–8207.

[52] M. Macler, Y. K. Bae, *J Chem Phys* **1997**, *106*, 5785.

[53] M. Lewerenz, B. Schilling, J. P. Toennies, *J Chem Phys* **1997**, *106*.

[54] W. K. Lewis, C. M. Lindsay, R. J. Bemish, R. E. Miller, *J. Am. Chem. Soc.* **2005**, *127*, 7235–7242.

[55] A. M. Morrison, S. D. Flynn, T. Liang, G. E. Douberly, *J. Phys. Chem. A* **2010**, *114*, 8090–8098.

[56] A. Gutberlet, G. Schwaab, Ö. Birer, M. Masia, A. Kaczmarek, H. Forbert, M. Havenith, D. Marx, *Science* **2009**, *324*, 1545–1548.

[57] A. Tessier, W. Forst, *Int. J. Mass Spectrom. Ion Phys.* **1971**, *7*, 281–295.

[58] F. Marinetti, E. Bodo, F. A. Gianturco, *ChemPhysChem* **2007**, *8*, 93–100.

[59] D. T. Petkie, T. M. Goyette, F. C. De Lucia, P. Helminger, S. P. Belov, G. Winnewisserr, *J. Mol. Spectrosc.* **1998**, *192*, 25–31.

[60] C. M. Lindsay, G. E. Douberly, R. E. Miller, *J. Mol. Struct.* **2006**, *786*, 96–104.

[61] K. E. Kuyanov, M. N. Slipchenko, A. F. Vilesov, *Chem. Phys. Lett.* **2006**, *427*, 5–9.

[62] F. Madeja, P. Markwick, M. Havenith, K. Nauta, R. E. Miller, *J. Chem. Phys.* **2002**, *116*, 2870–2878.

[63] F. Huisken, M. Kaloudis, A. A. Vigasin, *Chem. Phys. Lett.* **1997**, *269*, 235–243.

[64] H. Friedmann, S. Kimel, *J. Chem. Phys.* **1965**, *43*, 3925–3939.

[65] C. M. Lindsay, R. E. Miller, *J. Chem. Phys.* **2005**, *122*, 104306.

[66] P. R. P. Barreto, A. F. A. Vilela, A. Lombardi, G. S. Maciel, F. Palazzetti, V. Aquilanti, *J. Phys. Chem. A* **2007**, *111*, 12754–12762.

[67] A. C. Peet, D. C. Clary, J. M. Hutson, *J. Chem. Soc. Faraday Trans. 2 Mol. Chem. Phys.* **1987**, *83*, 1719–1731.

[68] C. M. Lovejoy, D. D. Nelson Jr., D. J. Nesbitt, *J. Chem. Phys.* **1987**, *87*, 5621–5628.

[69] D. T. Moore, R. E. Miller, *J. Chem. Phys.* **2003**, *118*, 9629–9636.

[70] J. P. Toennies, A. F. Vilesov, *Angew. Chem. - Int. Ed.* **2004**, *43*, 2622–2648.

[71] K. K. Lehmann, *J. Chem. Phys.* **2001**, *114*, 4643–4648.

[72] M. N. Slipchenko, A. F. Vilesov, *Chem. Phys. Lett.* **2005**, *412*, 176–183.

[73] A. G. Suárez, J. A. Ramilowski, R. M. Benito, D. Farrelly, *Chem. Phys. Lett.* **2011**, *502*, 14–22.

[74] D. Skvortsov, R. Sliter, M. Y. Choi, A. F. Vilesov, *J. Chem. Phys.* **2008**, *128*, 094308.

[75] K. Nauta, R. E. Miller, *J. Chem. Phys.* **2000**, *113*, 10158–10168.

[76] P. A. Denis, F. R. Ornellas, *J. Phys. Chem. A* **2009**, *113*, 499–506.

[77] K. K. Lehmann, *J. Chem. Phys.* **2007**, *126*, 024108.

[78] S. Grebenev, M. Hartmann, M. Havenith, B. Sartakov, J. P. Toennies, A. F. Vilesov, *J. Chem. Phys.* **2000**, *112*, 4485–4495.

[79] R. Lehnig, P. L. Raston, W. Jäger, *Faraday Discuss.* **2009**, *142*, 297–309.

[80] K. K. Lehmann, *Mol. Phys.* **1999**, *97*, 645–666.

[81] M. N. Van Staveren, V. A. Apkarian, *J. Chem. Phys.* **2010**, *133*, 054506.

Chapter 5: HOOD in Helium Nanodroplets

5.0 Introduction

Peroxides, a class of highly reactive compounds characterized by an oxygen-oxygen single bond, play an important role in biochemistry,[1] planetary science,[2] atmospheric science,[3] and in many other fields. Hydrogen peroxide is the simplest peroxide, containing two OH groups bonded together by a weak oxygen-oxygen bond, and is thus an ideal model with which to study the dynamics and chemistry of the O-O bond. The dynamics and chemistry of H_2O_2 received renewed attention when, in 2011, it was detected in an interstellar cloud.[4] Much of the previous theoretical and spectroscopic studies of hydrogen peroxide has focused on the vibration-rotation-tunneling dynamics.[5–8] The hindered rotation of the two OH groups about the O-O bonds through the *cis*- and *trans*- barriers results in the tunneling-splitting of the rovibrational lines.[9]

The rovibrational spectrum of hydrogen peroxide in helium nanodroplets was detailed in chapter 4. In an analysis of the line splitting, I determined the trans-tunneling splitting to be 7.7 cm^{-1} in helium nanodroplets.[10] This represents a reduction of only 6% of the tunneling splitting

compared to the gas phase. In 2012, Herberth *et al.* measured the far infrared spectrum of singly-deuterated hydrogen peroxide (HOOD).[5] In their study, the torsional splitting in the ground vibrational state due to the *trans*-barrier was determined to be 5.786(13) cm^{-1}. The rovibrational spectrum in the OH stretching region of HOOD in the gas phase has not yet been reported to my knowledge. Further, it has not been reported in helium nanodroplets. HOOD therefore presents a new opportunity to further study the interactions between the superfluid helium matrix and the large amplitude motions about the O-O bond.

In chapter 4, I discussed the concept of a "quantum-propeller" put forth in a theoretical study by Quist and Elser,[11] wherein the rovibrational lines are expected to exhibit fine structure due to rotation-translation coupling of the chiral H_2O_2 rotor in superfluid helium. The fine structure is expected to be observed as splitting of the $J_{K_aK_c} = 1_{10} \leftarrow 1_{01}$ transition into three. Observing the splitting in the rovibrational spectrum requires a resolution of 0.01 cm^{-1}. A resolution of 0.01cm^{1} or higher is well within the resolution limits for helium nanodroplet infrared spectroscopy. For H_2O_2, however, I showed that the linewidth of the $J_{K_aK_c} = 1_{10} \leftarrow 1_{01}$ transition is much broader, at 0.3 cm^{-1} than the required resolution to observe the splitting. Because linewidth of rovibrational lines is correlated to transition energy in helium nanodroplets, it is possible that a shift in transition energy for HOOD as compared to H_2O_2 may cause a reduction in linewidth. Thus, measuring the $J_{K_aK_c} = 1_{10} \leftarrow 1_{01}$ transition in HOOD presents a new possibility for the observation of the theoretically predicted "quantum propeller" effect, should it be observable. To further investigate the possibility of rotation-translation coupling of chiral molecules in superfluid helium, I measured the infrared spectrum of HOOD in helium nanodroplets. The details and results of this experiment are given in this chapter.

5.1 Experiment

Relatively pure H_2O_2 was obtained from a 30% aqueous solution by pumping away most of the water following Thenard.[12] Volumes used were kept below 1 mL, and held in a Pyrex finger encased in a fine metal mesh for safety. One equivalent of D_2O was added to the sample, and the remaining water was again pumped off.[13] Adding D_2O resulted in a 1:2:1 ratio of H_2O_2:HOOD:D_2O_2. The depletion spectrum was measured in the OH-stretching region from 3600 to 3620 cm^{-1} using an Aculight Argos SF-15 laser.[14] Further details of the experimental set up for the measurement of hydrogen peroxide in helium nanodroplets are given in section 4.1 of this thesis.

The details of the helium nanodroplet spectrometer are given in chapter 2 of this thesis. For this experiment, the backing pressure (P_{He}) of ultrapure helium was kept at 80 bar, and the nozzle temperature at (T_N) at 30 K for the production of helium nanodroplets. The resulting droplets had a mean size, $\overline{N}$, of 1700 helium atoms. Based on my findings with H_2O_2, the infrared spectrum of HOOD was measured by mass selecting an m/z of 17, corresponding to the OH^+ ion, to reduce the presence of lines of clusters and other species in the spectrum.[10]

5.2 Results and Discussion

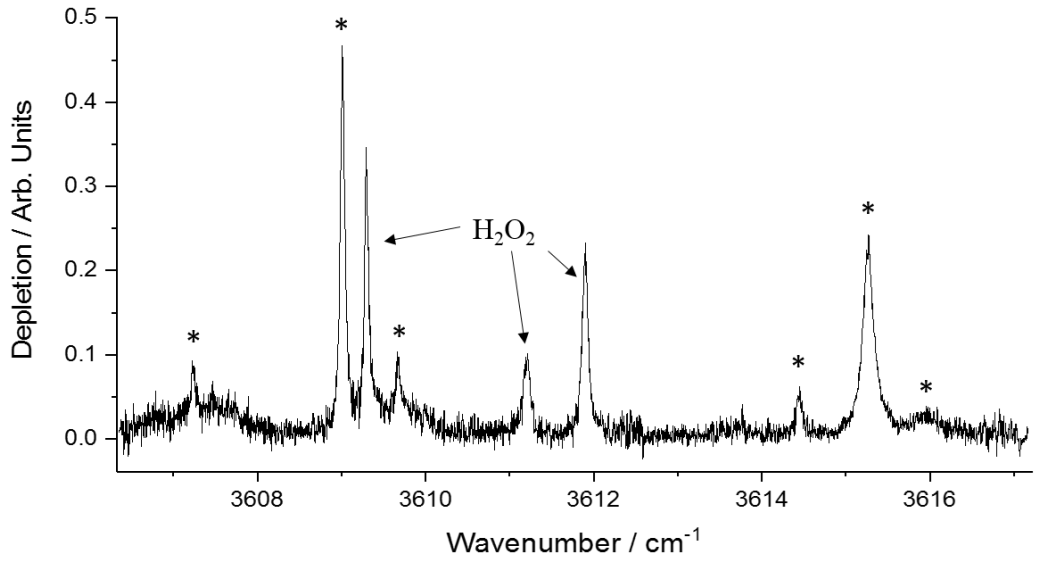

Figure 5.1. Survey scan of HOOD from 3606 to 3617 cm^{-1}. The six new lines in the scan are marked with an asterisk, while the known H_2O_2 lines are labeled separately.

Figure 5.1 shows the relevant portion of the survey spectrum of HOOD which was measured in the region from 3600 to 3620 cm^{-1}. In this region, previously unreported lines attributable to HOOD appear, as well as 3 lines previously assigned to H_2O_2. Because the scan was mass selected for an m/z=17 (OH^+ ion), both H_2O_2 and HOOD lines were expected to be observable in this area. An m/z corresponding to the OH^+ fragment was chosen rather than the OD^+ fragment, as OD^+ corresponds to an m/z of 18, which coincides with the H_2O^+ ion. Because previous work showed many lines in that same region due to water clusters, choosing an m/z of 18 would also enhance water cluster lines, making the spectrum more difficult to interpret. Even with the mass selection, known water dependent cluster peaks are still visible as weak, broad

features underneath the new reported lines at 3607.23 and 3609.00/3609.67 cm^{-1}. These broad features have been observed previously (see chapter 4) and are known to be responsive to changes in water levels within the droplet beam.

Because changes in the flow rate also affected the extent of decomposition and thus the amount of water (either deuterated or non-deuterated) present in the helium droplet beam, quantitative Poisson curves[15] were not possible to determine with this data. I did, however, produce qualitative Poisson-like curves by varying the flow rate and measuring the associated changes in depletion. The resulting data are presented in Fig. 5.2. Three lines (at 3609.0, 3609.7, and 3615.3 cm^{-1}) were examined for the changes in the depletion signal with flow rate, and all show a nearly coincidental response of depletion to the changes in flow rate, suggesting they

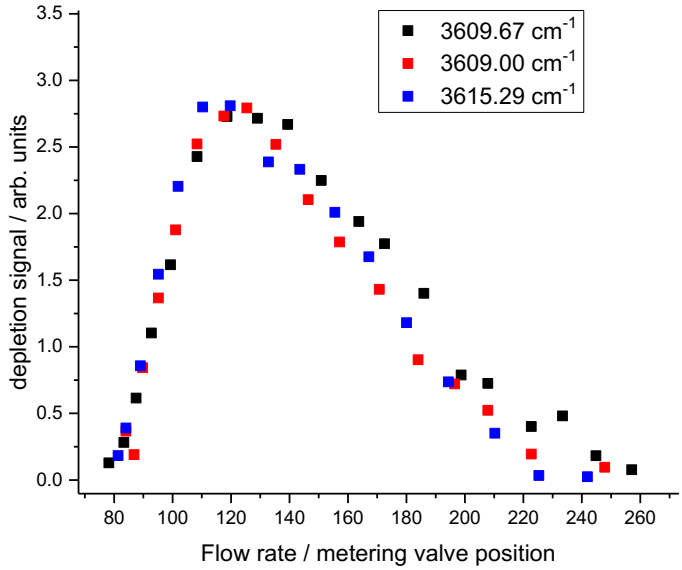

Figure 5.2. The dependence of the depletion signal on the flow rate of the HOOD vapor into the doping cell. Each curve was measured while parking the OPO laser on a specific line identified in the survey scan. The specific laser frequencies used are listed in the legend. The flow rate is the value listed on our Swagelok metering valve. The higher the value, the more open the valve, and the higher flow rate.

correspond to the same species (*i.e.*, the HOOD monomer). Note that the flow rate curves for the remaining three new lines in the spectrum are not included because the data was too variable due to the low intensity of these lines. Each of these three lines did, however, still respond qualitatively to the flow rate as expected.

To further ensure the new lines correspond to HOOD, an optically selected mass spectrum (OSMS)[16] of the line at 3609.0 cm^{-1} was recorded. This line was chosen as representative due to its intensity relative to other lines, since OSMS, like Poisson curves, tend to produce better data when intense lines are used. The OSMS is shown in Fig. 5.3. Since the OSMS for a particular line show the fragmentation pattern of the species responsible for the depletion, comparing the pattern of the suspected HOOD line compared to H_2O_2 (see figure 4.6) illustrates the difference in the fragment ions between the two species. For example, the OSMS for HOOD shows a much greater contribution to the overall depletion at m/z=19, which corresponds to the HDO^+ ion. Previously, I showed that for H_2O_2, the largest ion contributing to the depletion signal for the line at 3611.89 cm^{-1} is the H_2O^+ ion, a product of hard ionization in the small helium droplets used for the spectra. For the suspected HOOD line at 3609.01 cm^{-1}, the m/z=18 is much smaller compared to m/z=19. Excluding the He_2^+ peak, the two largest peaks are for m/z=19 and m/z=17, which corresponds to the OH^+ ion. Further, the peak at m/z=34 is much larger for the HOOD line than for the H_2O_2 line. This is because for H_2O_2, the only contributor to this peak is the parent ion, H_2O_2, whereas for HOOD, this line corresponds to the DO_2^+ ion, which is expected to be much more prominent in the OSMS, similar to HO_2^+ in the H_2O_2 OSMS. A peak for the HOOD parent ion is also present in the OSMS in Fig. 5.3.

Another significant difference between the OSMS for H_2O_2 and HOOD, is the position of

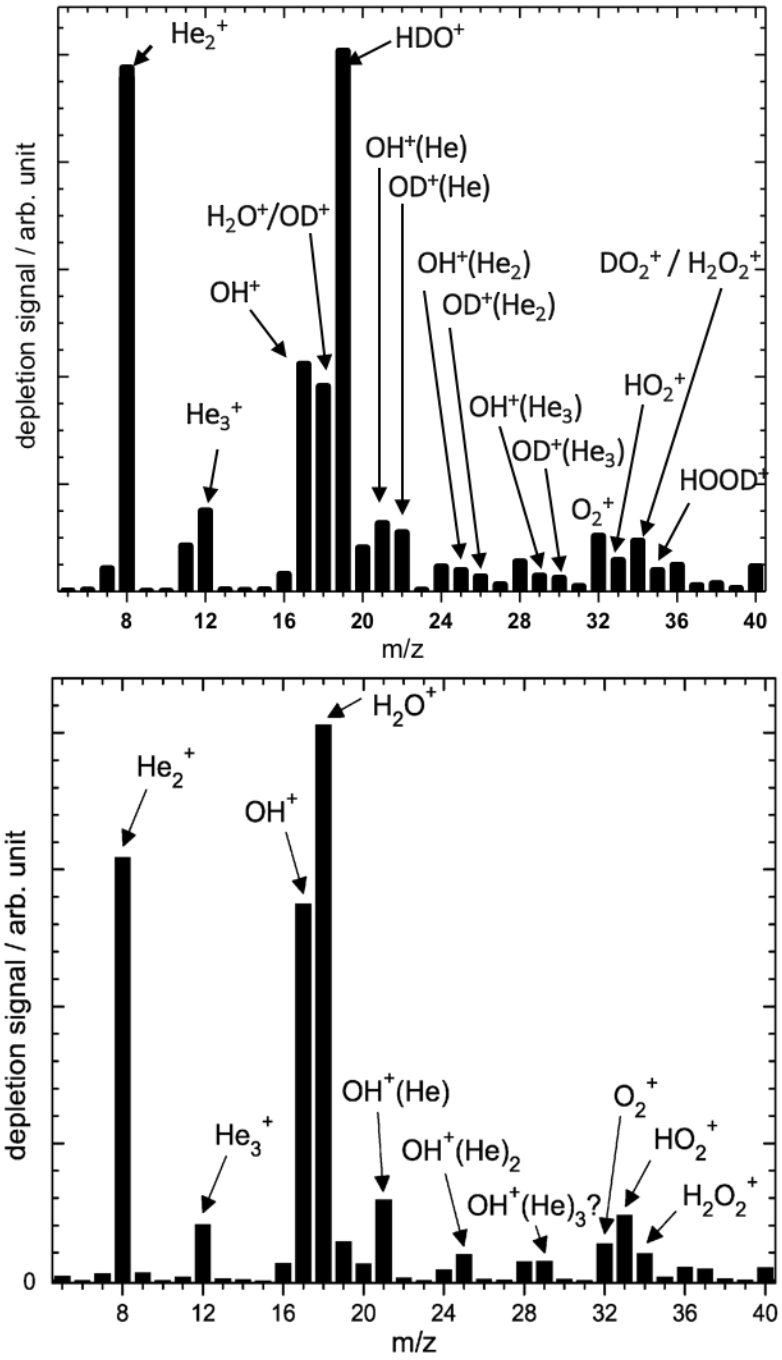

Figure 5.3. a) Optically selected mass spectrum of H_2O_2 in helium nanodroplets ($\bar{N} \approx 1700$); the laser was parked at 3611.89 cm^{-1} for the duration of the scan. b) Optically selected mass spectrum of HOOD in helium nanodroplets ($\bar{N} \approx 1700$); the laser was parked at 3609.01 cm^{-1} for the duration of the scan.

the ion-He cluster peaks. For H_2O_2, an obvious peak for the $OH^+(He)$ ion is present at m/z = 21.

For HOOD, the m/z = 21 peak is also present, but another peak at m/z = 22 also shows up corresponding to the $OD^+(He)$ dimer. This pattern repeats for $OH^+/OD^+(He_2)$ and $OH^+/OD^+(He_3)$, although with reduced intensity. Each of these clusters represent so-called snowball clusters[17] that form when helium is in the presence of positively charged ions. One odd feature, however, is the slightly different intensities of the $OH^+(He_N)$ and $OD^+(He_N)$ peaks. These peaks should present with a 1:1 intensity ratio, but the $OD^+(He_N)$ peaks are slightly less intense than their OH^+ counterparts. The difference could be due to different binding energies of the OD^+ fragment with He atoms, or potentially from contamination due to water being picked up in the droplets downstream following excitation.

The six observed lines were assigned using a combination of experimental and theoretical data. In 2001, Koput *et al.* calculated the band origin for the ν_5 OH stretching mode of HOOD to be 3622.9 cm^{-1}, and reported the calculated rotational energy levels of the ground torsional-vibrational states.[6] By scaling this data by a factor equivalent to what was used with H_2O_2, I calculated the predicted positions of the six observable lines in the ν_5 mode, as well as the band origin. The scaled predicted lines are shown in Table 5.1 (listed as gas phase), next to the positions of the observed lines of HOOD. The scaled calculated line positions match up very well with the observed lines, well within the expected deviation for gas phase vs. helium nanodroplet rovibrational lines.

Table 5.1 – Line positions and assignments in the ν=5 band of HOOD embedded in helium nanodroplets.

$(J'_{Ka'Kc'})$-$(J''_{Ka''Kc''})$	Gas Phase (cm^{-1})[a]	Helium nanodroplets (cm^{-1})	Lorentzian linewidths (cm^{-1})
0_{00}-1_{01}	3606.9	3607.2[b]	-
1_{01}-0_{00}	3610.1	3609.008(2)	0.070(8)
2_{02}-1_{01}	3611.7	3609.68(2)	0.29(8)
1_{10}-1_{01}	3614.8	3614.432(5)	0.05(1)
1_{11}-0_{00}	3616.4	3615.271(1)	0.172(5)
2_{12}-1_{01}	3618.0	3615.95(2)	0.23(6)

[a]Values scaled from calculated values in ref 6.

[b]The low intensity of the line at 3607.2 did not allow for a proper Lorentzian fit.

The recorded lines were fit with PGOPHER software, using Watson's semi-rigid rotor Hamiltonian in its S reduction.[18] Original trial constants for PGOPHER simulations were taken from Herberth *et al.*,[5] and reduced by an appropriate percentage that reflects the renormalization of reported constants.[10] Because only six lines were available, not all relevant spectroscopic constants could be fit to the experimental spectrum. Because HOOD is a nearly prolate symmetric top (k = -0.985) the linear combination $\bar{B}'' = \frac{1}{2}(B'' + C'')$ of rotational constants was fitted. Here, the double prime indicates the ground rovibrational state, while a single prime indicates the excited state. The fitted constants are given in table 5.2, and the overlay of the experimental spectrum with the simulated spectrum using the parameters in table 5.2 is shown in figure 5.4. The band origin of the ν_5 mode was determined to be 3608.06 cm^{-1}, which is within 1 cm^{-1} of the scaled calculated value of 3608.5 cm^{-1}, as is expected.

Using the fitted data, the $(B" + C")/2$ constant is renormalized by 42%, in keeping with the 42% found for H_2O_2.[10] The similarity of these values is likely due first to the similarities of the gas phase rotational constants (0.856 and 0.829 cm^{-1}).[5,19] As noted by Choi *et al.*, the extend of renormalization of rotational constants in going from the gas phase to helium droplets is linked in part to the size of the gas phase rotational constant.[20] Further, the likely similar size of the helium-molecule interaction potential for H_2O_2 / HOOD and the surrounding helium predicts that the renormalization of the rotational constant is again expected to be similar.

Table 5.2: Fitted constants of HOOD in superfluid helium nanodroplets (in cm^{-1}). The rotational constants were determined from a fit of the ν_5 line positions as described in the text.

Constant	Gas Phase	He Droplet
ν_5	3608.5[a]	3608.06
B''	0.829[b]	0.447
B'	0.828[b]	0.500
D_J'	2.62×10^{-6}[b]	0.0154
A'	7.10[c]	6.77

[a] Value scaled from Koput *et al.* in ref. 6.

[b] From ref. 5. In helium droplets, it was assumed that $D_J'' \approx D_J'$. During fitting, D_J'' was held constant and D_J' was fit.

Assuming that $A" \approx A'$ for HOOD in helium nanodroplets, the renormalization of $A"$ compared to gas phase is a mere 4.6%, similar to the 3% renormalization for H_2O_2. This is in keeping with the known trend in the renormalization of rotational constants in helium, where the increase in the effective moment of inertia around a rotational axis is larger for smaller rotational constants. Larger rotational constants result in faster rotors, and the helium cannot follow as effectively, and thus does not add as much to the effective moment of inertia about that particular

rotational axis.[20] Both the anisotropy of the He–molecule potential and the size of the rotational constant dictate the overall extent of the renormalization of the rotational constants, but for faster rotors, the anisotropy of the interaction potential plays a much less significant role.

The final constant fitted from the experimental data is the centrifugal distortion constant

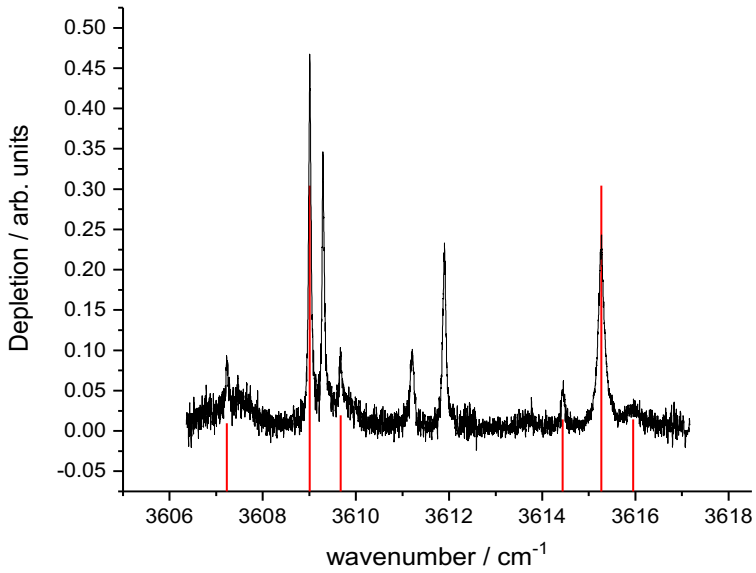

Figure 5.4. The simulated stick spectrum of HOOD at 0.4 K using the constants found in table 5.2. The experimental spectrum is shown above the simulation to illustrate the matchup of the simulated vs. experimental spectrum.

D_J', which was found to be ~5900 times larger than the gas phase ground state value (here, the assumption that $D_J' \approx D_J''$ was made for the comparison). A large increase in D_J is within the expected range of 10^3-10^4 increase in going from the gas phase to helium droplets.[21] Compared to H_2O_2, however, the increase in D_J is larger than expected. For hydrogen peroxide, the effective D_J was only increased by a factor of ~4500. Past studies have shown a correlation between rotational constants and the size of D_J. As B gets larger, D_J in helium droplets is also

expected to increase. However, for HOOD, the rotational constant is smaller, but D_J is larger. The nature of the increase in the effective D_J in going from hydrogen peroxide to the singly deuterated form is unclear, although it should be noted that the effective D_J constant reported here is for the excited vibrational state, rather than the ground state constant used in the comparison. An increase in the number of known rovibrational lines would help with providing enough data to do a more extensive fit, and thus a more direct comparison between helium droplet and gas phase values.

In the study I conducted of H_2O_2 in helium droplets, it was deduced that the *trans*-tunneling splitting is ~7.7 cm^{-1}, assuming that the torsional frequencies of the v_1 and v_5 bands were the same.[10] This indicated that the tunneling splitting is reduced by 6% in going from the gas phase to helium nanodroplets. In the present study, I was not able to determine the *trans*-tunneling splitting for HOOD, because the v_1 band origin (expected to be at ~2660 cm^{-1}) is outside of the range of the laser used when the study was completed. Now that the Jaeger lab has the Aculight ARGOS 2400-SF-15 module C, which has a frequency range of ~2560 – 3100 cm^{-1}, it would be useful to measure the v_1 lines of HOOD to estimate the *trans*-tunneling splitting for HOOD. This will be done in future studies.

Like hydrogen peroxide, I again find no evidence of "quantum propeller" behavior.[11] As detailed previously (see Chapter 4), a 0.01 cm^{-1} linewidth is required for the predicted splitting of the $J_{K_aK_c} = 1_{10} \leftarrow 1_{01}$ line due to the translation-rotational coupling of a chiral rotor with the helium environment. Figure 5.3 shows the $J_{K_aK_c} = 1_{10} \leftarrow 1_{01}$ lines for both H_2O_2 and HOOD, as well as the required linewidth. While the linewidth for HOOD is observed to be smaller than that of hydrogen peroxide, it is still not narrow enough to observe the predicted splitting. Further, the

low intensity of the line means that any potential splitting may also be obscured by noise. A final candidate for observing the translation-rotation coupling would be doubly deuterated hydrogen peroxide, D_2O_2. We were not able to measure the $J_{K_aK_c} = 1_{10} \leftarrow 1_{01}$ line for the doubly deuterated isotopomer, however, since the ν_5 band origin lies at ~2660 cm^{-1}. The measuring of the ν_5 band of D_2O_2 constitutes future work.

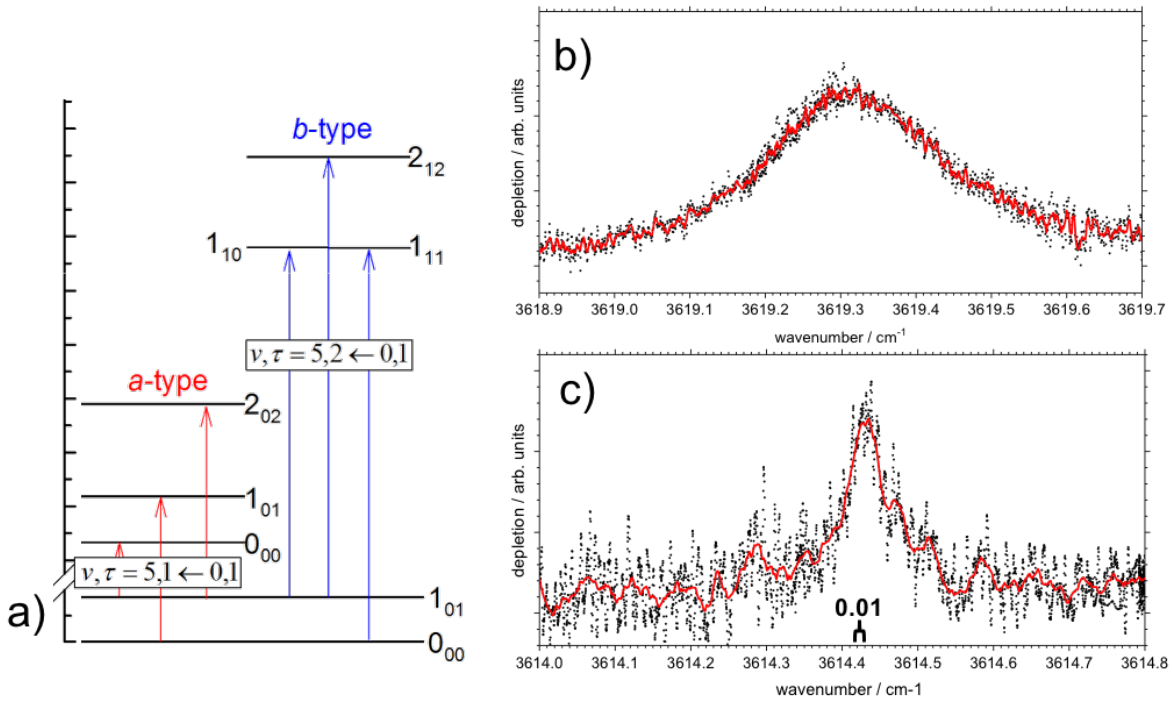

Figure 5.5. a) The energy level diagram for the transitions observed in the spectrum of HOOD. ν, τ represent the vibrational and torsional states, respectively. The values for the rotational quantum numbers $J_{K_aK_c}$ are given to the right of each energy level. The $J_{K_aK_c} = 1_{10} \leftarrow 1_{01}$ lines for H_2O_2 (b) and HOOD (c) are shown to illustrate the smaller linewidth for HOOD for this line. Shown on the HOOD line (c), is the predicted splitting due to the rotation-translation coupling, which could not be resolved. The red lines in figures (b) and (c) are meant only to guide the eye.

5.3 Conclusions

The infrared spectrum of HOOD was recorded in the range of 3600 to 3620 cm^{-1}. Six rovibrational lines were observed in the v_5 OH stretching band, with the v_5 band origin determined to be 3608.06 cm^{-1}. To my knowledge, no experimental gas phase data for the the v_5 band origin exist at this time. However, since the band origin shift in helium nanodroplets is typically less than 1 cm^{-1}, it is expected that the gas phase band origin is very close to the value reported herein. The renormalization of the $(B'' + C'')/2$ and A' constants are in keeping with expected values (42% and 4.6% respectively), and agree well with the renormalization observed for H_2O_2.

There was insufficient data to determine either the *trans*-tunneling splitting or the presence of the quantum propeller effect. To remedy this lack of data, future work will focus on the v_1 band of HOOD, as well as the v_5 stretching band for D_2O_2. The search will require the use of the Argos module C OPO laser, as well as a cleaner source of hydrogen peroxide to improve the signal-to-noise ratio for the recorded spectra. Finally, future efforts will focus on untangling the cluster peaks seen in both the H_2O_2 and HOOD spectra.

References

[1] F. Antunes, P. M. Brito, *Redox Biol.* **2017**, *13*, 1–7.

[2] J. Lasne, A. Noblet, C. Szopa, R. Navarro-González, M. Cabane, O. Poch, F. Stalport, P. François, S. K. Atreya, P. Coll, *Astrobiology* **2016**, *16*, 977–996.

[3] A. M. Thompson, *Science* **1992**, *256*, 1157–1165.

[4] P. Bergman, B. Parise, R. Liseau, B. Larsson, H. Olofsson, K. M. Menten, R. Güsten, *Astron. Astrophys.* **2011**, *531*, L8.

[5] D. Herberth, O. Baum, O. Pirali, P. Roy, S. Thorwirth, K. M. T. Yamada, S. Schlemmer, T. F. Giesen, *J. Quant. Spectrosc. Radiat. Transf.* **2012**, *113*, 1127–1133.

[6] J. Koput, S. Carter, N. C. Handy, *J. Chem. Phys.* **2001**, *115*, 8345–8350.

[7] P. Małyszek, J. Koput, *J. Comput. Chem.* **2013**, *34*, 337–345.

[8] G. S. Maciel, A. C. P. Bitencourt, M. Ragni, V. Aquilanti, *Chem. Phys. Lett.* **2006**, *432*, 383–390.

[9] J.-M. Flaud, A. Perrin, *Vib.-Rotational Spectrosc. Mol. Dyn. Adv. Ser. Phys. Chem.* **1997**.

[10] P. L. Raston, C. J. Knapp, W. Jäger, *Phys. Chem. Chem. Phys.* **2011**, *13*, 18789–18798.

[11] M. J. Quist, V. Elser, *J. Chem. Phys.* **2002**, *117*, 3878–3885.

[12] B. Silliman, *Elem. Chem. Order Lect. Yale Coll.* **1830**.

[13] J.-M. Flaud, J. W. C. Johns, Z. Lu, G. Winnewisser, H. Klein, *Can. J. Phys.* **2001**, *79*, 367–374.

[14] A. Henderson, *Photonics Spectra* **2009**, *43*.

[15] M. Lewerenz, B. Schilling, J. P. Toennies, *J. Chem. Phys.* **1995**, *102*, 8191–8207.

[16] W. K. Lewis, C. M. Lindsay, R. J. Bemish, R. E. Miller, *J. Am. Chem. Soc.* **2005**, *127*, 7235–7242.

[17] F. Marinetti, E. Bodo, F. A. Gianturco, *ChemPhysChem* **2007**, *8*, 93–100.

[18] C. M. Western, *J. Quant. Spectrosc. Radiat. Transf.* **2017**, *186*, 221–242.

[19] D. T. Petkie, T. M. Goyette, F. C. De Lucia, P. Helminger, S. P. Belov, G. Winnewisserr, *J. Mol. Spectrosc.* **1998**, *192*, 25–31.

[20] M. Y. Choi, G. E. Douberly, T. M. Falconer, W. K. Lewis, C. M. Lindsay, J. M. Merritt, P. L. Stiles, R. E. Miller, *Int. Rev. Phys. Chem.* **2006**, *25*, 15–75.

[21] J. P. Toennies, A. F. Vilesov, *Angew. Chem. - Int. Ed.* **2004**, *43*, 2622–2648.

Chapter 6: The Hydrogen Peroxide Dimer in Helium Nanodroplets

6.0 Introduction

Hydrogen peroxide is a small molecule containing two OH groups rotated 113.6° relative to one another along the O-O bond to give an open book structure.[1] The two OH groups allow hydrogen peroxide to participate in multiple hydrogen bonds when interacting with other molecules to form clusters. Hydrogen bonded clusters containing hydrogen peroxide represent a system of interest due to the presence of hydrogen peroxide, and its role as an oxidant, in the atmosphere.[2] Additionally, the hydrogen peroxide dimer itself, $(H_2O_2)_2$, is an important system for understanding cooperative hydrogen bonding,[3] and may be an important source of oxygen in the icy surfaces of Galilean satellites such as Ganymede and Europa.[4]

Much previous work has been done on hydrogen peroxide dimers, as well as hydrogen peroxide complexes with water. In 2000, Engdahl and Nelander reported the infrared spectrum of the H_2O_2-H_2O complex in an argon matrix.[5] The first matrix isolation study of hydrogen peroxide dimers was conducted by Engdahl *et al.*,[3] who measured the infrared spectrum of the dimer in the OH stretching region, and showed that the dimer is cyclic in structure. Each

hydrogen peroxide unit acts as both a hydrogen bond donor and acceptor, which is evident in the infrared spectrum which contains a hydrogen-bonded OH stretch (ν_1), and a free OH stretch (ν_5). Unlike the water dimer, $(H_2O)_2$, the H_2O_2-H_2O and $(H_2O_2)_2$ dimers both form cyclic structures with each monomer acting as both a hydrogen bond donor and acceptor, and thus represent excellent structures for investigating the effects of cooperative hydrogen bonds.[3,5] The infrared spectra of many other hydrogen peroxide complexes have also been investigated in argon matrices, including H_2O_2-OCS and H_2O_2-CS_2[6], H_2O_2-SO_2[7], and H_2O_2-HOO.[8]

In addition to the matrix isolation studies, a body of theoretical work pertaining to larger hydrogen peroxide clusters $(H_2O_2)_n$, has emerged to understand the extensive hydrogen bonding interactions in larger structures, as well as the implications of the (transient) chirality of hydrogen peroxide on the shape of large clusters. In 2003, Kulkarni *et al.*,[9] performed *ab initio* calculations for $(H_2O_2)_n$, with n=2-4, which indicate that clusters of hydrogen peroxide form three-dimensional structures analogous to water clusters. Subsequent studies indicate that larger clusters have the potential to form helices due to the open-book structure of hydrogen peroxide.[10]

Helium nanodroplets represent an ideal matrix for the investigation of possible structures of hydrogen peroxide clusters. Such investigations have been achieved before using water clusters, where the cyclic water hexamer was trapped and investigated using infrared spectroscopy.[11,12] As a basis for future work on larger clusters, I have investigated the hydrogen peroxide dimer in helium nanodroplets. While I was able to unambiguously assign the hydrogen peroxide monomer lines in Chapter 4, I was unable to assign the cluster peaks due to the large amount of water and oxygen in the droplets from decomposition of the hydrogen peroxide prior

to doping, as well as the residual water that remained after concentrating the aqueous sample. In order to assign the cluster peaks, I switched the hydrogen peroxide source to a solid urea-hydrogen peroxide complex (UHP). UHP has been shown to be a clean, easy to use hydrogen peroxide source for matrix isolation studies.[5,13] In this chapter, I detail my assignment of the hydrogen peroxide dimer OH stretching bands in helium nanodroplets using UHP as a doping source.

6.1 Experiment

As detailed in Chapter 2 of this thesis, a helium nanodroplet beam was produced by expanding high purity helium through a 5 μm pinhole nozzle. The nozzle temperature (T_N) was held at 20 K, and the helium backing pressure (P_{He}) at 40 bar, resulting in a mean droplet size of ~3500 atoms.[14] The droplet beam is skimmed and passes into a doping chamber where hydrogen peroxide is picked up by the droplets. A solid urea-hydrogen peroxide complex (UHP) was used as source of hydrogen peroxide.

Solid UHP (Sigma Aldrich, 97% purity) was placed in a glass finger and attached directly to a doping cell inlet with a single on-off valve (Swagelok) between the source and the doping chamber. Preliminary experiments using the UHP source showed a dramatic decrease in decomposition with a shorter path-length prior to the doping cell. The glass finger was wrapped in heating tape and the temperature was held constant at ~30°C to achieve a doping pressure of ~7.7×10^{-7} Torr for the survey scan (figure 6.1) and ~28°C to achieve a doping pressure of ~5.0×10^{-7} Torr. Under these conditions, hydrogen peroxide showed minimal decomposition as determined by mass spectra of the doped droplets. For the pressure dependence studies, the

temperature was varied to achieve desired doping pressures. A second doping chamber was used for the addition of water through a leak valve for the investigation of water containing clusters.

A mid-infrared laser (Lockheed-Martin Aculight ARGOS 2400-SF-15, module B) was aligned coaxially with the droplet beam for the purposes of measuring infrared spectra of dopants within the droplets. The frequency of the laser was varied using the automated tuning system detailed in chapter 3. When the laser frequency is resonant with a vibrational mode of the droplets, a photon is absorbed, followed by relaxation in which the energy of the photon is transferred to the helium bath resulting in evaporation of helium atoms. The net effect is to reduce the cross-section of the droplets, which is monitored with a quadrupole mass spectrometer. The reduction in droplet size results in a reduction of the ionization cross-section of the droplets, and thus a reduced ion signal.

6.2 The Hydrogen Peroxide Dimer Structure

Structure calations were performed using the GAUSSIAN 09 program[15] using the MP2 method and 6-311++g(2d,p) basis set. The two lowest energy structures were identified as cyclic structures, in agreement with previous theoretical studied.[9,10] The lowest energy cyclic dimer has the two “free” hydrogen atoms (ie., those not directly involved in a hydrogen bond) pointing away from the ring, but on opposite sides. One of the free hydrogen atoms can be thought of as pointing up, and the other down. The up-down structure is referred to as UD. The second ring structure was determined to be just 1.22 kJ/mol higher in energy, and has both of the free hydrogen atoms pointing away from the ring on the same side (referred to as up-up, or UU). The UU and UD structures are shown in Figure 6.1.

Vibrational calculation on the optimized structures showed that the most intense OH stretching frequency was the asymmetric stretch of the bound OH, which were calculated to be 3655 and 3648 cm^{-1} for the UU and UD dimers, respectively (these are unscaled values). The bound OH stretch is also redshifted with respect to the free OH stretching frequencies by 130-150 cm^{-1}. For the UU dimer, the symmetric and asymmetric free OH stretch showed similar intensities at 3784.3 and 3784.6 cm^{-1}, a difference that is large enough to resolve in helium nanodroplets, assuming a line width of <0.5 cm^{-1}. For the UD dimer, only the asymmetric stretch of the free OH can be observed due to a change in dipole moment which does not occur with the symmetric stretch. The free OH stretch for the UD dimer was calculated to be 3799 cm^{-1}. Given

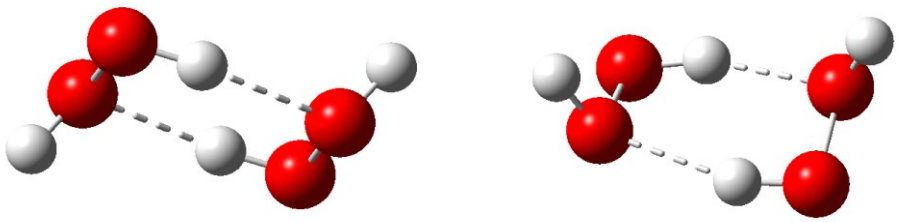

Figure 6.1. Optimized geometries of the up-down (left) and up-up (right) cyclic hydrogen peroxide dimers. The bound OH contains the hydrogen atom participating in hydrogen bonding (shown by the dashed line). The free OH groups are those with the hydrogen not participating in hydrogen bonding, pointing outside of the dimer ring. In the up-down structure, the free hydrogens are pointing away from the ring, with one pointing up, and the other down. In the up-up structure, the two free hydrogens are both pointing away from the ring on the same side.

the calculated frequencies, the infra-red spectra of both conformers should be observable in helium nanodroplets. In the matrix isolation study performed by Engdahl *et al.*,[3] the structure of the hydrogen peroxide dimer was determined to be cyclic rather than open, but the authors did not comment on the UU vs. UD conformation of the dimer. The structure in that case was assumed to be the lowest energy (UD) conformer.

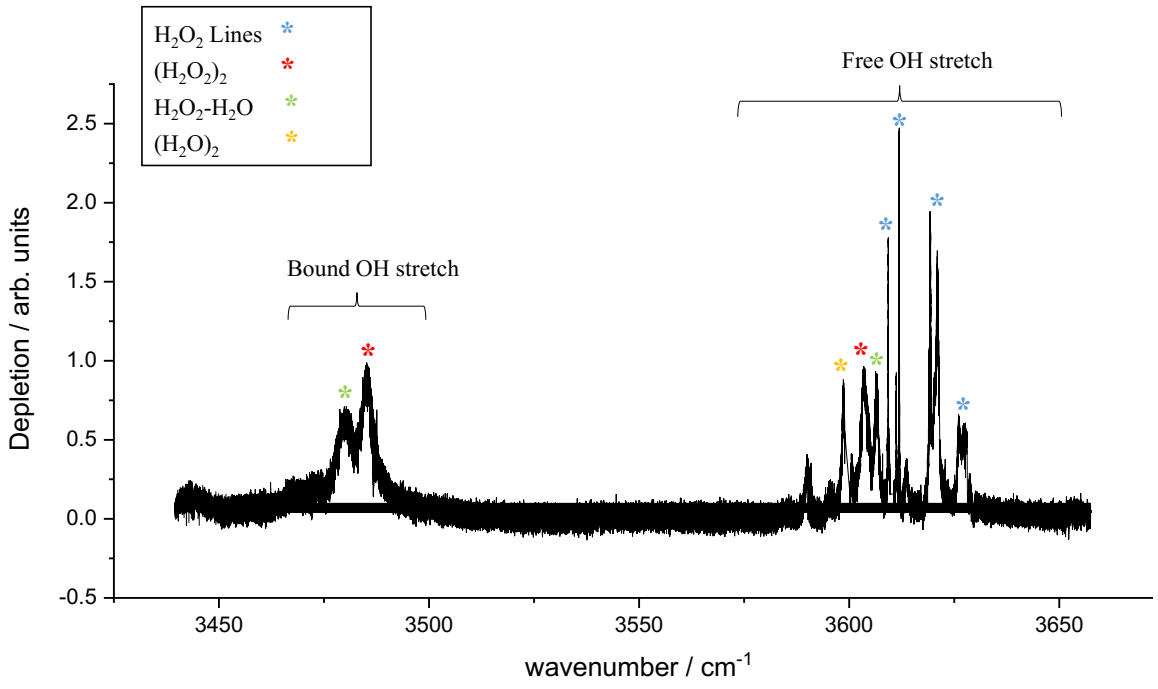

Figure 6.2. Survey scan of the OH stretching region of hydrogen peroxide in helium droplets using a solid urea-hydrogen peroxide complex as the source. The spectrum contains lines from the hydrogen peroxide monomer as well as complexes including the hydrogen peroxide dimer $(H_2O_2)_2$, the hydrogen peroxide water dimer H_2O_2-H_2O, and the water dimer $(H_2O)_2$. The spectrum is divided into the bound OH stretching region below 3500 cm^{-1}, and the free OH stretching region above 3575 cm^{-1}. The spectrum was recorded at a high doping pressure to enhance the cluster peaks.

6.3 Results and Discussion

6.3.1 Survey Scan and Line Assignments

A survey spectrum of hydrogen peroxide using the urea-hydrogen peroxide source is given in Figure 6.2. The survey spectrum contains the expected features for the hydrogen peroxide monomer, but shows some differences from the survey spectrum collected with the concentrated liquid hydrogen peroxide source (see Chapter 4, Figure 4.1). Most notably, the spectrum appears

cleaner, with fewer of the suspected (previously unassigned) cluster peaks. Further, the intensity of the known water dimer peak at 3598 cm^{-1} is reduced relative to the hydrogen peroxide monomer peaks. The reduction in the relative intensity of the water dimer peaks indicates that the solid hydrogen peroxide source is considerably cleaner. In fact, the comparison of the survey spectra from the two different hydrogen peroxide sources provided a good indication of which

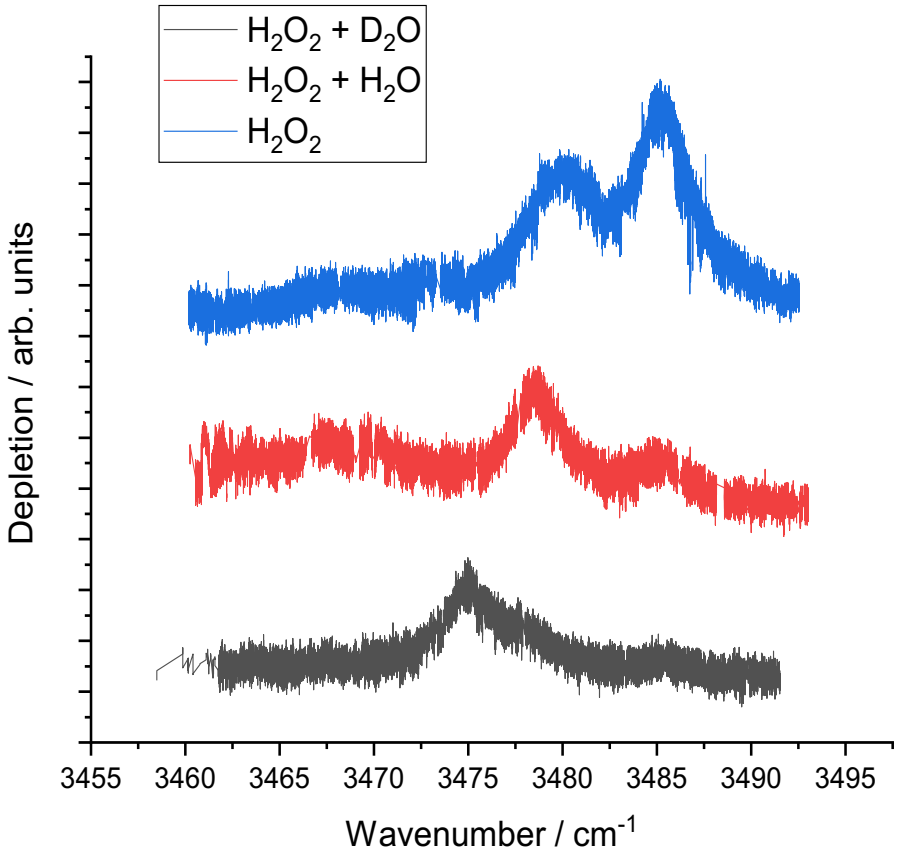

Figure 6.3. Spectra of the bound OH stretch of hydrogen peroxide. The blue trace was taken under standard doping conditions using the urea-hydrogen peroxide complex at a doping pressure of $5.0x10^{-7}$ Torr. Each of the bottom two traces were taken with a reduced doping pressure of hydrogen peroxide at $4.0x10^{-7}$ Torr while also doping with H_2O (red) and D_2O (black) in a separate doping cell, for a combined doping pressure of $4.4x10^{-7}$ Torr.

cluster peaks contained water, and was a starting point for the assignment of the hydrogen peroxide dimer lines. The survey spectrum contains several marked lines with tentative assignments, as well as known hydrogen peroxide lines (detailed in Chapter 4).

To help eliminate possible hydrogen peroxide-water cluster lines, each line in the survey spectrum (with the exception of the hydrogen peroxide monomer lines) was tested by intentionally adding water to the droplets through a precision leak valve, and monitoring the dependence of the depletion signal on the addition of water. Lines showing an increase in the depletion signal with the addition of water were classified as likely hydrogen peroxide-water multimer lines. The results of the initial water tests left 3 lines as potential candidates for $(H_2O_2)_2$: 3485, 3603.5, and 3606.5 cm^{-1}. Each of these lines, as well as some of the suspected water lines were subjected to further investigations to achieve line assignments. Figure 6.3 shows spectra obtained by intentionally adding water to look at the intensity changes of two overlapping lines in the bound OH stretching region for hydrogen peroxide. D_2O was also added in a third scan to show the shift in the OH stretch frequency for H_2O_2-D_2O compared to H_2O_2-H_2O.

Pressure dependence studies examining the dependence of depletion on the doping pressure of hydrogen peroxide were performed on several lines, including monomer lines for comparison. This was done by parking the laser on the frequency of a particular line, and then measuring the total depletion at different doping cell pressures. In Figure 6.4, the line at 3606.5 cm^{-1} shows the same doping pressure dependence as each of the included monomer lines (3611.89, 3519.3, and 3621.0 cm^{-1}) indicating that it is likely a cluster peak containing only one hydrogen peroxide. The remaining lines at 3485.0 and 3603.5 cm^{-1} show a different relationship

to the depletion on the partial pressure of hydrogen peroxide, indicating potential $(H_2O_2)_n$ clusters.

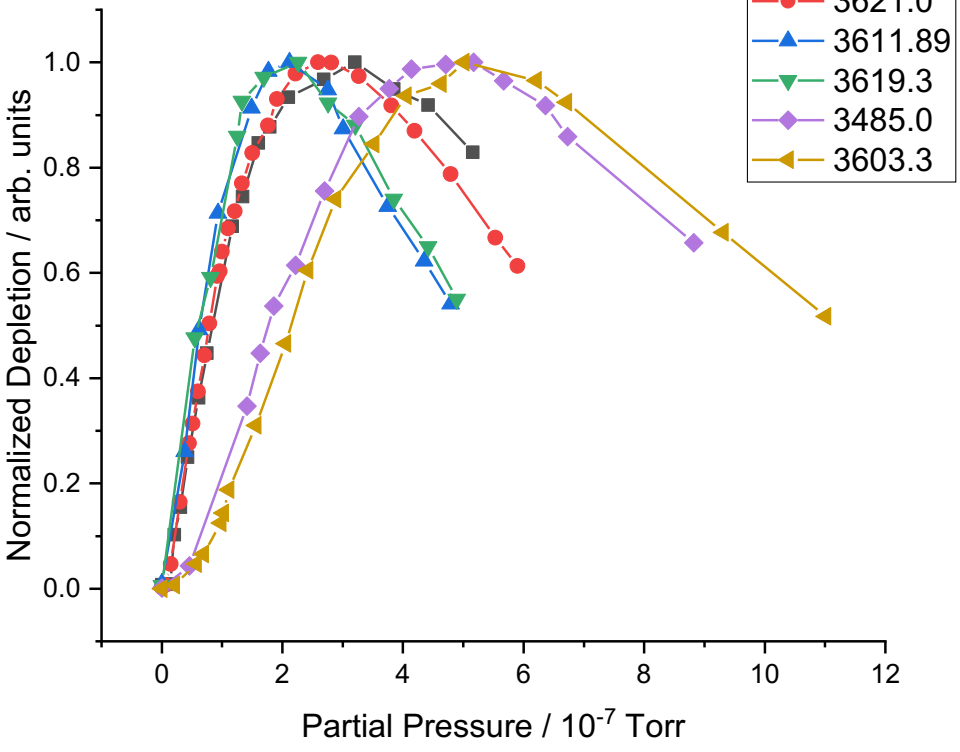

Figure 6.4. The pressure dependence of several hydrogen peroxide containing lines, measured by varying the doping cell pressure and measuring the depletion at the given frequencies.

To determine the number of hydrogen peroxide molecules included in the cluster, Poisson curves were fit to the data. The relationship between the probability for pickup of n dopant molecules (P_n) and the doping pressure is given by the following relationship:

$$P_n(\rho) = \frac{(\sigma l \rho)^n}{n!} \exp(-\sigma l \rho). \qquad (1)$$

where σ is the cross-section of the droplet, l is the length of the doping cell, and ρ is the number

density of the gas in the doping cell.[16] Because the cross-section and path length are held constant, the depletion signal as a function of partial pressure of hydrogen peroxide in the doping cell can be fit to equation (1) to give the number of particles, n. Figure 6.4 gives the Poisson fit

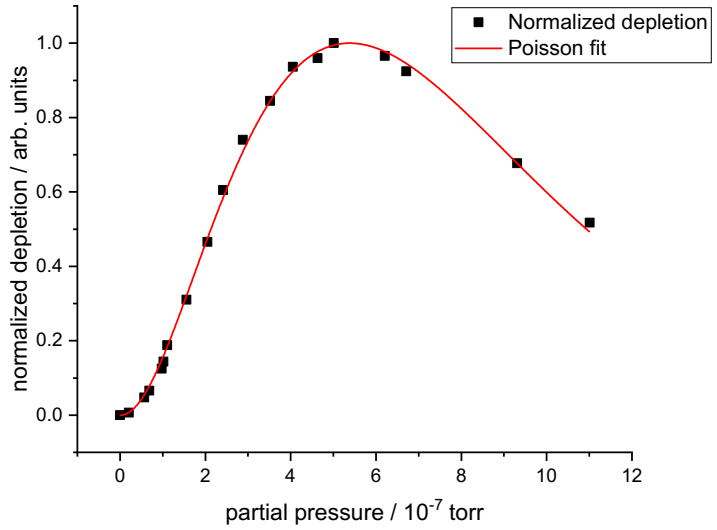

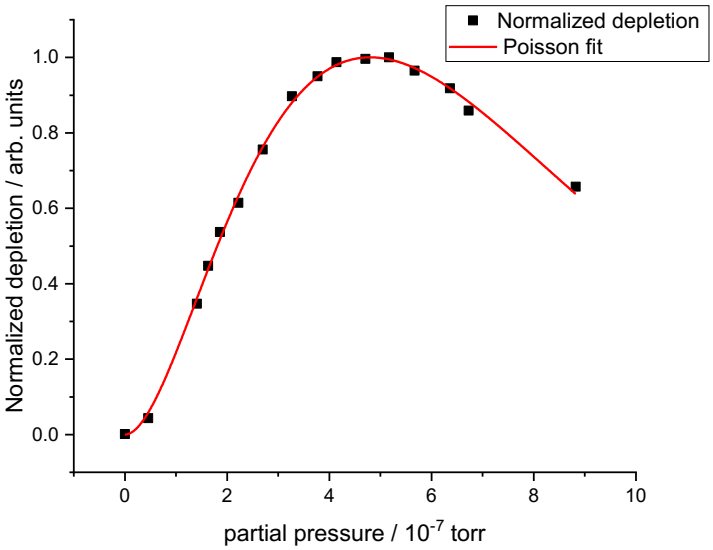

Figure 6.5. Poisson fits for the two $(H_2O_2)_2$ lines at 3603.5 cm^{-1} (top) and 3485.0 cm^{-1} (bottom). The line at 3603.5 cm^{-1} was fit to n=2.14(4) with an R-squared of 0.99829. For the line at 3485.0, the fit gave n=1.96(4) with an R-squared of 0.99842.

for the suspected dimer lines, both of which fit to n=2. Because of the Poisson curve fits and the negative test for the presence of water, it is reasonable to conclude that these lines correspond to the bound and free OH stretches of the hydrogen peroxide dimer.

The assignment of the free and bound OH stretch of $(H_2O_2)_2$ is in good agreement with a matrix isolation study conducted by Engdahl *et al.*[3] Table 6.1 lists the line positions of the helium dimer in hydrogen peroxide, as well as in an argon matrix. Like the matrix isolation study, the line positions in helium nanodroplets indicate a cyclic dimer, although it is not clear whether the dimer is of the UU or UD conformation. For the UU conformer, the free OH stretching region was expected to contain both the asymmetric and symmetric stretches, but the linewidth of the free OH stretch is too large to observe the lines separately. It could be possible to observe both the UU and UD dimers as the free OH stretches are separated by ~5 cm^{-1} according to the calculations. However, no other candidate $(H_2O_2)_2$ lines were observed in the free OH region. To assign the spectrum to a specific structure—either UU or UD—the spectra of deuterated dimers need to be measured, which will be done as future work.

Table 6.1. Line characteristics and assignments in the OH stretching spectrum of $(H_2O_2)_2$ embedded in superfluid helium nanodroplets.

Assignment	Helium droplet (cm^{-1})	Ar-Matrix (cm^{-1})[a]	Lorentzian linewidth (cm^{-1}) in He	Calculated frequencies[b] Up-Up	Calculated frequencies[b] Up-Down
Bound OH stretch	3485.24(2)	3471.3	4.021(8)	3655	3649
Free OH stretch	3603.60(1)	3581.7, 3576.7	1.830(5)	3784	3780

[a]From ref.3.

[b]Calculated values are unscaled. See text for calculation details.

In the matrix isolation study performed by Engdahl *et al.*,[3] two separate lines were observed in the free OH stretching region. This is in contrast to the single OH stretch observed in helium nanodroplets. The authors, however, attribute the two lines to a site splitting due to a possible asymmetry of the trapping site. Unlike frozen rare gas matrices, helium droplets not exhibit site splitting effects because the superfluid medium allows for nearly free movement of dopants inside the droplet.[17] Gas-phase infrared spectra of the hydrogen peroxide dimer have, to my knowledge, not yet been reported. However, the infrared spectrum of the hydrogen peroxide dimer in helium nanodroplets is expected to be more similar than those recorded in argon matrices to the spectrum in the gas phase. The dimer spectrum reported here would therefore be an excellent aid in the search for the gas-phase dimer.

6.3.2 Optically Selected Mass Spectra

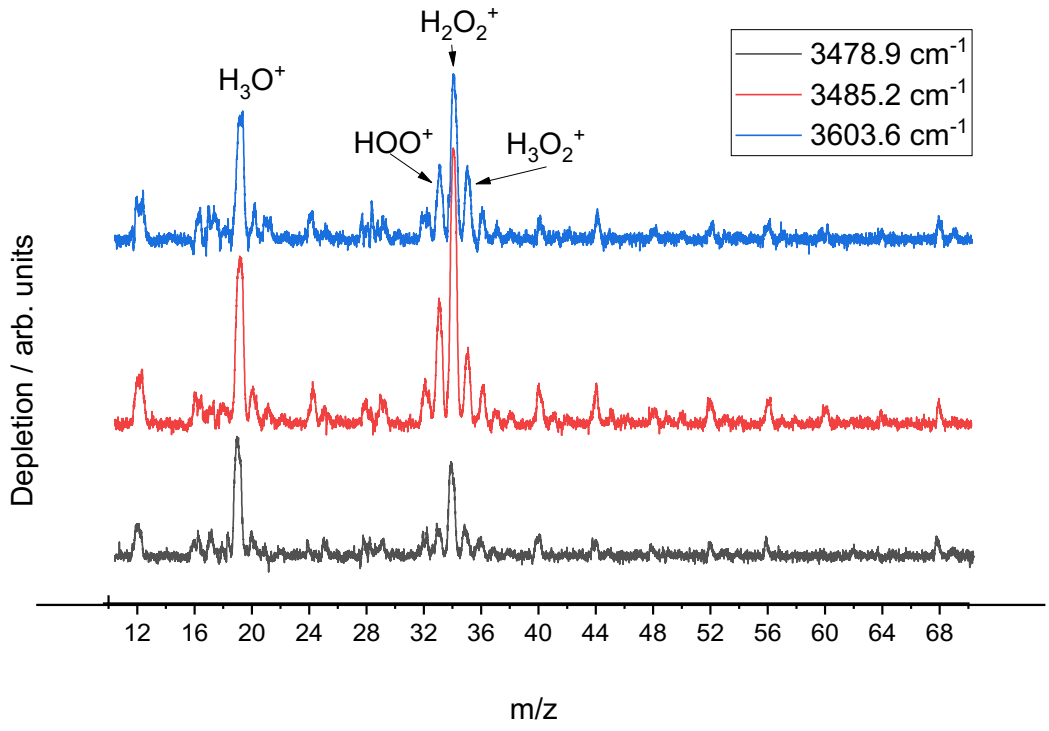

Figure 6.6. Optically selected mass spectra recorded at 3478.9 cm^{-1} (black), 3485.2 cm^{-1} (red) and 3603.6 cm^{-1} (blue). See text for details.

To examine the fragmentation pattern of the hydrogen peroxide dimer, optically selected mass spectra (OSMS) were recorded. The spectra are recorded by parking the laser on a line, and then measuring the depletion for different m/z values. Differences in the strength of the depletion signal at different m/z values give a fragmentation pattern for the species responsible for the depletion at that specific laser frequency.[18] Not only does this aid in line assignments, but provides an indication of what ions contribute the most to the depletion signal for a particular line. A mass-selected infrared spectrum can then be recorded by measuring the depletion for only

a specific ion, which is chosen based on over all depletion intensity. Mass-selected infrared spectra are employed to eliminate overlapping lines due to different species. I used the same technique in Chapter 4 of this thesis to clean up the monomer infrared spectrum of the hydrogen peroxide monomer.

Figure 6.6 shows the optically selected mass spectra recorded with the laser parked on the assigned $(H_2O_2)_2$ lines at 3603.5 and 3485.0 cm^{-1}, as well as the suspected H_2O_2-H_2O dimer line at 3478 cm^{-1}. All three OSMS show the expected $(He)_n^+$ cluster peaks every 4 m/z. The two most significant ion fragments in all three OSMS are H_3O^+ (m/z = 19) and $H_2O_2^+$ (m/z = 34). In the optically selected mass spectrum of the hydrogen peroxide monomer, I determined that the main ion produced as a result of ion fragmentation was at m/z = 18, which coincides with the H_2O^+ ion. It is unsurprising then, that the hydrogen peroxide dimer fragments to produce the H_3O^+ ion. Unlike the monomer OSMS, m/z = 34 showed the largest depletion, indicating that when the dimer is ionized, the $H_2O_2^+$ is produced, and a direct break-up of the dimer into monomer fragments is favored somewhat over fragmentation to H_3O^+. Other significant ions for $(H_2O_2)_2$ include HOO^+ at m/z = 33, and $H_3O_2^+$ at m/z = 35.

For the suspected H_2O_2-H_2O line at 3478 cm^{-1}, the depletion at m/z = 19 is stronger than at m/z = 34, which is expected for a dimer that contains both water and hydrogen peroxide. If some of the hydrogen peroxide ionizes to produce H_3O^+, and some of the dimer fragments such that the water carries one of the hydrogen bonded hydrogens from hydrogen peroxide with it, both will contribute to the depletion seen at m/z=19. In future studies, spectra of UHP in helium droplets will be mass selected at m/z=19 to enhance the water containing hydrogen peroxide clusters relative to other clusters. Doing so will help with the assignment of the H_2O_2-H_2O lines.

The mass selected spectra of the bound and free OH stretch of the $(H_2O_2)_2$ dimer is given Figure 6.7. In both cases, the mass selection reduced or eliminated the appearance of peaks resulting from other clusters. The free OH asymmetric stretch in Figure 6.7a, for example, contains no other obvious lines with the exception of the indicated hydrogen peroxide monomer lines. This indicates that nearby cluster peaks in the 3595 – 3614 cm^{-1} region are unlikely to involve water, as the OSMS revealed that such lines should still show up when selecting at m/z=34, albiet with reduced intensity. This would indicate that nearby lines in the survey spectrum such as the line observed at 3606 cm^{-1} represent hydrogen peroxide complexes with other dopants, such as N_2 or O_2. Pettersson *et al.*,[19] identified the matrix isolated H_2O_2-N_2 complex OH stretch at 3587.2 and 3582.1 cm^{-1}, which is close to the free OH stretch in argon matrix at 3581.7 cm^{-1}.[3] The close proximity of the $(H_2O_2)_2$ and H_2O_2-N_2 lines in argon matrices support the possibility of the line at 3606 cm^{-1} as belonging to the H_2O_2-N_2 dimer. An investigation of this line constitutes future work.

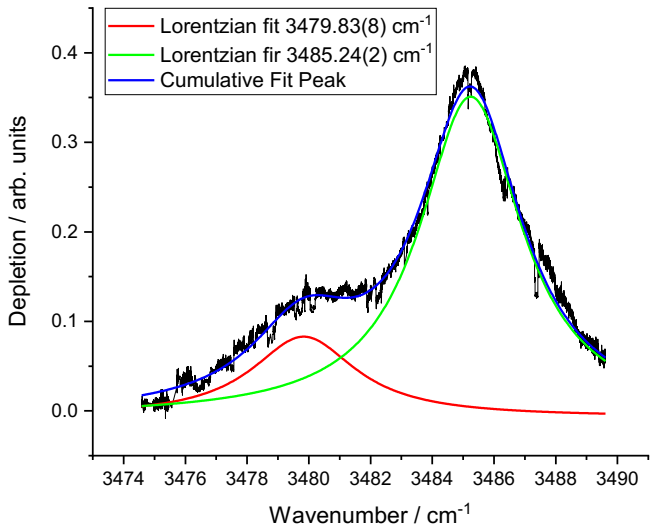

(a

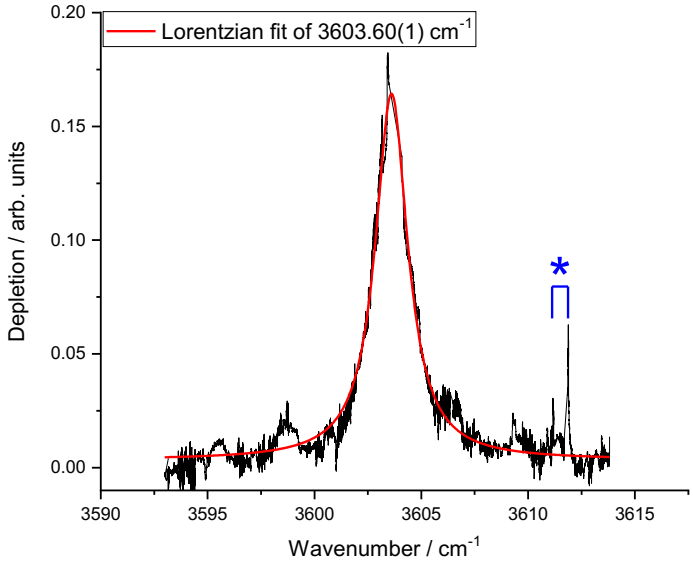

(b

Figure 6.7. (a) The mass-selected (m/z = 34) spectrum of the bound OH stretching region. A multipeak fit was performed in order to deconvolute the two overlapping lines, using a lorentzian function. Zsee text for details of data fluctuations. (b) The mass-selected spectrum in the free OH stretching region of the hydrogen peroxide dimer in helium droplets. The red line indicates the Lorentzian fit, and the blue lines marked with an asterisk indicate known hydrogen peroxide monomer lines. Mass selection at m/z = 34 eliminated other nearby cluster peaks.

In the mass selected scan of the bound OH stretch at 3485.2 cm^{-1}, the suspected H_2O_2-H_2O line remains, but with diminished intensity. This is to be expected for the H_2O_2-H_2O dimer, which likely has a similar fragmentation pattern owing to the similarities it shares with $(H_2O_2)_2$ – namely the cyclic structure and double hydrogen bond. It should be pointed out, however, that the suspected H_2O_2-H_2O line at 3479.8 cm^{-1} does appear to shift significantly to 3478.5 cm^{-1}, when the doping pressure of UHP is reduced to minimize the appearance of the line at 3485.2 cm^{-1}, while codoping with water (see Figure 6.8). It does not appear that the lineshift is a result of the borrowed intensity from the dimer line at 3485.2 cm^{-1}, as this would have shown up in the deconvolution of the two lines shown in Figure 6.7a. It is possible that there are actually two

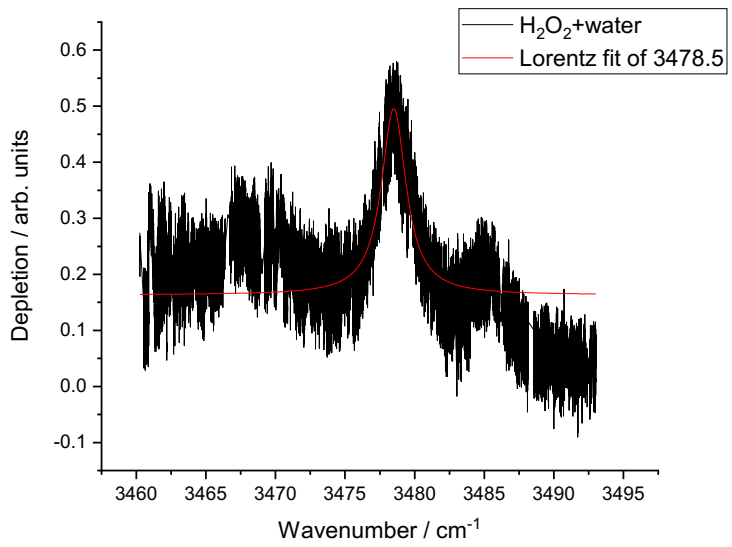

Figure 6.8. The Lorentzian line fit to the suspected H_2O_2-H_2O line in the bound OH stretching region of hydrogen peroxide. The spectrum was recorded by accepting all mass values above 6 m/z. The hydrogen peroxide doping pressure was intentionally kept low at about 2.5 x 10^{-7} Torr. The addition of water increased the total doping pressure to about 4.0 x 10^{-7} Torr.

overlapping cluster lines, both of which contain water. Under the conditions used for the survey scan in Chapter 4 (high H_2O_2 doping pressures and high water content), a broad feature is observed at 3479.5 cm^{-1}.

Electronic problems with the QMS resulted in the unusual data pattern observed in Figure 6.7a. The dips in intensity are artifacts stemming from the QMS which were artificially enhanced while smoothing and power correcting the data. I have left these in rather than alter the data. Further to this, there is a small section of data missing in Figure 67b, which was a result of a laser hop during scanning. I would typically scan over this area again to obtain the missing data, however, the electronic issues with the QMS mentioned above became more troublesome immediately after recording the spectrum. The QMS stopped functioning altogether, and as of the writing of this thesis, is still not repaired. Nevertheless, the key features including peak position and linewidths are visible in the presented data, and a fresh scan with a properly functioning QMS would not affect the assignment of the lines.

6.4 Conclusions

The infrared spectra of hydrogen peroxide in helium nanodroplets was measured using UHP as the source. The UHP source resulted in a much cleaner spectrum and a substantial reduction in the water content of the droplets compared to those recorded in Chapter 4. I assigned two lines to the hydrogen peroxide dimer (3485.2 and 3603.6 cm^{-1}). The lines were assigned using pressure dependence studies, co-doping with water, and comparisons with literature values for the dimer recorded in an argon matrix.[3] The assigned lines are consisted with a cyclic structure as reported by Engdahl *et al.*,[3] but I was not able to determine whether

the cyclic structure was UU or UD. Lines due to other hydrogen peroxide containing clusters were also observed, such as H_2O_2-H_2O, but the firm assignments of other cluster peaks represents future work.

References

[1] J. H. Baraban, P. B. Changala, J. F. Stanton, *J. Mol. Spectrosc.* **2018**, *343*, 92–95.

[2] J. V. McArdle, M. R. Hoffmann, *J. Phys. Chem.* **1983**, *87*, 5425–5429.

[3] A. Engdahl, B. Nelander, G. Karlström, *J. Phys. Chem. A* **2001**, *105*, 8393–8398.

[4] P. D. Cooper, R. E. Johnson, T. I. Quickenden, *Icarus* **2003**, *166*, 444–446.

[5] A. Engdahl, B. Nelander, *Phys. Chem. Chem. Phys.* **2000**, *2*, 3967–3970.

[6] K. Grzechnik, K. Mierzwicki, Z. Mielke, *ChemPhysChem* **2013**, *14*, 777–787.

[7] S. Pehkonen, J. Lundell, L. Khriachtchev, M. Pettersson, M. Räsänen, *Phys. Chem. Chem. Phys.* **2004**, *6*, 4607–4613.

[8] A. Engdahl, B. Nelander, *Phys. Chem. Chem. Phys.* **2004**, *6*, 730–734.

[9] S. A. Kulkarni, L. J. Bartolotti, R. K. Pathak, *Chem. Phys. Lett.* **2003**, *372*, 620–626.

[10] M. Elango, R. Parthasarathi, V. Subramanian, C. N. Ramachandran, N. Sathyamurthy, *J. Phys. Chem. A* **2006**, *110*, 6294–6300.

[11] K. Nauta, R. E. Miller, *Science* **2000**, *287*, 293–295.

[12] C. J. Burnham, S. S. Xantheas, M. A. Miller, B. E. Applegate, R. E. Miller, *J. Chem. Phys.* **2002**, *117*, 1109–1122.

[13] M. Pettersson, S. Tuominen, M. Räsänen, *J. Phys. Chem. A* **1997**, *101*, 1166–1171.

[14] M. Lewerenz, B. Schilling, J. P. Toennies, *Chem. Phys. Lett.* **1993**, *206*, 381–387.

[15] M.J. Frisch, *Gaussian 09 Revis. E01* **2009**.

[16] M. Lewerenz, B. Schilling, J. P. Toennies, *J. Chem. Phys.* **1995**, *102*, 8191–8207.

[17] J. P. Toennies, A. F. Vilesov, *Angew. Chem. - Int. Ed.* **2004**, *43*, 2622–2648.

[18] W. K. Lewis, C. M. Lindsay, R. J. Bemish, R. E. Miller, *J. Am. Chem. Soc.* **2005**, *127*, 7235–7242.

[19] J. Lundell, S. Pehkonen, M. Pettersson, M. Räsänen, *Chem. Phys. Lett.* **1998**, *286*, 382–388.

Chapter 7: Rovibrational Spectroscopy of the Cyclic Formic Acid Dimer

7.0 Introduction

Formic acid, the smallest carboxylic acid, can form dimers in a variety of single and double hydrogen bonded structures. It is the most abundant carboxylic acid in the atmosphere,[1] and its dimer is present in clouds, fogs, and aerosols.[2–4] The lowest energy cyclic dimer is, like the hydrogen peroxide dimer, a prototype for molecular complexes with double hydrogen bonds. Similar binding motifs play crucial roles in multiple-proton transfer processes in chemistry and biology, such as, for example, the base pair interactions in DNA.[5,6] Another interesting feature of the cyclic dimer is the process of hydrogen bond exchange,[7] which can result in hydrogen-bond tunneling splittings in high resolution spectra.[8–11]

The *cyc*-$(HCOOH)_2$ dimer possesses C_{2h} symmetry as a result of a symmetric double hydrogen bond and double proton exchange (see figure 7.1). Its structure has been studied using several techniques such as NMR spectroscopy,[12] Raman spectroscopy,[13,14] and infrared spectroscopy.[8,11,15–20] Several Fourier transform-infrared spectroscopic (FT-IR) studies indicate the existence of a cyclic structure in the gas phase.[16–19] Gadermann *et al*. have employed rapid scan FT-IR spectroscopy for characterization of the cyclic dimer in aerosols.[4] Recently,

Mackeprang *et al.* have used FT-IR difference spectroscopy to extract spectra of the cyclic form in a complex mixture of monomer and dimers of HCOOH.[15]

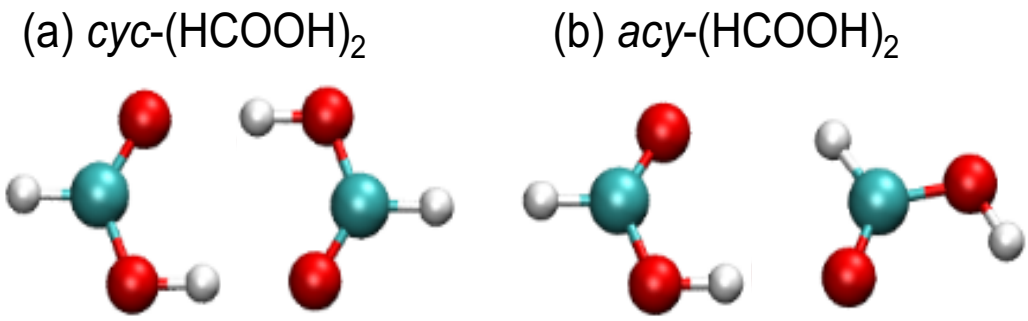

Figure 7.1. The *cyc*-(HCOOH)$_2$ (a) and *acy*-(HCOOH)$_2$ (b) formic acid dimer structures.

Formic acid dimers have also been investigated in rare-gas matrices. Gantenberg *et al.* have used pulsed deposition of formic acid into an argon matrix, and their results suggest the formation of a higher energy acyclic conformer, *acy*-(HCOOH)$_2$ upon deposition at 7K, which rearranges to the cyclic structure up annealing at 40 K.[21] This has been corroborated by matrix isolation studies conducted by Ito[22] and Marushkevich *et al*.[23] More recently, the cyclic complex was identified, along with products of X-ray irradiated isolated formic acid, in noble gas maxtrices (Xe, Kr, Ar, and Ne).[24]

In 2002, the first completely analyzed gas phase high-resolution infrared spectrum of (DCOOH)$_2$ was published by Madeja and Havenith.[8] The proton transfer in *cyc*-(HCOOH)$_2$ has also been probed by infrared high-resolution spectroscopy in the region of the antisymmetric C–O stretch vibration (1221 - 1227 cm^{-1}).[25] Recently, Zhang et al. measured rotationally resolved infrared spectra of (HCOOH)$_2$, (HCOOD)$_2$, and HCOOH-HCOOD complexes under

jet-cooled condition in the 7.2 μm region and determined the tunneling splitting.[26] The formic acid dimer has also been studied using the technique of helium nanodroplet spectroscopy.[27] The higher energy *acy*-$(HCOOH)_2$ was trapped in helium nanodroplets due to rapid cooling within the droplets, which prevents rearrangement to lower energy structures. The authors did not observe *cyc*-$(HCOOH)_2$ however, so there remains a lack of high-resolution infrared spectroscopic information of *cyc*-$(HCOOH)_2$ in helium nanodroplets. In addition to these experimental studies, *ab initio* studies have been carried out that clearly show that the cyclic structure corresponds to the global minimum on the potential energy surface.[28–30]

In this chapter, I report infrared depletion spectra of formic acid dimers, including deuterated isotopologues, embedded in helium nanodroplets. The results indicate the formation of the *cyc*-$(HCOOH)_2$ dimer with double hydrogen-bonds in addition to the *acy*-$(HCOOH)_2$ dimer, which has been identified in a previous study.[27] The identification of the *cyc*-$(HCOOH)_2$ isomer is strongly supported by the observed rotational contour for the ν_{18}(C–H) stretching vibration. The formation mechanism of most stable dimer structure in superfluid helium is discussed.

7.1 Experiment

The details of the helium nanodroplet apparatus are described in detail in Chapter 2. For this experiment, ultrapure helium gas at a backing pressure (P_0) of 50 bar was expanded through a pinhole nozzle cooled to 19 – 20 K, producing droplets with an average size of ~3200 atoms per droplet.[31] Formic acid was introduced into the skimmed droplet beam in a doping cell downstream of the nozzle chamber. The pressure of formic acid in the doping call was held at

2.5×10^{-7} Torr.

Two continuous wave infrared optical parametric oscillator (OPO) systems (Lockheed-Martin Aculight Argos SF-15) were used to measure the CH and OH stretching modes of the formic acid dimer. Module B covers the range of 3125 - 4000 cm^{-1} and module C covers the range of 2560 – 3125 cm^{-1}. Both modules were operated using the automated tuning method[32] detailed in Chapter 3 of this thesis. The idler output of the OPO was overlapped with the droplet beam in a coaxial orientation. A quadrupole mass spectrometer was used to measure the ion signal of the droplet and dopants, which were ionized through electron impact ionization at 110 eV. When infrared photons are resonant with a dopant transition, the energy absorbed is quenched by the helium bath, resulting in evaporation of some of the helium atoms. When the droplets are reduced in size, the ion signal detected by the mass spectrometer is reduced as a result of the reduction in ionization cross-section of the droplets.

Formic acid (HCOOH, purity 98%, Sigma-Aldrich), formic-d acid (DCOOH, isotopic purity 98%, Cambridge Isotope Laboratory), and formic acid-d (HCOOD, isotopic purity 95%, Sigma-Aldrich) were obtained commercially. The sample was degassed using multiple consecutive freeze-pump-thaw cycles.

7.2 Theoretical calculations

The experimental measurements were complemented by quantum chemical calculations. I employed the GAUSSIAN 09 program[33] to calculate the geometries, vibrational wavenumbers, IR intensities, and molecular constants of HCOOH dimers using density functional theory with the B3PW91 functional[34] and the aug-cc-pVTZ basis set.[35] According

to the B3PW91/aug-cc-pVTZ energies, *cyc*-$(HCOOH)_2$ is more stable than *acy*-$(HCOOH)_2$ by 28.7 kJ mol^{-1}, close to the value of 28 kJ mol^{-1} calculated with the B3LYP/TZ2P(f,d)+diff method and only slightly different from the CCSD(T)/aug-cc-pVTZ value of 26.3 kJ mol^{-1}.[36]

The frequencies of the infrared active modes predicted with the B3PW91/aug-cc-pVTZ method are 3103 cm^{-1} for the asymmetric O–H stretching (ν_{17}) and 3043cm^{-1} for asymmetric C–H stretching vibrations (ν_{18}) in *cyc*-$(HCOOH)_2$, as listed in Table 7.1. In case of *acy*-$(HCOOH)_2$, the predicted frequencies are 3739 and 3319 cm^{-1} for free (ν_1) and bound O–H stretching (ν_2), respectively, and 3103 and 3037 cm^{-1} for free (ν_3) and bound C–H stretching (ν_4) vibrations, respectively, as listed in Table 7.2.

The rovibrational assignment, fitting, and simulation of the observed C–H stretching band of the *cyc*-$(HCOOH)_2$ spectrum were performed with the PGOPHER program.[43] The rotational constants for ground state (A'', B'', C'') and upper state (A', B', C') vibrational levels were obtained by a vibrational-rotational coupling analysis through anharmonic calculations at the B3PW91/aug-cc-pVTZ level of theory. The calculated rotational constants were scaled by factor of 2.5 as an initial guess for the fitting procedure.

Table 7.1 Comparison of observed wavenumbers in helium nanodroplets and B3PW91/aug-cc-pVTZ predicted O–H and C–H stretching infrared bands of *cyc*-$(HCOOH)_2$ and its deuterated isotopologues and their corresponding lines reported in the gas phase and in argon matrices.

ν_i	*cyc*-$(HCOOH)_2$[a]			*cyc*-$(HCOOD)_2$[b]			*cyc*-$(DCOOH)_2$[c]		
	^{4}He droplet	Gas phase	Ar-matrix	^{4}He droplet	Gas phase	Ar-matrix	In ^4He_n	Gas phase	Ar-matrix
ν_{17} (O-H/D)	3082.30/ 3081.83?	3081[d]	3072[h]		2290[e]	2271.8, 2259.4[j]	3080.11	3078[d]	3069[i]
		3000[e]	3076[i]		2314[g]			3083.4[f]	
		3102.2[f]						3098[g]	
		3110[g]							
ν_{18} (C-H/D)	R 2940.56	2939.7[d]		2957.76	2936.2[d]			2209, 2237[d]	
	Q 2940.43	2944[e]	2947[i]	2957.44	2949[e]				2213[i]
	P 2940.31	2938.4[f]		2956.98	2960[g]			2238[f]	
		2957[g]			2951.5[k]			2251[g]	
								2210.4[k]	

[a]B3PW91/aug-cc-pVTZ predicted wavenumbers for ν_{17} and ν_{18} modes of *cyc*-$(HCOOH)_2$ are 3103.4 and 3042.8 cm^{-1}, respectively.
[b]B3PW91/aug-cc-pVTZ predicted wavenumbers for ν_{17} and ν_{18} modes of *cyc*-$(HCOOD)_2$ are 2247.3 and 3066.7 cm^{-1}, respectively.
[c]B3PW91/aug-cc-pVTZ predicted wavenumbers for ν_{17} and ν_{18} modes of *cyc*-$(DCOOH)_2$ are 3081.0 and 2272.6 cm^{-1}, respectively.
[d]Jet-cooled cavity ring-down infrared spectroscopy.[19]
[e]Gas phase infrared absorption spectroscopy.[37]
[f]Gas phase infrared absorption spectroscopy.[38]
[g]Gas phase prism based infrared absorption spectroscopy.[39]
[h]Matrix-isolation infrared spectroscopy.[40]
[i]Rare gas matrix-isolation infrared spectroscopy.[22]
[j]Matrix-isolation infrared spectroscopy.[23]
[k]Jet-cooled action spectroscopy.[41]

Table 7.2 Comparison of observed wavenumbers in helium nanodroplets and the B3PW91/aug-cc-pVTZ predicted O–H and C–H stretching infrared band of *acy*-$(HCOOH)_2$ and its deuterated isotopologues and their corresponding lines reported in nanodroplets and in rare gas matrix.

ν_i	*acy*-$(HCOOH)_2$			*acy*-$(HCOOD)_2$			*acy*-$(DCOOH)_2$	
	^{4}He droplet	Ar-matrix	B3PW91/aug-cc-pVTZ	^{4}He droplet	Ar-matrix	B3PW91/aug-cc-pVTZ	^{4}He droplet	B3PW91/aug-cc-pVTZ
ν_1 (O–H/ D_{free})	3560.21	3540.1 [b,c]	3738.9	2626.33 2624.74	2612.1, 2610.0[c]	2718.5	3561.45	3738.8
ν_2 (O–H/ D_{bound})		3142.8, 3101.4 [b] 3184, 3168, 3154, 3142, 3101[c]	3319.2			2420.0		3318.2
ν_3 (C–H/ D_{bound})			3103.2			3103.9		2311.3
ν_4 (C–H/ D_{free})	2931.38 2931.00		3036.9	2935.77 2934.79		3038.1		2254.8

[b]Matrix-isolation infrared spectroscopy.[42]
[c]Matrix-isolation infrared spectroscopy.[40]
[d]Tentative assignment for hydrogen bonded O–H stretching vibration of *acy*-$(HCOOH)_2$

7.3 Results and Discussion

7.3.1 Survey Scan

A survey spectrum was collected with ~2.5 x 10^{-7} torr formic acid partial pressure in the doping cell and collecting all mass channels with m/z > 29. A number of lines were observed in the 3575 – 3548 cm^{-1} and 3085 – 2928 cm^{-1} regions, see Figure 7.2. These lines are categorized into four different groups based on known lines of the monomer, pressure dependent studies for the homodimers, and N_2 doping pressure tests for an N_2 containing heterodimer. These four groups of lines are marked with *t*-FA, *cyc*-FAD, *acy*-FAD, and FA-N_2, respectively, as shown in Figure 7.2.

Rotationally resolved lines in the higher (3573 – 3566 cm^{-1}) and lower frequency regions (2947 – 2943.5 cm^{-1}) marked with *t*-FA in Figure 7.1 are attributed to the monomer, consistent with the reported lines for the *trans*-HCOOH monomer isolated in helium nanodroplets.[27] The observed lines at 3550 and 2939 cm^{-1} labeled with FA-N_2 in Figure 7.2 belong to a complex involving formic acid and nitrogen. To make sure that these lines are related to the HCOOH-N_2 complex, the droplets were intentionally doped with nitrogen. Upon addition of N_2, the intensity of lines marked FA-N_2 goes up. The corresponding infrared absorption features of FA-N_2 in an Ar-matrix were previously reported to be at 3531.7 and 2952.5 cm^{-1}.[44] Further details of this complex comprise future work and are not detailed in this chapter.

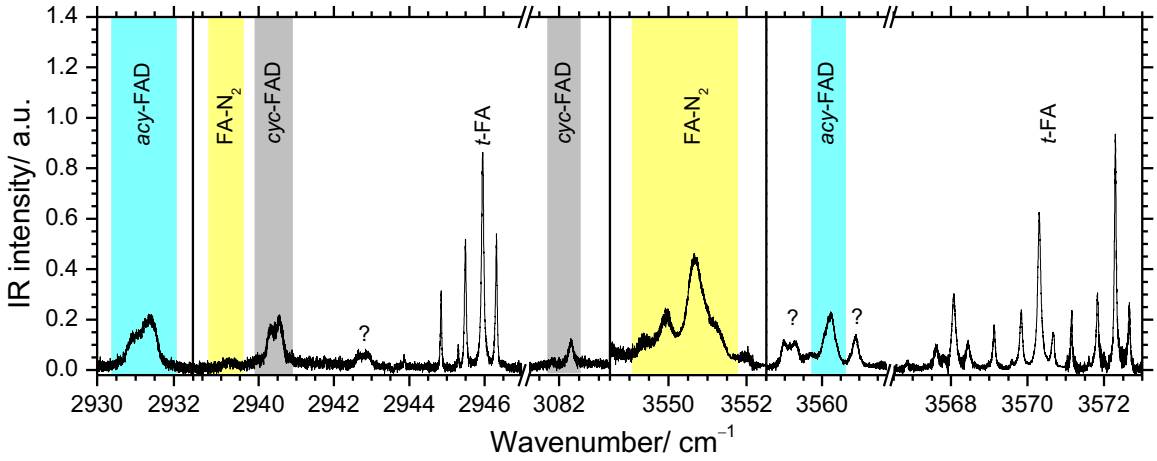

Figure 7.2. Survey scan of HCOOH in helium nanodroplets. The infrared depletion spectra were recorded on mass channels with m/z > 29 with an HCOOH doping cell partial pressure of ~2.5 x 10^{-7} torr. Features marked with *t*-FA, *cyc*-FAD, *acy*-FAD, and FA-N_2 correspond to the *trans*-HCOOH monomer, cyclic and acyclic dimers of *trans*-HCOOH, and the HCOOH-N_2 complex, respectively.

The broad features in Figure 7.2 marked with *acy*-FAD at 3560 and 2931 cm^{-1} and listed in Table 7.2 are readily assigned to *acy*-$(HCOOH)_2$, consistent with previously reported lines for bound O–H and free C–H stretching vibrations of *acy*-$(HCOOH)_2$ embedded in helium nanodroplets.[27] The intensity of the broad features near 3082 and 2940 cm^{-1}, marked with *cyc*-FAD in Figure 7.2 and listed in Table 7.1, decreases upon addition of H_2O. However, upon addition of N_2, the P-branch at 2940 cm^{-1} slightly increases as shown in Figure 7.3, whereas the line at 3082 cm^{-1} decreases in intensity, as expected. The intensity increase at 2940 cm^{-1} upon addition of N_2 could be due to interference of infrared absorption related to the HCOOH-N_2 complex. Based on pressure dependence studies, theoretical calculations, and a rotational contour analysis, to be discussed in the following sections, I have assigned these lines to the HCOOH dimer with a cyclic structure.

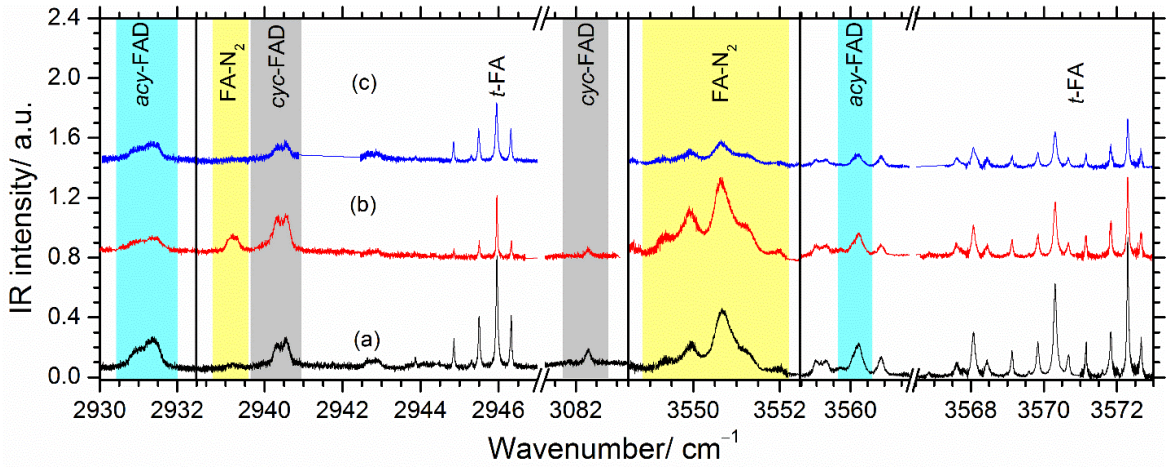

Figure 7.3. Infrared depletion spectra recorded with doping cell filled with HCOOH (a), HCOOH + N_2 (b), and HCOOH + H_2O (c). Features marked with *t*-FA, *cyc*-FAD, *acy*-FAD, FA-N_2 correspond to monomer, cyclic and acyclic dimers, and N_2 complex of *trans*-HCOOH, respectively.

7.3.2 Pressure dependence

To assign signals to a specific species, I monitored the change in intensity of the depletion signal as a function of HCOOH partial pressure. The results for selected features at 3572.30, 3082.30, and 2940.31 cm^{-1} are displayed in Figure 7.4. The probability, P_n, for pick-up of n dopant molecules by a helium droplet is given by a Poisson distribution,[45]

$$P_n(\rho) = \frac{(\sigma l \rho)^n}{n!} \exp(-\sigma l \rho). \qquad (1)$$

Here, $(\sigma l \rho)$ is the average number of collisions which leads to capture of the particles by the droplets, in which ρ, σ, and l are the number density of molecules, capture cross section, and length of the doping cell, respectively.

The data sets plotted in Fig. 7.4 were fitted to a Poisson distribution to yield the following n-values: n=1 for the line at 3572.30 cm^{-1}, as expected for the monomeric (n = 1) form of

HCOOH, and n=2 for the signals at 3082.30 and 2940.31 cm^{-1}, consistent with a dimeric form. From Fig. 7.4, the optimal formic acid doping pressure for the dimer signal is ~ 5 x10^{-7} torr. However, depletion spectra were measured at pressures of ~2.5x10^{-7} torr to avoid formation of higher order HCOOH clusters.

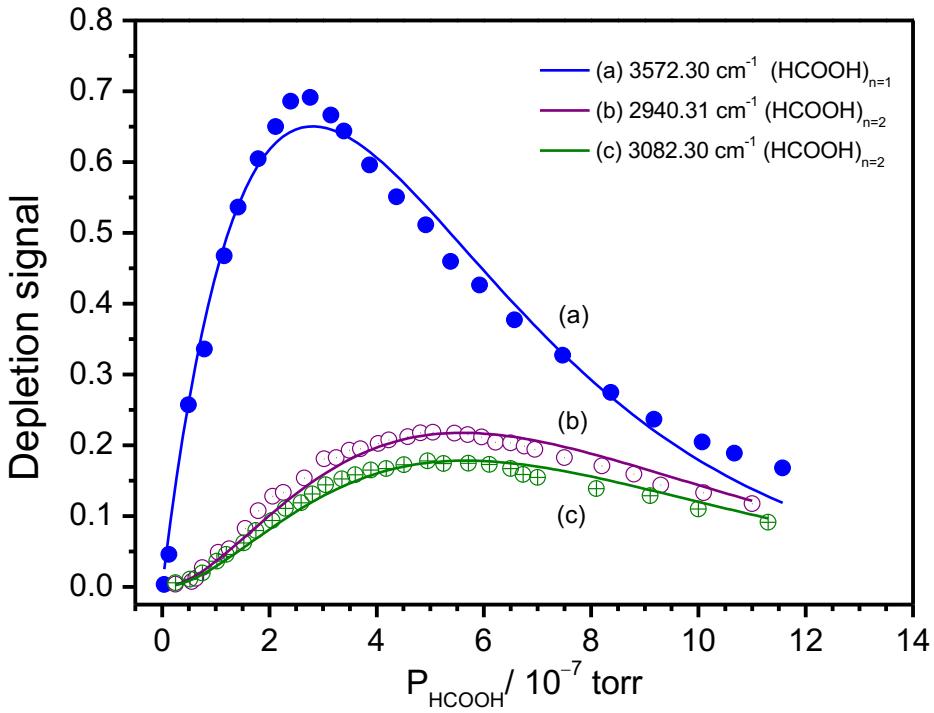

Figure 7.4. Variation of signal intensity for the HCOOH monomer in the O–H stretch and dimer in the "free" C–H stretch and "hydrogen bonded" O–H stretch regions in dependence of the pickup pressure. Fitted lines correspond to the expected variation of a monomer (blue) and cyclic dimer signals (purple and green) if we assumed a Poisson distribution.

7.3.3 Assignment of the $(HCOOH)_2$ lines to cyc-*$(HCOOH)_2$*

In the region between 3085 and 2928 cm^{-1} several bands were observed (see Figure 7.2). The line at 3082 cm^{-1} and the partially rotationally resolved lines at 2940.56, 2940.43, and

2940.31 cm^{-1} are marked with *cyc*-FAD in Figure 7.1 and listed in Table 7.1. The pickup pressure/intensity correlations in Figure 7.4 support the assignment of these lines to the formic acid dimer. This assignment is further supported by proximity to gas-phase values reported at 3081 and 2939.7 cm^{-1}, which were measured by cavity ring down spectroscopy.[19,20]

To corroborate the frequency shifts of the dimer lines with respect to the monomer transitions, I plot the experimental spectrum with features of HCOOH monomer and dimers in helium droplets (Figure 7.5 a) and compare it with B3PW91/aug-cc-pVTZ simulated spectra for *trans*-HCOOH, *cyc*-$(HCOOH)_2$, and *acy*-$(HCOOH)_2$ in Figure 7.4 b-d. The spectra were simulated using scaled harmonic vibrational wavenumbers (scaling factors 0.9546 for region above 3200 cm^{-1} and 0.9427 for that below 3200 cm^{-1}) and IR intensities from the DFT calculations. The scaling factors were obtained by taking the ratio of measured vibrational wavenumbers of the HCOOH monomer in helium nanodroplets to the calculated values. The experimental and calculated frequency shifts in going from monomer to dimer are, in general, quite consistent. However, a discrepancy is found between the observed red shift (488.37 cm^{-1}) in helium droplets and the DFT value of 574 cm^{-1} for the hydrogen bonded O–H stretching vibration in *cyc*-$(HCOOH)_2$. I also simulated spectra corresponding to traces (b - d) in Figure 7.4 from MP2/aug-cc-pVTZ calculations. Although the MP2 predicted O–H vibrational band position is close to the observed value, the intensity of this band is found to be too large, similar to that of the C–H stretching vibration. Furthermore, the MP2 calculated C–H band is blue shifted, which is not in agreement with observations from helium nanodroplet or jet experiments.

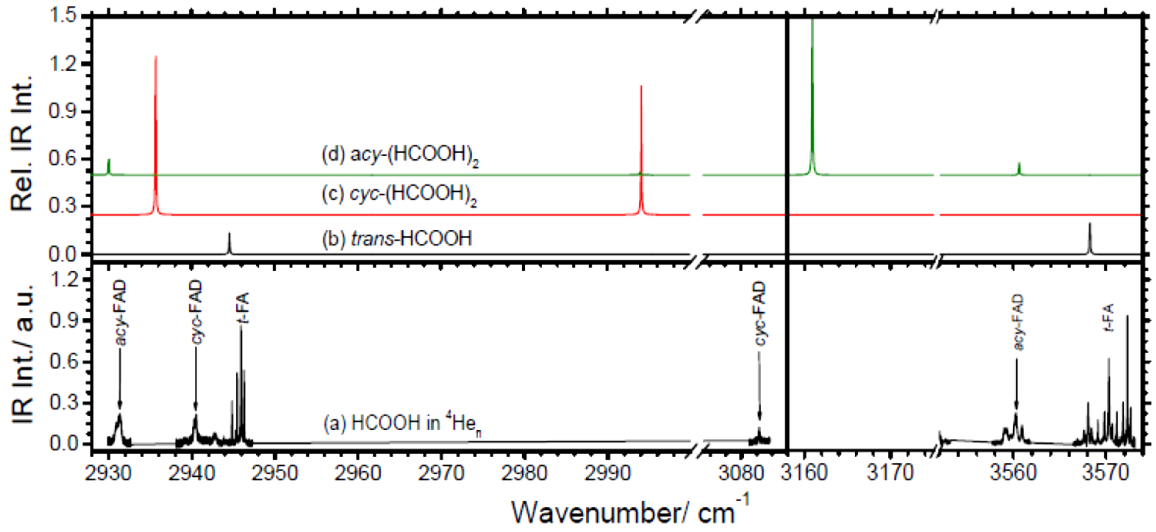

Figure 7.5. Comparison of the experimental spectrum with those simulated for possible candidates. (a) The spectrum of HCOOH doped helium nanodroplets. Infrared spectra of *trans*-HCOOH (b), *cyc*-$(HCOOH)_2$ (c), and *acy*-$(HCOOH)_2$ (d) were simulated with FWHM = 0.025 cm^{-1} and using scaled harmonic vibrational wavenumbers (scaling factors 0.9546 for region above 3200 cm^{-1} and 0.9427 for that below 3200 cm^{-1}) and IR intensities predicted with the MP2/aug-cc-pVTZ method.

The line at 3082.30 cm^{-1} is assigned to the bound O–H stretching vibration in *cyc*-$(HCOOH)_2$, which is red-shifted by 488.37 cm^{-1} relative to the monomer. For the frequency shift estimation, I used the band origin of 3570.67 cm^{-1} for the free O–H stretching vibration in the HCOOH monomer isolated in helium droplets.[27] This large shift is due to the strong hydrogen bonding in the cyclic dimer. The C–H stretch vibration, observed at 2940.402(υ_0) cm^{-1}, is red-shifted by 4 cm^{-1} relative to monomer at 2944.42 cm^{-1}.[27] This small red-shift of the C–H stretch vibration is a result of the only weak perturbation upon complex formation. The determined red-shifts for the O–H and C–H stretching vibrations of *cyc*-$(HCOOH)_2$ in droplets are close to

those from an argon matrix-isolation FT-IR study (470 and 3 cm^{-1})[22] and the gas phase FT-IR study of Wachs et al. (468.3 and 3.7 cm^{-1}).[38] According to Maréchal's gas phase FT-IR study, the O–H stretch vibrational band is red-shifted by 567 cm^{-1}, whereas C–H stretching vibrational band is blue-shifted by 3 cm^{-1}.[37] The room temperature gas phase FT-IR spectra are complicated by the overlap between broad C–H stretch and relatively sharp O–H stretch vibrational bands of the dimers; as a result finding accurate individual vibrational band position could be difficult. Recently, Mackeprang et al.[15] used difference FT-IR spectroscopy to extract the spectra of cyclic formic acid dimer in the gas phase, and found red-shifts for both O–H and C–H stretching vibrations of 470.5 and 3.1 cm^{-1}, respectively, for *cyc*-$(HCOOH)_2$.

7.3.4 Deuterated Isotopologues

Deuterium-substitution experiments can provide additional support for the assignment of lines in the *cyc*-FAD and *acy*-FAD groups to the *cyc*-$(HCOOH)_2$ and *acy*-$(HCOOH)_2$ dimers, respectively. Figure 7.6 shows depletion spectra of HCOOD monomer and dimers in the O–D and C–H stretching region. I observed two sets of rotationally resolved sharp lines in the 2634 – 2630 cm^{-1} and 2942 – 2939 cm^{-1} regions, marked with *t*-FAd in Figure 7.6. The pattern of these sharp lines are similar to those of the O–H and C–H stretching vibrations of monomeric *trans*-HCOOH in droplets and close to the previously reported lines for *trans*-HCOOD at 2637 and 2942 cm^{-1} in the gas phase,[37] and 2619.5/2618.0 and 2961.2 cm^{-1} in an Ar-matrix.[42] A line at 2940.1 cm^{-1} for the C–H stretching band of *trans*-HCOOD under jet-cooled conditions has been reported by Yoon et al.[41] These observed sharp lines were unambiguously assigned to the O–D and C–H stretching vibrations of *trans*-HCOOD in an earlier report.[46] A broad band feature

with satellite peaks (2957.76 and 2956.98 cm^{-1}) observed at 2957.44 cm^{-1} is marked with *cyc*-FADd in Figure 7.5 and listed in Table 7.1. This transition at 2957.44 cm^{-1} is attributed to the C–H stretching vibration of *cyc*-$(HCOOD)_2$. The observed isotopic shift of *cyc*-$(HCOOD)_2$ is consistent with the B3PW91/aug-cc-pVTZ predicted shift as listed in Table 7.3. This observed

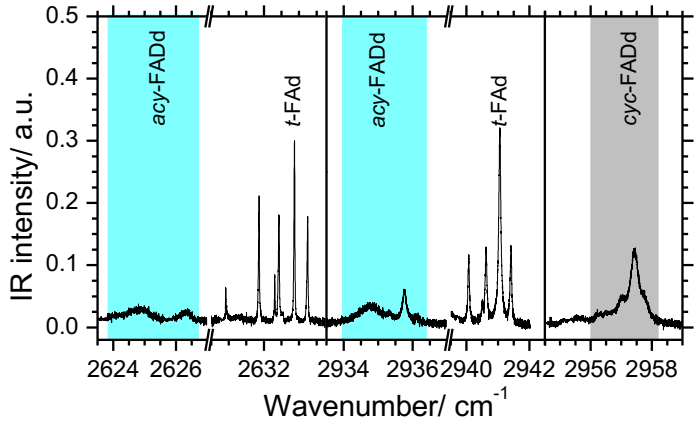

Figure 7.6. Survey scan of HCOOD in helium nanodroplets. Infrared depletion spectra were recorded on mass channels with m/z > 29 with an HCOOD doping cell partial pressure of ~2.5 x10^{-7} torr. Features marked with *t*-FAd, *cyc*-FADd, and *acy*-FADd corresponds to *trans*-HCOOD monomer and cyclic and acyclic dimers, respectively.

line is in a different position than the corresponding line from a jet-cooled cavity ring-down spectrum (2936.2 cm^{-1}) of *cyc*-$(HCOOD)_2$.[19] However, it does appear between the corresponding features in a jet-cooled action spectrum (2951.5 cm^{-1})[41] and a room temperature infrared absorption spectrum (2960.0 cm^{-1}) in the gas phase.[39]

In addition, I observed a broad doublet at 2626.33/2624.74 cm^{-1} and a doublet consisting of a broad and a sharp feature at 2935.77 cm^{-1} and 2934.79 cm^{-1}, respectively, as marked with *acy*-FADd in Figure 7.6. Their intensities decrease upon addition of N_2 in the second doping cell.

Out of these two sets of lines, those in the first set have been reported at 2612.1/2610.0 cm^{-1} in Ar-matrix, see Table 7.2.[40] The lines at 2626.33/2624.74 cm^{-1} and at 2935.77/2934.79 cm^{-1} are assigned to the O–D and C–H stretching vibrations of *acy*-$(HCOOD)_2$, respectively, based on wavenumber shifts with respect to the monomer (*trans*-HCOOD) and the expected isotopic shifts for the acyclic dimer, as found in Table 7.4.

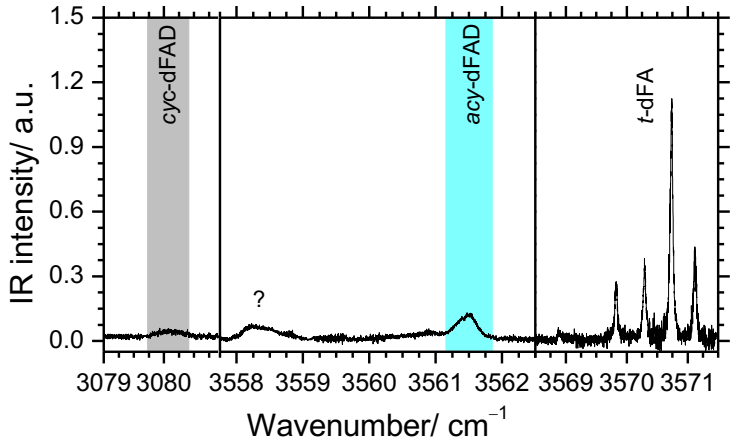

Figure 7.7. Survey scan of DCOOH in helium nanodroplets. Infrared depletion spectra were recorded on mass channels with m/z > 30 with a DCOOH doping cell partial pressure at ~2.5 x10^{-7} torr. Features marked with *t*-dFA, *cyc*-dFAD, and *acy*-dFAD correspond to the *trans*-DCOOH monomer, and cyclic and acyclic dimers, respectively.

The depletion spectra of the DCOOH monomer and its dimers and the results are presented in Figure 7.7. We observed a set of rotationally resolved sharp lines in the 3572 – 3568 cm^{-1} region, marked with *t*-dFA in Figure 7.6. These rotationally resolved lines are attributed to the O–H stretching vibration of monomeric *trans*-DCOOH, consistent with reported lines for *trans*-DCOOH in helium nanodroplets.[27] A weaker broad band feature observed at 3080.11 cm^{-1} is labeled with *cyc*-dFAD in Figure 7.7 and listed in Table 7.1. The intensity of this line decreases upon N_2 addition. This feature is close to the reported line at 3078 cm^{-1} of jet-cooled

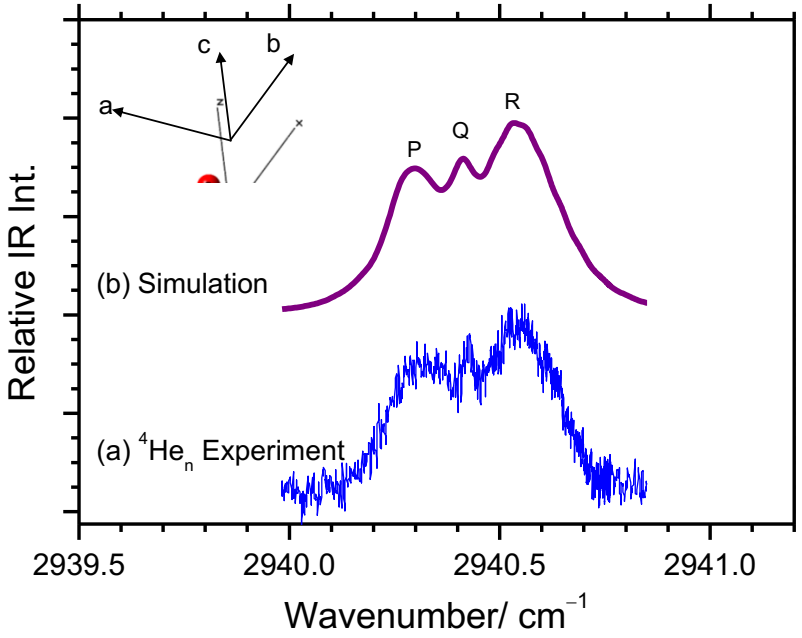

Figure 7.8. (a) An experimental spectrum of the ν_{18} band of *cyc*-$(HCOOH)_2$ embedded in helium nanodroplets. (b) A simulated spectrum using the molecular constants given in Table 7.5, a rotational temperature 0.38 K, and Lorentzian linewidths of 0.067 cm^{-1}.

cyc-$(DCOOH)_2$,[19] but slightly blue-shifted compared to the value of 3069 cm^{-1} observed in an Ar-matrix[22] and red-shifted with respect to the gas phase value of 3098 cm^{-1}.[39] We assign this line to the O–H stretching vibration of *cyc*-$(DCOOH)_2$. This assignment is consistent with the direction of the band shift with respect to the monomer, and the expected isotopic shift listed in Table 7.3. Another broad feature observed at 3561.45 cm^{-1}, is designated with *acy*-dFAD in Figure 7.7 and listed in Table 7.2. This broad feature is attributed to the free O–H stretching vibration of *acy*-$(DCOOH)_2$, consistent with the expected shift with respect to the monomer peak, and with the isotopic shift listed in Table 7.4.

7.3.5 Rotational contour analysis

Broad features were observed for the C–H stretch vibrational mode (ν_{18}) of *cyc*-$(HCOOH)_2$, which is attributed to partially resolved rotational fine structure. It consists of three bands at 2940.56, 2940.43, and 2940.31 cm^{-1} with FWHMs 0.215, 0.021, and 0.229 cm^{-1}, respectively. A rotational contour analysis of the ν_{18} mode provides further support for the assignment to *cyc*-$(HCOOH)_2$. Previously, only ground state rotational constants for the cyclic formic acid dimer in the gas phase have been reported, which are based on electron diffraction[47] and fs DFWM measurements under jet-cooled conditions (~60 K).[48] Both ground state and excited state rotational constants have been reported of the antisymmetric C–O stretch vibration at 1221.0 – 1226.7 cm^{-1}, based on an observed gas phase high-resolution spectrum.[25]

The rotational band contour for the ν_{18}(C–H) fundamental band of *cyc*-$(HCOOH)_2$ in helium droplets were fitted using the PGOPHER program.[43] Scaled B3PW91/aug-cc-pVTZ calculated rotational constants A', A'', B', B'', C', and C'' (see Table 7.5, prime and double primes indicate the vibrationally excited and ground state, respectively), a temperature of 0.38 K, and a Lorentzian width of 0.067 cm^{-1} were used for the simulation. Figure 7.8 shows the result from the fitting procedure together with the experimental spectrum. From the fit, I found a band origin frequency of 2940.402(2) cm^{-1} for the C–H stretch vibration. This frequency is close to the jet-cooled gas phase value of 2939.7 cm^{-1}.[20] The ν_{18} band is mostly *b*-type with a significant P and R branch; the weighting of types is *a*: *b*: *c* = 0.22:0.78:0.0. (The projection of dipole derivatives for the ν_{18} vibrational mode of *cyc*-$(HCOOH)_2$ onto the inertial axes *a*, *b*, and *c* is shown in the inset of Figure 7.7.) The rotational constants A', B', and C', determined in the fitting procedure are reduced from the gas phase values by 63%, 67%, and 74%, respectively (see Table 7.5),

which is a result of helium density following the dimer rotation.

Table 7.3 Comparison of observed and B3PW91/aug-cc-pVTZ calculated vibrational wavenumbers (cm^{-1}) and isotopic ratios for *cyc*-$(HCOOH)_2$.

ν_i	*cyc*-$(HCOOH)_2$		*cyc*-$(HCOOD)_2$			*cyc*-$(DCOOH)_2$		
	^{4}He droplet	B3PW91 /aug-cc-pVTZ	^{4}He droplet	B3PW91/aug-cc-pVTZ	Isotopic ratio[a]	^{4}He droplet	B3PW91/ aug-cc-pVTZ	Isotopic ratio[a]
ν_1(O–H/D_{sym})		2950.2 (0.0)		2178.1 (0.0)	(0.7383)		2949.6 (0.0)	(0.9998)
ν_2(C–H/D_{sym})		3068.5 (0.0)		3068.0 (0.0)	(0.9998)		2276.4 (0.0)	(0.7419)
ν_{17}(O–H/D_{asym})	3082.30 3081.83?	3103.4 (1293)		2247.3 (1547)	(0.7241)	3080.11	3081.0 (2870)	0.9993 (0.9928)
ν_{18}(C–H/D_{asym})	R 2940.56 Q 2940.43 P 2940.31	3042.8 (1723)	2957.76 2957.44 2956.98	3066.7 (87)	1.0058 (1.0078)		2272.6 (176)	(0.7469)

[a]Experimental isotopic ratios are listed; these values are the ratio of vibrational wavenumbers of minor isotopologues to that of the most abundant one. Calculated ratios are listed in parentheses.

Table 7.4 Comparison of observed and B3PW91/aug-cc-pVTZ calculated vibrational wavenumbers (cm^{-1}) and isotopic ratios for *acy*-$(HCOOH)_2$.

ν_i	*acy*-$(HCOOH)_2$		*acy*-$(HCOOD)_2$			*acy*-$(DCOOH)_2$		
	^{4}He droplet	B3PW91/aug-cc-pVTZ	^{4}He droplet	B3PW91/aug-cc-pVTZ	Isotopic ratio[a]	^{4}He dropet	B3PW91/aug-cc-pVTZ	Isotopic ratio[a]
ν_1(O–H/D_{free})	3560.21	3738.9 (70)	2626.33 2624.74	2718.5 (42)	0.7374 (0.7271)	3561.45	3738.8 (70)	1.0002 (0.9999)
ν_2(O–H/D_{bound})	3225?[b]	3319.2 (1029)		2420.0 (544)	(0.7291)		3318.2 (1059)	(0.9997)
ν_3(C–H/D_{bound})	n.o.	3103.2 (15)		3103.9 (9.3)	(1.0002)		2311.3 (29)	(0.7448)
ν_4(C–H/D_{free})	2931.38 2931.00	3036.9 (102)	2935.77 2934.79	3038.1 (59)	1.0014 (1.0004)		2254.8 (82)	(0.7425)

[a]Experimental isotopic ratios are listed; these values are the ratio of vibrational wavenumbers of minor isotopologues to that of the most abundant one. Calculated ratios are listed in parentheses.
[b]Reported line observed in super-fluid helium nanodroplets; tentatively assigned to the hydrogen bonded O–H stretching vibration of *acy*-$(HCOOH)_2$.[27]

Table 7.5 Summary of molecular constants for *cyc*-$(HCOOH)_2$ in liquid helium nanodroplets (^4He_n), reported in the gas phase and obtained with the B3PW91/aug-cc-pVTZ method.

Constants	ν_{18}(C–H)			
	^{4}He droplet	Gas phase	B3PW91/aug-cc-pVTZ	Δ
υ_0 (cm^{-1})	2940.402(2)	2939.7[a]	3042.8	+0.70
A''(cm^{-1})	0.075(1)	0.2022732[b]	0.201802	–0.1278(63%)
B''(cm^{-1})	0.0279(6)	0.0767864[b]	0.079254	–0.0489(64%)
C''(cm^{-1})	0.0128(2)	0.0555384[b]	0.056916	–0.0427(77%)
A'(cm^{-1})	0.075(1)	n.o.	0.201747	–0.1267(63%)[c]
B'(cm^{-1})	0.0261(5)	n.o.	0.080395	–0.0543(67%)[c]
C'(cm^{-1})	0.0147(2)	n.o.	0.057506	–0.0428(74%)[c]
T (K)	0.38	≈ 60	298	

[a]Jet-cooled cavity ring-down spectroscopy.[19,20]
[b]Femtosecond degenerate four-wave mixing (fs DFWM).[48]
[c]B3PW91/aug-cc-pVTZ calculated rotational constants used for estimation of differences.

7.3.6 The formation mechanism of the cyclic formic acid dimer in helium nanodroplets

The formation of the cyclic conformer of the formic acid dimer from the monomers is an exothermic process, liberating 58 kJ mol^{-1}. The exothermicity of the acyclic form is less (27 kJ mol^{-1}), as predicted with the B3PW91/aug-cc-pVTZ method. Inert gas matrix isolation studies suggest that the formation of the cyclic dimer occurs in a stepwise fashion; first, the acyclic dimer is formed, which is subsequently converted to the cyclic dimer.[21] The barrier for interconversion from the acyclic to cyclic structure was previously estimated with the B3LYP/TZ2P(f,d)+diff method to be 11.7 kJ mol^{-1}.[36]

I observed both cyclic and acyclic dimers of the formic acid dimer in helium nanodroplets at 0.38 K, in contrast to a previous study, where only the acyclic form was

observed.[27] Structures of clusters formed in helium nanodroplets often differ from those found in the gas phase, due to the unique growth conditions in liquid helium. In free-jet expansions, clusters are formed by three-body collisions, which provide the necessary conservation of momentum and energy. These clusters are formed by collisions between relatively warm molecules which subsequently cool down to tens of kelvin in the expansion. In contrast, in superfluid helium the growth occurs by subsequent pickup of monomers, which are cooled by the helium prior to aggregation.[49] At long range, both molecular dipoles will be oriented in a head-tail configuration because of the relatively strong dipole-dipole interactions. This is in agreement with the previous observation of the acyclic structure of the formic acid dimer in helium droplets.[27] There is a barrier of ~12 kJ mol^{-1} between the approach geometry and the global minimum, *cyc*-$(HCOOH)_2$, which exceeds the small internal energy present at 0.38 K. Reorientation to the global minimum on the potential energy surface and formation of cyclic structure through stepwise mechanism is therefore not possible in helium nanodroplets. However, at closer distances there are, besides the dipole-dipole electrostatic interaction, other interactions, including dispersion interactions, which may become important and might play a crucial role in formation of the cyclic structure of the formic acid dimer in droplets through a barrierless channel.

7.4 Conclusions

This Chapter details the studies done on the *cyc*-$(HCOOH)_2$ dimer in helium nanodroplets. Characteristic lines were observed at 3082.30 cm^{-1} for the O–H stretching (ν_{17}) and at 2940.56(R), 2940.43(Q), and 2940.31(P) cm^{-1} for C–H stretching (ν_{18}) vibrations of *cyc*-

$(HCOOH)_2$. The assignments are in excellent agreement with the lines observed in jet-cooled CRD experiments and consistent with ab initio predicted vibrational spectral shifts. The assignments are also in good agreement with the expected deuterium isotopic shifts. The assignment to the cyclic dimer is further supported by a rotational contour analysis of the C–H stretch vibrational band structure of *cyc*-$(HCOOH)_2$. The rotational A', B', and C' constants for the cyclic dimer in superfluid helium are found to be reduced by 63%, 67%, and 74%, respectively, with respect to the gas phase, which indicates dragging of helium density by the dimer in the helium environment. I observed both local, *acy*-$(HCOOH)_2$, and global minimum energy structures, *cyc*-$(HCOOH)_2$, in helium nanodroplets and conclude that formation of cyclic structure occurs through a barrier less channel and is stabilized by short-range interactions. A comparison of experimental and simulated infrared spectra of *cyc*-$(HCOOH)_2$ indicates that the B3PW91(DFT) method is superior to the MP2 method for frequency calculations.

References

[1] D. B. Millet, M. Baasandorj, D. K. Farmer, J. A. Thornton, K. Baumann, P. Brophy, S. Chaliyakunnel, J. A. de Gouw, M. Graus, L. Hu, et al., *Atmospheric Chem. Phys.* **2015**, *15*, 6283–6304.

[2] C. M. Nordstrom, A. J. McGrath, A. J. Thakkar, *Can. J. Chem.* **2010**, *88*, 736–743.

[3] A. Allouche, *J. Chem. Phys.* **2005**, *122*, 234703.

[4] M. Gadermann, D. Vollmar, R. Signorell, *Phys. Chem. Chem. Phys.* **2007**, *9*, 4535–4544.

[5] E. T. Kool, *Annu. Rev. Biophys. Biomol. Struct.* **2001**, *30*, 1–22.

[6] R. Podeszwa, K. Patkowski, K. Szalewicz, *Phys. Chem. Chem. Phys.* **2010**, *12*, 5974–5979.

[7] D. Luckhaus, *Phys. Chem. Chem. Phys.* **2010**, *12*, 8357–8361.

[8] F. Madeja, M. Havenith, *J. Chem. Phys.* **2002**, *117*, 7162–7168.

[9] Z. Smedarchina, A. Fernández-Ramos, W. Siebrand, *J. Chem. Phys.* **2005**, *122*, 134309.

[10] A. Jain, E. L. Sibert, *J. Chem. Phys.* **2015**, *142*, 084115.

[11] Ö. Birer, M. Havenith, *Annu. Rev. Phys. Chem.* **2009**, *60*, 263–275.

[12] K. I. Lazaar, S. H. Bauer, *J. Am. Chem. Soc.* **1985**, *107*, 3769–3772.

[13] Z. Xue, M. A. Suhm, *J Chem Phys* **2009**, *131*.

[14] J. E. Bertie, K. H. Michaelian, H. H. Eysel, D. Hager, *J. Chem. Phys.* **1986**, *85*, 4779–4789.

[15] K. Mackeprang, Z.-H. Xu, Z. Maroun, M. Meuwly, H. G. Kjaergaard, *Phys. Chem. Chem. Phys.* **2016**, *18*, 24654–24662.

[16] F. Kollipost, R. W. Larsen, A. V. Domanskaya, M. Nörenberg, M. A. Suhm, *J. Chem. Phys.* **2012**, *136*, 151101.

[17] F. Ito, *Chem. Phys. Lett.* **2007**, *447*, 202–207.

[18] R. Georges, M. Freytes, D. Hurtmans, I. Kleiner, J. Vander Auwera, M. Herman, *Chem. Phys.* **2004**, *305*, 187–196.

[19] F. Ito, T. Nakanaga, *Chem. Phys.* **2002**, *277*, 163–169.

[20] F. Ito, T. Nakanaga, *Chem. Phys. Lett.* **2000**, *318*, 571–577.

[21] M. Gantenberg, M. Halupka, W. Sander, *Chem. - Eur. J.* **2000**, *6*, 1865–1869.

[22] F. Ito, *J. Chem. Phys.* **2008**, *128*, 114310.

[23] K. Marushkevich, L. Khriachtchev, J. Lundell, A. Domanskaya, M. Räsänen, *J. Phys. Chem. A* **2010**, *114*, 3495–3502.

[24] S. V. Ryazantsev, V. I. Feldman, *Phys. Chem. Chem. Phys.* **2015**, *17*, 30648–30658.

[25] M. Ortlieb, M. Havenith, *J. Phys. Chem. A* **2007**, *111*, 7355–7363.

[26] Y. Zhang, W. Li, W. Luo, Y. Zhu, C. Duan, *J. Chem. Phys.* **2017**, *146*, DOI 10.1063/1.4989863.

[27] F. Madeja, M. Havenith, K. Nauta, R. E. Miller, J. Chocholoušová, P. Hobza, *J. Chem. Phys.* **2004**, *120*, 10554–10560.

[28] J. Chocholousova, J. Vacek, P. Hobza, *Phys. Chem. Chem. Phys.* **2002**, *4*, 2119–2122.

[29] R. Kalescky, E. Kraka, D. Cremer, *Mol. Phys.* **2013**, *111*, 1497–1510.

[30] C. Qu, J. M. Bowman, *Phys. Chem. Chem. Phys.* **2016**, *18*, 24835–24840.

[31] M. Lewerenz, B. Schilling, J. P. Toennies, *Chem. Phys. Lett.* **1993**, *206*, 381–387.

[32] A. M. Morrison, T. Liang, G. E. Douberly, *Rev. Sci. Instrum.* **2013**, *84*, DOI 10.1063/1.4776179.

[33] M.J. Frisch, *Gaussian 09 Revis. E01* **2009**.

[34] A. D. Becke, *J. Chem. Phys.* **1993**, *98*, 1372–1377.

[35] T. H. Dunning, *J. Chem. Phys.* **1989**, *90*, 1007–1023.

[36] N. R. Brinkmann, G. S. Tschumper, G. Yan, H. F. Schaefer, *J. Phys. Chem. A* **2003**, *107*, 10208–10216.

[37] Y. Maréchal, *J. Chem. Phys.* **1987**, *87*, 6344–6353.

[38] T. Wachs, D. Borchardt, S. H. Bauer, *Spectrochim. Acta Part Mol. Spectrosc.* **1987**, *43*, 965–969.

[39] R. C. Millikan, K. S. Pitzer, *J. Am. Chem. Soc.* **1958**, *80*, 3515–3521.

[40] K. Marushkevich, L. Khriachtchev, M. Räsänen, M. Melavuori, J. Lundell, *J. Phys. Chem. A* **2012**, *116*, 2101–2108.

[41] Y. H. Yoon, M. L. Hause, A. S. Case, F. F. Crim, *J. Chem. Phys.* **2008**, *128*, 084305.

[42] K. Marushkevich, L. Khriachtchev, J. Lundell, A. V. Domanskaya, M. Räsänen, *J. Mol. Spectrosc.* **2010**, *259*, 105–110.

[43] C. M. Western, *J. Quant. Spectrosc. Radiat. Transf.* **2017**, *186*, 221–242.

[44] J. Lundell, M. Räsänen, Z. Latajka, *Chem. Phys.* **1994**, *189*, 245–260.

[45] M. Y. Choi, G. E. Douberly, T. M. Falconer, W. K. Lewis, C. M. Lindsay, J. M. Merritt, P. L. Stiles, R. E. Miller, *Int. Rev. Phys. Chem.* **2006**, *25*, 15–75.

[46] P. Das, C. J. Knapp, W. Jäger, *J. Mol. Spectrosc.* **2017**, *341*, 17–22.

[47] A. Almenningen, O. Bastiansen, T. Motzfeldt, *Acta. Chem. Scand.* **1969**, *65*, 2848–2864.

[48] V. V. Matylitsky, C. Riehn, M. F. Gelin, B. Brutschy, *J. Chem. Phys.* **2003**, *119*, 10553–10562.

[49] M. Lewerenz, B. Schilling, J. P. Toennies, *J. Chem. Phys.* **1995**, *102*, 8191–8207.

Chapter 8: Conclusions

This thesis constitutes the work I have completed on measuring laser infrared spectra of small molecules and molecular clusters in superfluid helium nanodroplets. With the use of high-resolution infrared spectroscopy, I have examined the interplay between small molecules and the superfluid helium bath by extensive comparisons with gas phase and other matrix isolated spectra. Further, I have made use of the superfluid matrix to examine small hydrogen bonded clusters to evaluate their spectra and interpret the cluster configurations.

The hydrogen peroxide infrared spectrum in the OH stretching region is presented and the analysis described in Chapter 4. Both the asymmetric and symmetric OH stretching fundamentals were observed. Analyses of rovibrational lineshapes indicate an asymmetrical skewing of the lines, possibly due to the shedding of helium density as the rotor reaches its terminal velocity.[1] Further, the *trans*-tunneling splitting was deduced to be 7.7 cm^{-1}, a reduction of 6% relative to gas phase values, indicating that tunneling splitting is affected very little by the superfluid environment of the droplet. The rovibrational lines were too broad to resolve the

expected line splittings due to the rotational-translational coupling in hydrogen peroxide.[2] In Chapter 5, I describe measurements of the spectrum of HOOD, but again, linewidths did not permit any observation of line splittings. For HOOD, only the anymmetric stretching mode was observed, which prevented an analysis of the *trans* tunneling splitting. For the asymmetric mode, however, rotational constants are reduced by a similar amount as in H_2O_2. The $B(\approx C)$ rotational constant is reduced by ~40% in both cases, while the A constant is relatively unaffected due to the fast rotations about the *a*-axis.

In Chapter 6, I made use of a new source of hydrogen peroxide to help with the assignment of the many cluster peaks observed in the work described in Chapter 4. The solid urea-hydrogen peroxide complex provided a much cleaner source of H_2O_2,[3] resulting in considerably less water in the doped droplets. I was able to assign the free and bound OH stretching lines for the hydrogen peroxide dimer, using Poisson fits to the line signal intensity dependence on the doping pressure, as well as by intentionally co-doping with water. An optically-selected mass spectrum was recorded, and a new mass-selected spectrum was measured using a m/z = 34, which provided a much cleaner spectrum of the hydrogen peroxide dimer. An assignment of the hydrogen peroxide water cluster peaks constitutes future work. The hydrogen peroxide dimer has not been observed in the gas phase, and the reported infrared spectrum could be used to aid in the search for the hydrogen peroxide dimer in the gas phase.

Continuing with the theme of hydrogen bonded clusters in Chapter 7, I observed the spectrum of the cyclic formic acid dimer. Previously, only the acyclic dimer has been observed in helium droplets.[4] Both the OH and CH stretching fundamentals were measured, and the frequencies are in good agreement with gas phase values. The A, B, and C constants are reduced

by 63%, 67%, and 74%, respectively. The renormalization suggests that rotations about all tree axes fall within the adiabatic following regime.[5] An interesting conclusion from this chapter regards the formation mechanism of dimers in helium nanodroplets. As indicated by the presence of two different formic acid dimers in helium nanodroplets, the influence of long range attractive forces is insufficient in describing the presence of high energy dimer conformations in helium nanodroplets. My experimental work on the formic acid dimer in helium nanodroplets suggests that a more detailed exploration of dimer formation in helium nanodroplets is required.

The bulk of this thesis focused specifically on the infrared spectra of small molecules and molecular clusters. Despite a large body of research on the spectra of molecules embedded in helium nanodroplets, much remains unknown. Many questions surrounding the interaction between the helium bath and the dopant still remain, as do questions about the structure of quantum mechanical excitations within droplets, including translational modes and quantized vortices. This type of fundamental research must continue to be conducted to better inform the burgeoning area of applied nanodroplet research.

References

[1] M. N. Van Staveren, V. A. Apkarian, *J. Chem. Phys.* **2010**, *133*, DOI 10.1063/1.3469816.

[2] M. J. Quist, V. Elser, *J. Chem. Phys.* **2002**, *117*, 3878–3885.

[3] M. Pettersson, S. Tuominen, M. Räsänen, *J. Phys. Chem. A* **1997**, *101*, 1166–1171.

[4] F. Madeja, M. Havenith, K. Nauta, R. E. Miller, J. Chocholoušová, P. Hobza, *J. Chem. Phys.* **2004**, *120*, 10554–10560.

[5] M. Y. Choi, G. E. Douberly, T. M. Falconer, W. K. Lewis, C. M. Lindsay, J. M. Merritt, P. L. Stiles, R. E. Miller, *Int. Rev. Phys. Chem.* **2006**, *25*, 15–75.

Bibliography

Allouche, A. Quantum Studies of Hydrogen Bonding in Formic Acid and Water Ice Surface. *The Journal of Chemical Physics* **2005**, *122* (23), 234703.

Almenningen, A.; Bastiansen, O.; Motzfeldt, T. *Acta. Chem. Scand.* **1969**, *65*, 2848–2864.

Andronikashvili, E. L. A Direct Observation of Two Kinds of Motion in Helium II. *J. Phys. USSR* **1946**, *10*.

Antunes, F.; Brito, P. M. Quantitative Biology of Hydrogen Peroxide Signaling. *Redox Biology* **2017**, *13*, 1–7.

Babichenko, V. S.; Kagan, Y. Rotational Structure of Molecules in Quantum 4He and 3He Liquids. *Physical Review Letters* **1999**, *83* (17), 3458–3461.

Baraban, J. H.; Changala, P. B.; Stanton, J. F. The Equilibrium Structure of Hydrogen Peroxide. *Journal of Molecular Spectroscopy* **2018**, *343*, 92–95.

Barreto, P. R. P.; Vilela, A. F. A.; Lombardi, A.; Maciel, G. S.; Palazzetti, F.; Aquilanti, V. The Hydrogen Peroxide-Rare Gas Systems: Quantum Chemical Calculations and Hyperspherical Harmonic Representation of the Potential Energy Surface for Atom-Floppy Molecule Interactions. *Journal of Physical Chemistry A* **2007**, *111* (49), 12754–12762.

Becke, A. D. A New Mixing of Hartree–Fock and Local Density-functional Theories. *The Journal of Chemical Physics* **1993**, *98* (2), 1372–1377.

Becker, E. W. On the History of Cluster Beams. *Zeitschrift für Physik D Atoms, Molecules and Clusters* **1986**, *3* (2), 101–107.

Bergman, P.; Parise, B.; Liseau, R.; Larsson, B.; Olofsson, H.; Menten, K. M.; Güsten, R. Detection of Interstellar Hydrogen Peroxide. *Astronomy and Astrophysics* **2011**, *531*.

Bertie, J. E.; Michaelian, K. H.; Eysel, H. H.; Hager, D. The Raman-Active O-H and O-D Stretching Vibrations and Raman Spectra of Gaseous Formic Acid-d1 and -OD. *The Journal of Chemical Physics* **1986**, *85* (9), 4779–4789.

Bierau, F.; Kupser, P.; Meijer, G.; Von Helden, G. Catching Proteins in Liquid Helium Droplets. *Physical Review Letters* **2010**, *105* (13).

Birer, Ö.; Havenith, M. High-Resolution Infrared Spectroscopy of the Formic Acid Dimer. *Annu. Rev. Phys. Chem.* **2009**, *60* (1), 263–275.

Brink, D. M.; Stringari, S. Density of States and Evaporation Rate of Helium Clusters. *Zeitschrift für Physik D Atoms, Molecules and Clusters* **1990**, *15* (3), 257–263.

Brinkmann, N. R.; Tschumper, G. S.; Yan, G.; Schaefer, H. F. An Alternative Mechanism for the Dimerization of Formic Acid. *J. Phys. Chem. A* **2003**, *107* (47), 10208–10216.

Buchenau, H.; Knuth, E. L.; Northby, J.; Toennies, J. P.; Winkler, C. Mass Spectra and Time-of-flight Distributions of Helium Cluster Beams. *The Journal of Chemical Physics* **1990**, *92* (11), 6875–6889.

Burnham, C. J.; Xantheas, S. S.; Miller, M. A.; Applegate, B. E.; Miller, R. E. The Formation of Cyclic Water Complexes by Sequential Ring Insertion: Experiment and Theory. *Journal of Chemical Physics* **2002**, *117* (3), 1109–1122.

Cabana, A.; Savitsky, G. B.; Hornig, D. F. Vibration-Rotation Spectra of CH_4 and CD_4 Impurities in Xenon, Krypton, and Argon Crystals. *The Journal of Chemical Physics* **1963**, *39* (11), 2942–2950.

Callegari, C.; Lehmann, K. K.; Schmied, R.; Scoles, G. Helium Nanodroplet Isolation Rovibrational Spectroscopy: Methods and Recent Results. *Journal of Chemical Physics* **2001**, *115* (22), 10090–10110.

Callicoatt, B. E.; Förde, K.; Jung, L. F.; Ruchti, T.; Janda, K. C. Fragmentation of Ionized Liquid Helium Droplets: A New Interpretation. *The Journal of Chemical Physics* **1998**, *109* (23), 10195–10200.

Chocholousova, J.; Vacek, J.; Hobza, P. Potential Energy and Free Energy Surfaces of the Formic Acid Dimer: Correlated Ab Initio Calculations and Molecular Dynamics Simulations. *Phys. Chem. Chem. Phys.* **2002**, *4* (11), 2119–2122.

Choi, M. Y.; Douberly, G. E.; Falconer, T. M.; Lewis, W. K.; Lindsay, C. M.; Merritt, J. M.; Stiles, P. L.; Miller, R. E. Infrared Spectroscopy of Helium Nanodroplets: Novel Methods for Physics and Chemistry. *International Reviews in Physical Chemistry* **2006**, *25* (1–2), 15–75.

Clancy, R. T.; Sandor, B. J.; Moriarty-Schieven, G. H. A Measurement of the 362 GHz Absorption Line of Mars Atmospheric H2O2. *Icarus* **2004**, *168* (1), 116–121.

Conjusteau, A.; Callegari, C.; Reinhard, I.; Lehmann, K. K.; Scoles, G. Microwave Spectra of HCN and DCN in 4He Nanodroplets: A Test of Adiabatic Following. *The Journal of Chemical Physics* **2000**, *113* (12), 4840–4843.

Cook, W. B.; Hunt, R. H.; Shelton, W. N.; Flaherty, F. A. Torsion-Rotation Energy Levels, Hindering Potential, and Inertial Parameters of the First Excited Vibrational State of the Antisymmetric O-H Stretch in Hydrogen Peroxide. *Journal of Molecular Spectroscopy* **1995**, *171* (1), 91–112.

Cowley, R. A.; Woods, A. D. B. *Can. J. Phys.* **1971**, *49*.

Das, P.; Knapp, C. J.; Jäger, W. Ro-Vibrational Spectroscopy of the Formic Acid-d1 Monomer Embedded in Helium Nanodroplets. *Journal of Molecular Spectroscopy* **2017**, *341*, 17–22.

Denis, P. A.; Ornellas, F. R. Theoretical Characterization of Hydrogen Polyoxides: HOOH, HOOOH, HOOOOH, and HOOO. *Journal of Physical Chemistry A* **2009**, *113* (2), 499–506.

Dunning, T. H. Gaussian Basis Sets for Use in Correlated Molecular Calculations. I. The Atoms Boron through Neon and Hydrogen. *The Journal of Chemical Physics* **1989**, *90* (2), 1007–1023.

Elango, M.; Parthasarathi, R.; Subramanian, V.; Ramachandran, C. N.; Sathyamurthy, N. Hydrogen Peroxide Clusters: The Role of Open Book Motif in Cage and Helical Structures. *Journal of Physical Chemistry A* **2006**, *110* (19), 6294–6300.

Encrenaz, T.; Bézard, B.; Greathouse, T. K.; Richter, M. J.; Lacy, J. H.; Atreya, S. K.; Wong, A. S.; Lebonnois, S.; Lefèvre, F.; Forget, F. Hydrogen Peroxide on Mars: Evidence for Spatial and Seasonal Variations. *Icarus* **2004**, *170* (2), 424–429.

Engdahl, A.; Nelander, B.; Karlström, G. A Matrix Isolation and Ab Initio Study of the Hydrogen Peroxide Dimer. *Journal of Physical Chemistry A* **2001**, *105* (37), 8393–8398.

Engdahl, A.; Nelander, B. The Structure of the Water-Hydrogen Peroxide Complex. A Matrix Isolation Study. *Physical Chemistry Chemical Physics* **2000**, *2* (18), 3967–3970.

Engdahl, A.; Nelander, B. The Vibrational Spectrum of H_2O_3. *Science* **2002**, *295* (5554), 482–483.

Engdahl, A.; Nelander, B. The HOOH-HOO Complex. A Matrix Isolation Study. *Physical Chemistry Chemical Physics* **2004**, *6* (4), 730–734.

Flaud, J.-M.; Camy-Peyret, C.; Johns, J. W. C.; Carli, B. The Far Infrared Spectrum of H2O2. First Observation of the Staggering of the Levels and Determination of the Cis Barrier. *The Journal of Chemical Physics* **1989**, *91* (3), 1504–1510.

Flaud, J.-M.; Johns, J. W. C.; Lu, Z.; Winnewisser, G.; Klein, H. The Torsion-Rotation Spectrum of D2O2. *Canadian Journal of Physics* **2001**, *79* (2–3), 367–374.

Flaud, J.-M.; Perrin, A. High-Resolution Infrared Spectroscopy and One-Dimensional Large Amplitude Motion in Asymmetric Tops: HNO3 and H2O2. In *Vibration-Rotational*

Spectroscopy and Molecular Dynamics; Advanced Series in Physical Chemistry; World Scientific: Singapore, 1997; Vol. 9, pp 396–460.

Fraley, P. E.; Narahari Rao, K. High Resolution Infrared Spectra of Water Vapor. ν1 and ν3 Band of H2 16O. *Journal of Molecular Spectroscopy* **1969**, *29* (1–3), 348–364.

Friedmann, H.; Kimel, S. Theory of Shifts of Vibration-Rotation Lines of Diatomic Molecules in Noble-Gas Matrices. Intermolecular Forces in Crystals. *The Journal of Chemical Physics* **1965**, *43* (11), 3925–3939.

Frisch, M. J. *Gaussian 03, Revision E.01* **2004**.

Fröchtenicht, R.; Toennies, J. P.; Vilesov, A. High-Resolution Infrared Spectroscopy of SF6 Embedded in He Clusters. *Chemical Physics Letters* **1994**, *229* (1), 1–7.

Gadermann, M.; Vollmar, D.; Signorell, R. Infrared Spectroscopy of Acetic Acid and Formic Acid Aerosols: Pure and Compound Acid/Ice Particles. *Physical Chemistry Chemical Physics* **2007**, *9* (32), 4535–4544.

Gantenberg, M.; Halupka, M.; Sander, W. Dimerization of Formic Acid - An Example of A "noncovalent" reaction Mechanism. *Chemistry - A European Journal* **2000**, *6* (10), 1865–1869.

Georges, R.; Freytes, M.; Hurtmans, D.; Kleiner, I.; Vander Auwera, J.; Herman, M. Jet-Cooled and Room Temperature FTIR Spectra of the Dimer of Formic Acid in the Gas Phase. *Chemical Physics* **2004**, *305* (1), 187–196.

Gomez, L. F.; Ferguson, K. R.; Cryan, J. P.; Bacellar, C.; Tanyag, R. M. P.; Jones, C.; Schorb, S.; Anielski, D.; Belkacem, A.; Bernando, C.; et al. Shapes and Vorticities of Superfluid Helium Nanodroplets. *Science* **2014**, *345* (6199), 906.

Gomez, L. F.; Loginov, E.; Sliter, R.; Vilesov, A. F. Sizes of Large He Droplets. *The Journal of Chemical Physics* **2011**, *135* (15), 154201.

Goyal, S.; Schutt, D. L.; Scoles, G. Vibrational Spectroscopy of Sulfur Hexafluoride Attached to Helium Clusters. *Physical Review Letters* **1992**, *69* (6), 933–936.

Grebenev, S.; Hartmann, M.; Havenith, M.; Sartakov, B.; Toennies, J. P.; Vilesov, A. F. The Rotational Spectrum of Single OCS Molecules in Liquid 4He Droplets. *Journal of Chemical Physics* **2000**, *112* (10), 4485–4495.

Grebenev, S.; Toennies, J. P.; Vilesov, A. F. Superfluidity within a Small Helium-4 Cluster: The Microscopic Andronikashvili Experiment. *Science* **1998**, *279* (5359), 2083–2086.

Grisenti, R. E.; Toennies, J. P. Cryogenic Microjet Source for Orthotropic Beams of Ultralarge Superfluid Helium Droplets. *Phys. Rev. Lett.* **2003**, *90* (23), 234501.

Grzechnik, K.; Mierzwicki, K.; Mielke, Z. Matrix-Isolated Hydrogen-Bonded and Van Der Waals Complexes of Hydrogen Peroxide with OCS and CS2. *ChemPhysChem* **2013**, *14* (4), 777–787.

Gutberlet, A.; Schwaab, G.; Birer, Ö.; Masia, M.; Kaczmarek, A.; Forbert, H.; Havenith, M.; Marx, D. Aggregation-Induced Dissociation of HCl(H 2O) 4 below 1 K: The Smallest Droplet of Acid. *Science* **2009**, *324* (5934), 1545–1548.

Harms, J.; Hartmann, M.; Toennies, J. P.; Vilesov, A. F.; Sartakov, B. Rotational Structure of the IR Spectra of Single SF6 Molecules in Liquid 4He and 3He Droplets. *Journal of Molecular Spectroscopy* **1997**, *185* (1), 204–206.

Harms, J.; Toennies, J. P.; Knuth, E. L. Droplets Formed in Helium Free-Jet Expansions from

States near the Critical Point. *The Journal of Chemical Physics* **1997**, *106* (8), 3348–3357.

Harms, J.; Toennies, J. P.; Dalfovo, F. Density of Superfluid Helium Droplets. *Phys. Rev. B* **1998**, *58* (6), 3341–3350.

Hartmann, M.; Mielke, F.; Toennies, J. P.; Vilesov, A. F.; Benedek, G. Direct Spectroscopic Observation of Elementary Excitations in Superfluid He Droplets. *Physical Review Letters* **1996**, *76* (24), 4560–4563.

Hartmann, M.; Miller, R. E.; Toennies, J. P.; Vilesov, A. Rotationally Resolved Spectroscopy of SF6 in Liquid Helium Clusters: A Molecular Probe of Cluster Temperature. *Physical Review Letters* **1995**, *75* (8), 1566–1569.

Helminger, P.; Bowman, W. C.; De Lucia, F. C. A Study of the Rotational-Torsional Spectrum of Hydrogen Peroxide between 80 and 700 GHz. *Journal of Molecular Spectroscopy* **1981**, *85* (1), 120–130.

Henderson, A.; Stafford, R.; Miller, J. H. Continuous Wave Optical Parametric Oscillators Break New Spectral Ground. *Spectroscopy (Santa Monica)* **2005**, *20* (11), 12–18.

Henderson, A.; Stafford, R. Intra-Cavity Power Effects in Singly Resonant Cw OPOs. *Applied Physics B: Lasers and Optics* **2006**, *85* (2–3), 181–184.

Henderson, A.; Stafford, R. Low Threshold, Singly-Resonant CW OPO Pumped by an All-Fiber Pump Source. *Optics Express* **2006**, *14* (2), 767–772.

Henderson, A. Mid-IR Tunable Lasers Probe Hydrocarbon Molecules. *Photonics Spectra* **2009**, *43* (9).

Herberth, D.; Baum, O.; Pirali, O.; Roy, P.; Thorwirth, S.; Yamada, K. M. T.; Schlemmer, S.; Giesen, T. F. Far Infrared Fourier-Transform Spectroscopy of Mono-Deuterated Hydrogen Peroxide HOOD. *Journal of Quantitative Spectroscopy and Radiative Transfer* **2012**, *113* (11), 1127–1133.

Hooker, S.; Webb, C. *Laser Physics*, 1st ed.; Oxford Master Series in Atomic, Optical, and Laser Physics; Oxford University Press: New York, USA, 2010.

Hougen, J. T. Summary Of Group Theoretical Results For Microwave And Infrared Studies Of H//2o//2. *Canadian journal of physics* **1984**, *62* (12), 1392–1402.

Huisken, F.; Kaloudis, M.; Vigasin, A. A. Vibrational Frequency Shifts Caused by Weak Intermolecular Interactions. *Chemical Physics Letters* **1997**, *269* (3–4), 235–243.

Hunt, R. H.; Leacock, R. A.; Wilbur Peters, C.; Hecht, K. T. Internal-Rotation in Hydrogen Peroxide: The Far-Infrared Spectrum and the Determination of the Hindering Potential. *The Journal of Chemical Physics* **1965**, *42* (6), 1931–1946.

Ito, F. Jet-Cooled Infrared Spectra of the Formic Acid Dimer by Cavity Ring-down Spectroscopy: Observation of the C-O Stretching Region and Vibrational Analysis of the Fermi-Triad System. *Chemical Physics Letters* **2007**, *447* (4–6), 202–207.

Ito, F.; Nakanaga, T. A Jet-Cooled Infrared Spectrum of the Formic Acid Dimer by Cavity Ring-down Spectroscopy. *Chemical Physics Letters* **2000**, *318* (6), 571–577.

Ito, F.; Nakanaga, T. Jet-Cooled Infrared Spectra of the Formic Acid Dimer by Cavity Ring-down Spectroscopy: Observation of the O H Stretching Region. *Chemical Physics* **2002**, *277* (2), 163–169.

Ito, F. Infrared Spectra of $(HCOOH)_2$ and $(DCOOH)_2$ in Rare Gas Matrices: A Comparative Study with Gas Phase Spectra. *The Journal of Chemical Physics* **2008**, *128* (11), 114310.

Jain, A.; Sibert, E. L. Tunneling Splittings in Formic Acid Dimer: An Adiabatic Approximation to the Herring Formula. *The Journal of Chemical Physics* **2015**, *142* (8), 084115.

Kalescky, R.; Kraka, E.; Cremer, D. Local Vibrational Modes of the Formic Acid Dimer – the Strength of the Double Hydrogen Bond. *Molecular Physics* **2013**, *111* (9–11), 1497–1510.

Kamerlingh, O. H. *Commun. Phys. Lab. Univ. Leiden* **1908**, *105*, 3.

Kapitza, P. Viscosity of Liquid Helium below the λ-Point [1]. *Nature* **1938**, *141* (3558), 74.

Khriachtchev, L.; Pettersson, M.; Tuominen, S.; Räsänen, M. Photochemistry of Hydrogen Peroxide in Solid Argon. *The Journal of Chemical Physics* **1997**, *107* (18), 7252–7259.

Knuth, E. L.; Henne, U. Average Size and Size Distribution of Large Droplets Produced in a Free-Jet Expansion of a Liquid. *The Journal of Chemical Physics* **1999**, *110* (5), 2664–2668.

Knuth, E. L.; Schilling, B.; Toennies, J. P. *Proceedings of the 19th International Symposium on Rarefied Gas Dynamics, University of Oxford, 1994* **1995**.

Kollipost, F.; Larsen, R. W.; Domanskaya, A. V.; Nörenberg, M.; Suhm, M. A. Communication: The Highest Frequency Hydrogen Bond Vibration and an Experimental Value for the Dissociation Energy of Formic Acid Dimer. *The Journal of Chemical Physics* **2012**, *136* (15), 151101.

Kool, E. T. Hydrogen Bonding, Base Stacking, and Steric Effects in DNA Replication. *Annu. Rev. Biophys. Biomol. Struct.* **2001**, *30* (1), 1–22.

Koput, J.; Carter, S.; Handy, N. C. Ab Initio Prediction of the Vibrational-Rotational Energy Levels of Hydrogen Peroxide and Its Isotopomers. *Journal of Chemical Physics* **2001**, *115* (18), 8345–8350.

Krasnokutski, S. A.; Kuhn, M.; Renzler, M.; Jäger, C.; Henning, T.; Scheier, P. Ultra-Low-Temperature Reactions Of Carbon Atoms With Hydrogen Molecules. *Astrophysical Journal Letters* **2016**, *818* (2).

Kulkarni, A. D.; Rai, D.; Bartolotti, L. J.; Pathak, R. K. Methyl Hydrogen Peroxide Dimer: A Structural Study. *Journal of Molecular Structure: THEOCHEM* **2007**, *824* (1–3), 32–38.

Kuma, S.; Slipchenko, M. N.; Momose, T.; Vilesov, A. F. Infrared Spectra and Intensities of ArH2O and O 2H2O Complexes in the Range of the ν3 Band of H2O. *Journal of Physical Chemistry A* **2010**, *114* (34), 9022–9027.

Kuyanov, K. E.; Slipchenko, M. N.; Vilesov, A. F. Spectra of the ν1 and ν3 Bands of Water Molecules in Helium Droplets. *Chemical Physics Letters* **2006**, *427* (1–3), 5–9.

Kuyanov-Prozument, K.; Choi, M. Y.; Vilesov, A. F. Spectrum and Infrared Intensities of OH-Stretching Bands of Water Dimers. *Journal of Chemical Physics* **2010**, *132* (1).

Landau, L. Theory of the Superfluidity of Helium II. *Phys. Rev.* **1941**, *60* (4), 356–358.

Lannon, J. A.; Verderame, F. D.; Anderson Jr., R. W. Infrared Spectrum of Solid and Matrix-Isolated H2O2 and D2O2. *The Journal of Chemical Physics* **1971**, *54* (5), 2212–2223.

Lasne, J.; Noblet, A.; Szopa, C.; Navarro-González, R.; Cabane, M.; Poch, O.; Stalport, F.; François, P.; Atreya, S. K.; Coll, P. Oxidants at the Surface of Mars: A Review in Light of Recent Exploration Results. *Astrobiology* **2016**, *16* (12), 977–996.

Lazaar, K. I.; Bauer, S. H. Conversions over Low Barriers. 4. Dimer/Monomer Dissociation in Formic Acid. *J. Am. Chem. Soc.* **1985**, *107* (13), 3769–3772.

Lee, E.; Farrelly, D.; Whaley, K. B. Rotational Level Structure of SF6-Doped 4 HeN Clusters. *Physical Review Letters* **1999**, *83* (19), 3812–3815.

Lehmann, K. K. Potential of a Neutral Impurity in a Large 4He Cluster. *Molecular Physics* **1999**, *97* (5), 645–666.

Lehmann, K. K. Rotation in Liquid 4HE: Lessons from a Highly Simplified Model. *Journal of Chemical Physics* **2001**, *114* (10), 4643–4648.

Lehmann, K. K. Lorentzian Line Shape due to an Inhomogeneous Size Distribution without Relaxation. *Journal of Chemical Physics* **2007**, *126* (2).

Lehnig, R.; Blinov, N. V.; Jäger, W. Evidence for an Energy Level Substructure of Molecular States in Helium Droplets. *Journal of Chemical Physics* **2007**, *127* (24).

Lehnig, R.; Jäger, W. Infrared Spectroscopy of the Antisymmetric Stretching Mode of 16OC18O in Helium Nanodroplets. *Chemical Physics Letters* **2006**, *424* (1–3), 146–150.

Lehnig, R.; Raston, P. L.; Jäger, W. Rotational Spectroscopy of Single Carbonyl Sulfide Molecules Embedded in Superfluid Helium Nanodroplets. *Faraday Discussions* **2009**, *142*, 297–309.

Lewerenz, M.; Schilling, B.; Toennies, J. P. A New Scattering Deflection Method for Determining and Selecting the Sizes of Large Liquid Clusters of 4He. *Chemical Physics Letters* **1993**, *206* (1–4), 381–387.

Lewerenz, M.; Schilling, B.; Toennies, J. P. Successive Capture and Coagulation of Atoms and Molecules to Small Clusters in Large Liquid Helium Clusters. *The Journal of Chemical Physics* **1995**, *102* (20), 8191–8207.

Lewis, W. K.; Lindsay, C. M.; Bemish, R. J.; Miller, R. E. Probing Charge-Transfer Processes in Helium Nanodroplets by Optically Selected Mass Spectrometry (OSMS): Charge Steering by Long-Range Interactions. *Journal of the American Chemical Society* **2005**, *127* (19), 7235–7242.

Lindsay, C. M.; Douberly, G. E.; Miller, R. E. Rotational and Vibrational Dynamics of H2O and HDO in Helium Nanodroplets. *Journal of Molecular Structure* **2006**, *786* (2–3 SPEC. ISS.), 96–104.

Lovejoy, C. M.; Nelson Jr., D. D.; Nesbitt, D. J. Hindered Internal Rotation in Jet Cooled H2HF Complexes. *The Journal of Chemical Physics* **1987**, *87* (10), 5621–5628.

Luckhaus, D. Hydrogen Exchange in Formic Acid Dimer: Tunnelling above the Barrier. *Phys. Chem. Chem. Phys.* **2010**, *12* (29), 8357–8361.

Lundell, J.; Jolkkonen, S.; Khriachtchev, L.; Pettersson, M.; Räsänen, M. Matrix Isolation and Ab Initio Study of the Hydrogen-Bonded H2O2-CO Complex. *Chemistry - A European Journal* **2001**, *7* (8), 1670–1678.

Lundell, J.; Pehkonen, S.; Pettersson, M.; Räsänen, M. Interaction between Hydrogen Peroxide and Molecular Nitrogen. *Chemical Physics Letters* **1998**, *286* (5–6), 382–388.

Lundell, J.; Räsänen, M.; Latajka, Z. Matrix Isolation FTIR and Ab Initio Study of Complexes between Formic Acid and Nitrogen. *Chemical Physics* **1994**, *189* (2), 245–260.

Maciel, G. S.; Bitencourt, A. C. P.; Ragni, M.; Aquilanti, V. Studies of the Dynamics around the O-O Bond: Orthogonal Local Modes of Hydrogen Peroxide. *Chemical Physics Letters* **2006**, *432* (4–6), 383–390.

Mackeprang, K.; Xu, Z.-H.; Maroun, Z.; Meuwly, M.; Kjaergaard, H. G. Spectroscopy and Dynamics of Double Proton Transfer in Formic Acid Dimer. *Phys. Chem. Chem. Phys.* **2016**, *18* (35), 24654–24662.

Madeja, F.; Havenith, M.; Nauta, K.; Miller, R. E.; Chocholoušová, J.; Hobza, P. Polar Isomer of Formic Acid Dimers Formed in Helium Nanodroplets. *Journal of Chemical Physics* **2004**, *120* (22), 10554–10560.

Madeja, F.; Havenith, M. High Resolution Spectroscopy of Carboxylic Acid in the Gas Phase: Observation of Proton Transfer in (DCOOH)2. *Journal of Chemical Physics* **2002**, *117* (15), 7162–7168.

Madeja, F.; Markwick, P.; Havenith, M.; Nauta, K.; Miller, R. E. Rotationally Resolved Infrared Spectroscopy of h2- and d1-Formic Acid Monomer in Liquid He Droplets. *Journal of Chemical Physics* **2002**, *116* (7), 2870–2878.

Małyszek, P.; Koput, J. Accurate Ab Initio Potential Energy Surface and Vibration-Rotation Energy Levels of Hydrogen Peroxide. *Journal of Computational Chemistry* **2013**, *34* (5), 337–345.

Manatt, S. L.; Manatt, M. R. R. On the Analyses of Mixture Vapor Pressure Data: The Hydrogen Peroxide/Water System and Its Excess Thermodynamic Functions. *Chemistry - A European Journal* **2004**, *10* (24), 6540–6557.

Manatt, S. L.; Manatt, M. R. R. *Chem.-Eur. J.* **2006**, *12*, 3695.

Maréchal, Y. IR Spectra of Carboxylic Acids in the Gas Phase: A Quantitative Reinvestigation. *The Journal of Chemical Physics* **1987**, *87* (11), 6344–6353.

Marinetti, F.; Bodo, E.; Gianturco, F. A. Microsolvation of an Ionic Dopant in Small 4He Clusters: OH +(3Σ)(4He)N via Genetic Algorithm Optimizations. *ChemPhysChem* **2007**, *8* (1), 93–100.

Marushkevich, K.; Khriachtchev, L.; Lundell, J.; Domanskaya, A. V.; Räsänen, M. Vibrational Spectroscopy of Trans and Cis Deuterated Formic Acid (HCOOD): Anharmonic Calculations and Experiments in Argon and Neon Matrices. *Journal of Molecular Spectroscopy* **2010**, *259* (2), 105–110.

Marushkevich, K.; Khriachtchev, L.; Lundell, J.; Domanskaya, A.; Räsänen, M. Matrix Isolation and Ab Initio Study of Trans−Trans and Trans−Cis Dimers of Formic Acid. *J. Phys. Chem. A* **2010**, *114* (10), 3495–3502.

Marushkevich, K.; Khriachtchev, L.; Räsänen, M.; Melavuori, M.; Lundell, J. Dimers of the Higher-Energy Conformer of Formic Acid: Experimental Observation. *J. Phys. Chem. A* **2012**, *116* (9), 2101–2108.

Massey, J. T.; Bianco, D. R. The Microwave Spectrum of Hydrogen Peroxide. *The Journal of Chemical Physics* **1954**, *22* (3), 442–448.

Matylitsky, V. V.; Riehn, C.; Gelin, M. F.; Brutschy, B. The Formic Acid Dimer (HCOOH)2 Probed by Time-Resolved Structure Selective Spectroscopy. *The Journal of Chemical Physics* **2003**, *119* (20), 10553–10562.

McArdle, J. V.; Hoffmann, M. R. Kinetics and Mechanism of the Oxidation of Aquated Sulfur Dioxide by Hydrogen Peroxide at Low pH. *Journal of Physical Chemistry* **1983**, *87* (26), 5425–5429.

Millet, D. B.; Baasandorj, M.; Farmer, D. K.; Thornton, J. A.; Baumann, K.; Brophy, P.; Chaliyakunnel, S.; de Gouw, J. A.; Graus, M.; Hu, L.; et al. A Large and Ubiquitous Source of Atmospheric Formic Acid. *Atmospheric Chemistry & Physics* **2015**, *15* (11), 6283–6304.

Millikan, R. C.; Pitzer, K. S. The Infrared Spectra of Dimeric and Crystalline Formic Acid. *J. Am. Chem. Soc.* **1958**, *80* (14), 3515–3521.

Momose, T.; Miki, M.; Wakabayashi, T.; Shida, T.; Chan, M.-C.; Lee, S. S.; Oka, T. Infrared Spectroscopic Study of Rovibrational States of Methane Trapped in Parahydrogen Crystal. *Journal of Chemical Physics* **1997**, *107* (19), 7707–7716.

Moore, D. T.; Miller, R. E. Dynamics of Hydrogen-HF Complexes in Helium Nanodroplets. *Journal of Chemical Physics* **2003**, *118* (21), 9629–9636.

Morrison, A. M.; Liang, T.; Douberly, G. E. Automation of an "Aculight" Continuous-Wave Optical Parametric Oscillator. *Review of Scientific Instruments* **2013**, *84* (1), 013102.

Morrison, A. M.; Flynn, S. D.; Liang, T.; Douberly, G. E. Infrared Spectroscopy of (HCl)m(H2O)n Clusters in Helium Nanodroplets: Definitive Assignments in the HCL Stretch Region. *Journal of Physical Chemistry A* **2010**, *114* (31), 8090–8098.

Nauta, K.; Miller, R. E. Nonequilibrium Self-Assembly of Long Chains of Polar Molecules in Superfluid Helium. *Science* **1999**, *283* (5409), 1895–1897.

Nauta, K.; Miller, R. E. Hydrogen Fluoride Dimer in Liquid Helium: A Prototype System for Studying Solvent Effects on Hydrogen Bonding. *Journal of Chemical Physics* **2000**, *113* (22), 10158–10168.

Nauta, K.; Miller, R. E. Metastable Vibrationally Excited HF (v = 1) in Helium Nanodroplets. *Journal of Chemical Physics* **2000**, *113* (21), 9466–9469.

Nauta, K.; Miller, R. E. Rotational and Vibrational Dynamics of CO_2 and N_2O in Helium Nanodroplets. *The Journal of Chemical Physics* **2001**, *115* (22), 10254–10260.

Nauta, K.; Miller, R. E. Rotational and Vibrational Dynamics of Methane in Helium Nanodroplets. *Chemical Physics Letters* **2001**, *350* (3–4), 225–232.

Nordstrom, C. M.; McGrath, A. J.; Thakkar, A. J. Microsolvation of the Formic Acid Dimer – (HCOOH)2(H2O)n Clusters with N = 1 5. *Canadian Journal of Chemistry* **2010**, *88* (8), 736–743.

Olson, W. B.; Hunt, R. H.; Young, B. W.; Maki, A. G.; Brault, J. W. Rotational Constants of the Lowest Torsional Component (0G) of the Ground State and Lowest Torsional Component (1G) of the First Excited Torsional State of Hydrogen Peroxide. *Journal of Molecular Spectroscopy* **1988**, *127* (1), 12–34.

Ortlieb, M.; Havenith, M. Proton Transfer in (HCOOH)2: An IR High-Resolution Spectroscopic Study of the Antisymmetric C-O Stretch. *Journal of Physical Chemistry A* **2007**, *111* (31), 7355–7363.

Peet, A. C.; Clary, D. C.; Hutson, J. M. A Comparison of the Vibrational Predissociation Rates in the Rare-Gas-Ethylene Clusters. *Journal of the Chemical Society, Faraday Transactions 2: Molecular and Chemical Physics* **1987**, *83* (9), 1719–1731.

Pehkonen, S.; Lundell, J.; Khriachtchev, L.; Pettersson, M.; Räsänen, M. Matrix Isolation and Quantum Chemical Studies on the H2O 2-SO2 Complex. *Physical Chemistry Chemical Physics* **2004**, *6* (19), 4607–4613.

Petkie, D. T.; Goyette, T. M.; De Lucia, F. C.; Helminger, P.; Belov, S. P.; Winnewisserr, G. Millimeter and Submillimeter-Wave Spectrum of Hydrogen Peroxide in the Ground and v3 = 1 Vibrational States. *Journal of Molecular Spectroscopy* **1998**, *192* (1), 25–31.

Petkie, D. T.; Goyette, T. M.; Holton, J. J.; Delucia, F. C.; Helminger, P. Millimeter/Submillimeter-Wave Spectrum of the First Excited Torsional State in HOOH. *Journal of Molecular Spectroscopy* **1995**, *171* (1), 145–159.

Pettersson, M.; Tuominen, S.; Räsänen, M. IR Spectroscopic Study of H_2O_2, HDO_2, and D_2O_2 Isolated in Ar, Kr, and Xe Matrices. *Journal of Physical Chemistry A* **1997**, *101* (6), 1166–1171.

Podeszwa, R.; Patkowski, K.; Szalewicz, K. Improved Interaction Energy Benchmarks for Dimers of Biological Relevance. *Phys. Chem. Chem. Phys.* **2010**, *12* (23), 5974–5979.

Qu, C.; Bowman, J. M. An Ab Initio Potential Energy Surface for the Formic Acid Dimer: Zero-Point Energy, Selected Anharmonic Fundamental Energies, and Ground-State Tunneling Splitting Calculated in Relaxed 1-4-Mode Subspaces. *Phys. Chem. Chem. Phys.* **2016**, *18* (36), 24835–24840.

Quist, M. J.; Elser, V. Dynamics of Immersed Molecules in Superfluids. *The Journal of Chemical Physics* **2002**, *117* (8), 3878–3885.

Raston, P. L.; Knapp, C. J.; Jäger, W. Rotovibrational Spectroscopy of Hydrogen Peroxide Embedded in Superfluid Helium Nanodroplets. *Physical Chemistry Chemical Physics* **2011**, *13* (42), 18789–18798.

Ryazantsev, S. V.; Feldman, V. I. Radiation-Induced Transformations of Matrix-Isolated Formic Acid: Evidence for the HCOOH [Rightward Arrow] HOCO + H Channel. *Phys. Chem. Chem. Phys.* **2015**, *17* (45), 30648–30658.

Scheidemann, A.; Toennies, J. P.; Northby, J. A. Capture of Neon Atoms by ^{4}He Clusters. *Phys. Rev. Lett.* **1990**, *64* (16), 1899–1902.

Schulz, C. P.; Claas, P.; Schumacher, D.; Stienkemeier, F. Formation and Stability of High-Spin Alkali Clusters. *Physical Review Letters* **2004**, *92* (1), 134011–134014.

Silliman, B. *Elements of Chemistry in the Order of the Lectures Given in Yale College* **1830**.

Sindzingre, P.; Klein, M. L.; Ceperley, D. M. Path-Integral Monte Carlo Study of Low-Temperature ^{4}He Clusters. *Phys. Rev. Lett.* **1989**, *63* (15), 1601–1604.

Skvortsov, D.; Sliter, R.; Choi, M. Y.; Vilesov, A. F. Interchange-Tunneling Splitting in HCl Dimer in Helium Nanodroplets. *Journal of Chemical Physics* **2008**, *128* (9).

Slipchenko, M. N.; Vilesov, A. F. Spectra of NH3 in He Droplets in the 3 Mm Range. *Chemical Physics Letters* **2005**, *412* (1–3), 176–183.

Smedarchina, Z.; Fernández-Ramos, A.; Siebrand, W. Tunneling Dynamics of Double Proton Transfer in Formic Acid and Benzoic Acid Dimers. *The Journal of Chemical Physics* **2005**, *122* (13), 134309.

Stienkemeier, F.; Bünermann, O.; Mayol, R.; Ancilotto, F.; Barranco, M.; Pi, M. Surface Location of Sodium Atoms Attached to ^{4}He Nanodroplets. *Phys. Rev. B* **2004**, *70* (21), 214509.

Stienkemeier, F.; Lehmann, K. K. Spectroscopy and Dynamics in Helium Nanodroplets. *Journal of Physics B: Atomic, Molecular and Optical Physics* **2006**, *39* (8), R127–R166.

Suárez, A. G.; Ramilowski, J. A.; Benito, R. M.; Farrelly, D. Renormalization of the Rotational Constants of an Ammonia Molecule Seeded into a 4He Droplet. *Chemical Physics Letters* **2011**, *502* (1–3), 14–22.

Szalewicz, K. Interplay between Theory and Experiment in Investigations of Molecules Embedded in Superfluid Helium Nanodroplets. *International Reviews in Physical Chemistry* **2008**, *27* (2), 273–316.

Tang, J.; Xu, J.; McKellar, A. R. W.; Jäger, W. Quantum Solvation of Carbonyl Sulfide with Helium Atoms. *Science* **2002**, *297* (5589), 2030–2033.

Tessier, A.; Forst, W. Kinetics of Hydrogen Peroxide Pyrolysis by Molecular-Beam Mass Spectrometry. *International Journal of Mass Spectrometry and Ion Physics* **1971**, *7* (4), 281–295.

Thompson, A. M. The Oxidizing Capacity of the Earth's Atmosphere: Probable Past and Future Changes. *Science* **1992**, *256* (5060), 1157.

Tiszla, L. Transport Phenomena in Helium II. *Nature* **1938**, *141*, 913.

Toennies, J. P.; Vilesov, A. F. Spectroscopy of Atoms and Molecules in Liquid Helium. *Annual Review of Physical Chemistry* **1998**, *49* (1), 1–41.

Toennies, J. P.; Vilesov, A. F. Superfluid Helium Droplets: A Uniquely Cold Nanomatrix for Molecules and Molecular Complexes. *Angewandte Chemie - International Edition* **2004**, *43* (20), 2622–2648.

Van Staveren, M. N.; Apkarian, V. A. Dynamically Skewed Lines: Rotations in Superfluid Helium. *Journal of Chemical Physics* **2010**, *133* (5).

Volk, A.; Thaler, P.; Knez, D.; Hauser, A. W.; Steurer, J.; Grogger, W.; Hofer, F.; Ernst, W. E. The Impact of Doping Rates on the Morphologies of Silver and Gold Nanowires Grown in Helium Nanodroplets. *Physical Chemistry Chemical Physics* **2016**, *18* (3), 1451–1459.

Wachs, T.; Borchardt, D.; Bauer, S. H. Resolution of Spectra of Mixtures, Applied to Gaseous Formic Acids. *Spectrochimica Acta Part A: Molecular Spectroscopy* **1987**, *43* (7), 965–969.

Western, C. M. PGOPHER: A Program for Simulating Rotational, Vibrational and Electronic Spectra. *Journal of Quantitative Spectroscopy and Radiative Transfer* **2017**, *186*, 221–242.

Xue, Z.; Suhm, M. A. *J. Chem. Phys.* **2009**, *131*.

Yoon, Y. H.; Hause, M. L.; Case, A. S.; Crim, F. F. Vibrational Action Spectroscopy of the C–H and C–D Stretches in Partially Deuterated Formic Acid Dimer. *The Journal of Chemical Physics* **2008**, *128* (8), 084305.

Zhang, Y.; Li, W.; Luo, W.; Zhu, Y.; Duan, C. High Resolution Jet-Cooled Infrared Absorption Spectra of $(HCOOH)_2$, $(HCOOD)_2$, and HCOOH-HCOOD Complexes in 7.2 μ M Region. *Journal of Chemical Physics* **2017**, *146* (24).

Zumwalt, L. R.; Giguère, P. A. The Infra-Red Bands of Hydrogen Peroxide at λ9720 and the Structure and Torsional Oscillation of Hydrogen Peroxide. *The Journal of Chemical Physics* **1941**, *9* (6), 458–462.